The Pennsylvania State University

The Graduate School

College of Engineering

DESIGN AND TESTING OF A HELICOPTER ROTOR BLADE CHORD EXTENSION SYSTEM

A Thesis in

Aerospace Engineering

by

Eric William Hayden

Submitted in Partial Fulfillment
of the Requirements
for the Degree of

Master of Science

August 2012

The thesis of Eric William Hayden was reviewed and approved* by the following:

Farhan S. Gandhi
Professor of Aerospace Engineering
Thesis Advisor

Joseph F. Horn
Associate Professor of Aerospace Engineering

George A. Lesieutre
Professor of Aerospace Engineering
Head of the Department of Aerospace Engineering

*Signatures are on file in the Graduate School

ABSTRACT

In high gross weight, high altitude, and high speed operations, the helicopter main rotor is susceptible to stall. The onset of stall both limits the envelope as well as significantly increases the power requirement. The ability to generate additional lift can reduce the power requirement and expand the envelope. One approach to generating higher lift is through chord extension morphing of sections of the main rotor blade.

This study presents a mechanism for increasing the blade chord by extending a flat plate through a slit in the trailing edge. In order to minimize the structural impact on the blade, the device was constrained to be aft of the spar. In view of the available space constraints, the mechanism consists of a single linkage which transforms spanwise actuation output into chordwise displacement. The study has considered both electromechanical and pneumatic actuation methods. As with any morphing rotor technology, the system must be able to operate within the high-g environment present in a helicopter blade. The current prototypes have been spin tested on the Pennsylvania State University's Adverse Environment Rotor Test Stand (AERTS). The test section for each prototype used a 16 in chord NACA 0015 airfoil with an 11.5 in span. The goal of the spin test was to show successful actuation of the design under the centrifugal acceleration present in a UH-60 helicopter blade at 73% rotor radius.

The electromechanically actuated extendable chord system was able to achieve 1.3 in of chordwise extension (8.13 % chord extension) at a maximum rotational speed of 385 RPM. The corresponding centrifugal acceleration of 210 g's is approximately 47% of the full-scale loading. The system was ultimately limited by the capabilities of the commercially available off-the-shelf electromechanical actuator. Under these conditions, the electromechanical motor required 40W of power.

The pneumatically actuated system was able to provide 1.9 in of chordwise extension (11.88% chord extension). With the pressure limited to 105 psi using the AERTS facility, the system was only able to operate successfully up to 315 RPM, or at 32% of full-scale centrifugal acceleration. The experimental result showed good correlation with the numerical simulation. The analysis also showed that by balancing the chordwise and spanwise forces, actuation requirements can be dramatically reduced in subsequent designs.

TABLE OF CONTENTS

LIST OF FIGURES

LIST OF TABLES

LIST OF SYMBOLS

A	Area
C_d	Drag coefficient
C_l	Lift coefficient
D	Diameter
$D_{O,CR}$	Distance from center of rotation to coordinate system origin
F	Force
F_{ACT}	Actuator force
F_{AT}	Centrifugal force on actuator components
F_{IN}	Centrifugal force on inner rail components
F_{INy}	Chordwise component of inner rail component centrifugal force
F_{LC}	Load Cell Axial Force
F_{PA}	Centrifugal force on plate assembly
F_{ROD}	Centrifugal force on linkage
FS	Factor of safety
L_{AC}	Linkage length between points A and C
L_{BC}	Linkage length between points B and C
L_{BCG}	Linkage length between point B and linkage CG
L_{CCG}	Length between point C and CG of rod end and thread adapter
L_{CE}	Length between points C and E
M_{ACT}	Actuator moment
M_{AT}	Mass of the actuator components
M_{LC}	Load Cell Moment
M_{PA}	Mass of the plate assembly
M_{ROD}	Mass of the linkage
M_S	Linear slide moment
N_S	Linear slide normal force
P	Total rotor power
P_i	Induced power
P_o	Profile power
P_p	Propulsive power
R	Blade radius
R_{AT}	Radius of actuator components
R_{Ax}	Spanwise component of the reaction force at point A
R_{Ay}	Chordwise component of the reaction force at point A
R_{Ay}	Chordwise reaction force at point A
R_{Bx}	Spanwise component of the reaction force at point B

R_{By}	Chordwise component of the reaction force at point B
R_{Cx}	Spanwise component of the reaction force at point C
Rcy	Chordwise component of the reaction force at point C
R_{PA}	Radius of plate assembly
R_{ROD}	Radius of the linkage
V	Helicopter forward air speed
V_{LC}	Load Cell Shear Force
W_i	Weight at point i
c	Blade chord
f_S	Linear slide friction force
h_{AT}	Chordwise offset of actuator component CG with repect to point A
h_B	Chordwise offset of point B with repect to point A
h_{IN}	Chordwse offset of inner rail component CG with repect to point C
h_{PA}	Chordwise offset of plate assembly CG with repect to point C
h_S	Chordwise offset of linear slide
l_1	Retracted truss length
w_{AT}	Spanwise offset of actuator component CG with repect to point A
w_B	Spanwise offset of point B with repect to point A
w_{IN}	Spanwise offset of inner rail component CG with repect to point C
w_{PA}	Spanwise offset of plate assembly CG with repect to point C
w_S	Spanwise offset of outer rail slide with repect to point C
w_{S2}	Spanwise offset of inner rail extension element with repect to point C
x_{CG}	Spanwise location of CG
x_i	Spanwise location of point i
y_{CG}	Spanwise location of CG
y_i	Chordwise location of point i
Δl	Change in truss length
Δs	Spanwise truss displacement
Ω	Rotor rotational speed
α, AOA	Angle of attack
δ_{AT}	Active tab deflection
θ_{AT}	Angle of the actuator component centrifugal force vector relative to the x-axis
θ_{IN}	Angle of the inner rail components' centrifugal force vector relative to x-axis
θ_{PA}	Angle of the plate assembly centrifugal force vector relative to the x-axis
θ_{ROD}	Angle of the linkage centrifugal force vector relative to the x-axis
$\mu_{Al,Al}$	Coefficient of friction of aluminum on aluminum
μ_S	Coefficient of friction for linear slide
σ	Stress
σ_{yield}	Yield strength
φ_{AC}	Linkage angle between points A and C

φ_{BC}	Linkage angle between points B and C
ψ	Blade azimuth

ACKNOWLEDGEMENTS

First and foremost I would like to express my deepest gratitude to my wife, Heather, and my parents, Richard and Rae Anne. My wife has demonstrated an incredible amount of patience and understanding during the late nights and weekends spent on campus. The love she has given me over the past few years has made all the hardships well worth the effort. Also, without the ideals instilled in me from a young age by my parents, I surely would not be where I am today.

I would also like to thank the many wonderful people at the Pennsylvania State University. Dr. Farhan Gandhi has given me the opportunity to pursue my academic goals and I am grateful for his guidance over the past few years. Furthermore, I would like to the staff members of the Department of Aerospace Engineering for their invaluable help. Specifically, the experiments conducted in this thesis would not have been possible without assistance from Richard Auhl and Mark Catalano. I would also like to thank the members of the Penn State AERTS team, lead by Dr. Jose Palacios, for their experience and patience during the many repeated tests on the rotor stand. I would like to acknowledge the experienced machinists at the Engineering Shop Services and the Learning Factory for helping me manufacture the prototypes.

I would also like to acknowledge the Science, Mathematics and Research for Transformation Scholarship for the financial support they provided throughout my graduate studies. Likewise, I would like to thank Mark Silva and the members of the AIR 4.3.2.1 branch at the Naval Air Warfare Center in Patuxent River, MD for allowing me to be a part of this scholarship and for their support during my internships.

Last, but not least, I would like to thank my friends who have given me so many great experiences during my time at Penn State. My friends and colleagues, Mihir Mistry and Gabriel Murray, have given me more than they will ever really know. They have really made working in the Vertical Lift Research Center of Excellence at Penn State everyday a joy and I will certainly miss them in the future. I would like to express my sincere gratitude to my friends back in Pittsburgh as well. The random trips home every few months were just what I needed to relax and reinvigorate my studies.

Chapter 1

Introduction

Although, the ideas of rotary-wing flight are first seen in Chinese “tops” around 400 BC, it is not until the early 1930s that the first controllable, human-carrying helicopters are realized. In contrast, fixed-wing aircraft quickly advanced from the initial experiments of Otto Lilienthal in 1891 to the first successful controlled flight of the Wright Flyer in 1903. This fact simultaneously demonstrates the simple concepts of rotary-wing flight as well as its complex design challenges. While other aircraft are capable of vertical landing, the helicopter is able to do so with much greater efficiency and is therefore much more practical for vertical landing and take-off. These unique features make it an essential part of modern aviation. However, this is achieved at the cost of greater power requirements in comparison to fixed-wing aircraft during forward flight. Perhaps the most unique and complex aspect of the helicopter is the main rotor. Not only is it responsible for lift, propulsion, and control, but it also is a significant contributor to the overall power consumption of the aircraft. Since the available power of the aircraft limits its performance in term of maximum gross weight, altitude, forward speed, range, and endurance, it follows that much research in the rotorcraft community revolves around main rotor power reduction.

1.1 Background and Motivation

Keeping in mind the fact that most helicopters are meant to operate in a variety of flight regimes, it is obvious that main rotor design is less of an optimum and more of a compromise. Consider the relatively simple case of hover shown in Figure 1-1; although axisymmetric, each radial location is experiencing a different incident flow velocity. The aerodynamic environment rapidly becomes more complex as the helicopter transitions to forward flight (Figure 1-2).

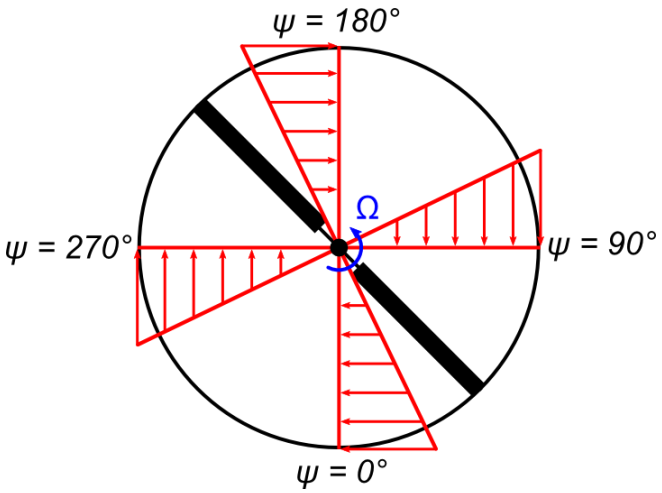

Figure 1-1: Hover tangential flow velocity field.

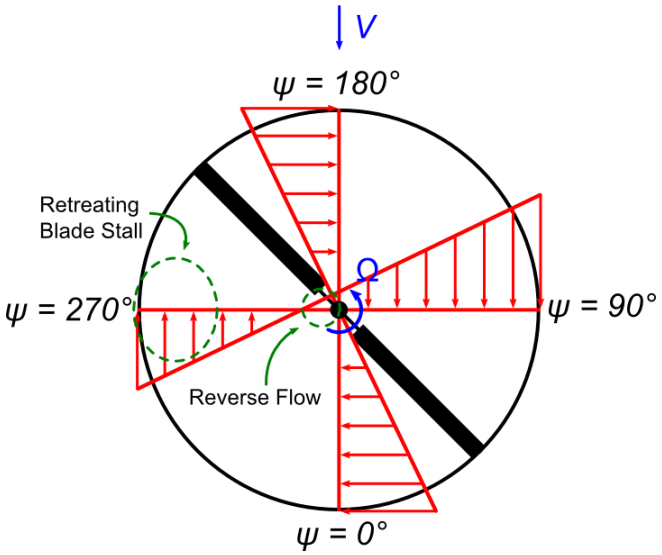

Figure 1-2: Forward flight tangential flow velocity field.

It follows then that the main source of power consumption changes as the helicopter transitions from hover into low-speed and high-speed forward flight. The total main rotor power required for steady, level flight can be divided into three components: induced power, profile power, and propulsive power (Refs. 1, 2). The induced power is a measure of the energy required to accelerate the air through the rotor disk in order to generate lift. The second contribution, profile power, is the power required to overcome the rotor blade profile drag; i.e., the forces which occur as a result of viscous losses at the blade. Finally, propulsive power is the result of parasitic airframe drag which must be overcome by a forward tilting of the rotor disk. It should be noted that induced power and propulsive power are often calculated together and separated afterwards in order to gain a better understanding of the rotor characteristics.

Estimations for main rotor power can be made using Blade Element Theory as described in Refs. 1 and 3. This method provides a simple way of demonstrating how component varies with respect forward speed for a helicopter in steady, level flight.

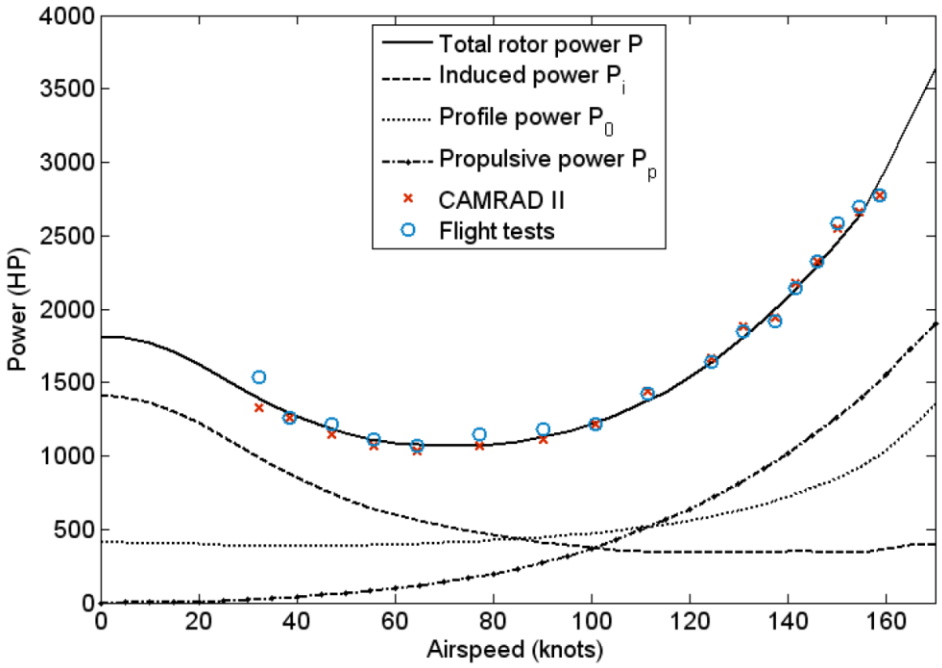

Figure 1-3: Main rotor power as a function of forward flight speed for a UH-60 type aircraft. (Ref. 2)

As shown in Figure 1-3, the induced power is high in hover and decreases with increasing forward flight speed. As parasitic airframe drag and rotor profile drag increase, the rotor disk must be progressively tilted forward which causes an increase in propulsive power at higher speeds. Moreover, the rotor profile power slowly increases for low to moderate forward speeds. However, at high velocities, compressibility effects and retreating blade stall can dramatically increase profile power. This effect will be explained further in subsequent sections.

Obviously, the total power requirements in high speed forward flight can be decreased most significantly through reductions in propulsive power and profile power. Since propulsive power is mainly a result of fuselage design, reductions can be achieved using advanced fuselage designs. However, this falls outside the scope of the current work and will therefore not be discussed further. Profile power, on the other hand, is a direct result of the main rotor blade design and has the potential to be reduced using morphing technology which can be tailored to increase performance over multiple flight regimes. There has been much research into various types of morphing technologies and their potential benefits on overall helicopter performance. However, relatively few studies have been conducted that attempt to show the feasibility of these systems at full-scale centrifugal loading. The content of this thesis presents the design of a new mechanism intended to reduce the main rotor power requirements. The operability of the device will also be shown at representative full-scale centrifugal loading. The subsequent sections of this chapter will present various morphing rotor concepts related to main rotor power reduction. Furthermore, an introductory discussion of the current morphing rotor technology will follow, as well as its advantages and disadvantages in comparison to other concepts. Finally, a progression of the work to its current state will be outlined.

1.2 Review of Related Work

1.2.1 Retreating Blade Stall

As mentioned, there have been many efforts made in designing morphing rotor technologies specifically to reduce main rotor power and potentially expand the operating envelope. As discussed in Ref. 3, the maximum speed of many current helicopters is retreating blade stall. This effect occurs as a direct result of the low tangential velocities seen by the helicopter blades at azimuth angles around 270° (Figure 1-2). Therefore, the local angle of attack needs to be sufficiently high in order to achieve the lift required to trim the rotor. During high thrust situations, such as high speed, gross weight, and altitude, the lift requirements on the retreating side become such that the blade begins to experience stall at various points along the span. This flow separation leads to high drag and a sharp decrease in lift. This is demonstrated in Figure 1-4 for the UH-60 SC1095 and SC1094 R8 airfoils (Refs. 2, 4).

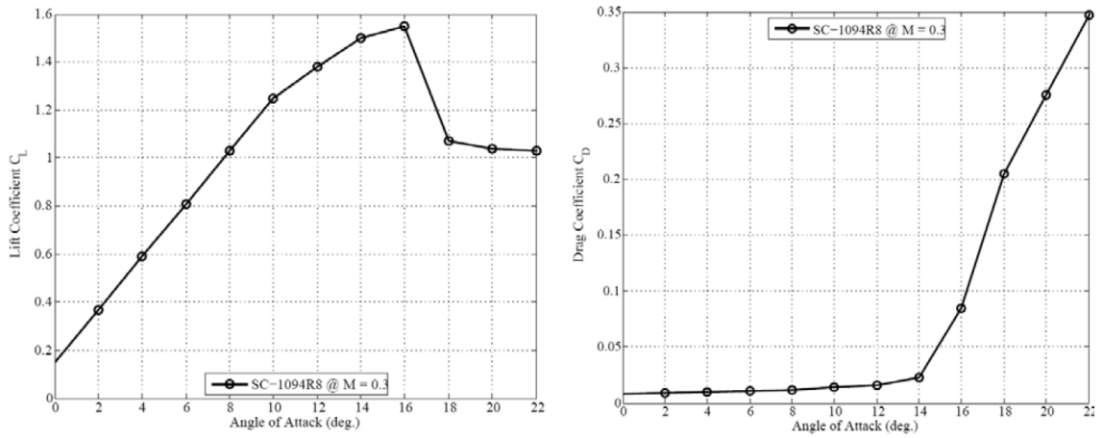

(a) (b)

Figure 1-4: (a) Lift coefficient and (b) drag coefficient as a function of the angle of attack of a SC-1094R8 airfoil at a Mach number of 0.3 (Refs. 2, 4).

Furthermore, not only does retreating blade stall lead to an increase in blade drag and rotor power, but it also produces an increase in control loads and vibrations which can be severe enough to limit forward speed as well (Ref. 3).

The feasibility of morphing rotor designs to alleviate stall and improve rotor performance has been detailed by Yeo in 2008 (Ref. 5). This study focused on active control methods such as leading edge slats, variable droop leading edges, oscillatory jets, and Gurney flaps. These devices showed no performance improvement when operated in low thrust situations; i.e. well within the operational envelope. However, as retreating blade stall becomes more important at the edges of the flight envelope, these devices showed a marked improvement. This is because each of these morphing technologies is a high lift device designed to increase maximum local lift coefficient.

1.2.2 Stall Alleviation via Extendable Chord Sections

Another approach to stall alleviation is presented by Liu et al. in Ref. 6. In this work, lift enhancement is generated by means of a thin plate extending through the trailing edge of the airfoil. The authors conducted wind tunnel experiments using several plate deployment configurations on a NACA 0012 symmetrical airfoil. The study focused on plate deployments at a zero angle relative to the trailing edge as well as various inclination angles up to 14°. The authors referred to this concept as the Static Extended Trailing Edge (SETE). The effect of the SETE on the lift and drag coefficients are shown in Figure 1-5 and Figure 1-6. Interestingly, even with a non-optimal airfoil shape, the 0° inclination showed no degradation in lift coefficient. Rather, this configuration was actually able to increase the maximum lift coefficient while having a minimal impact on drag.

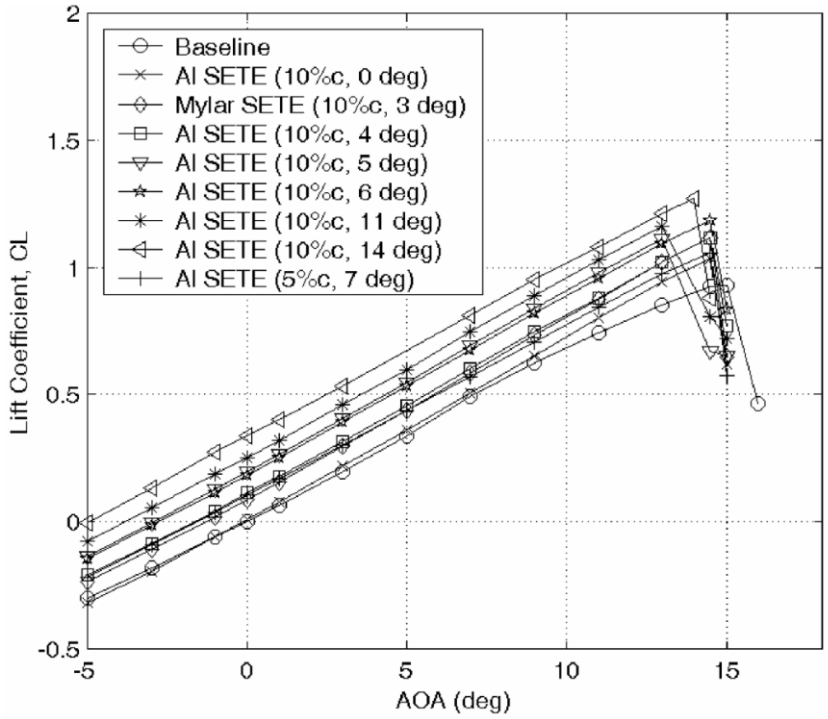

Figure 1-5: Lift coefficient as a function of angle of attack for a NACA 0012 airfoil model with the SETE (Ref. 6).

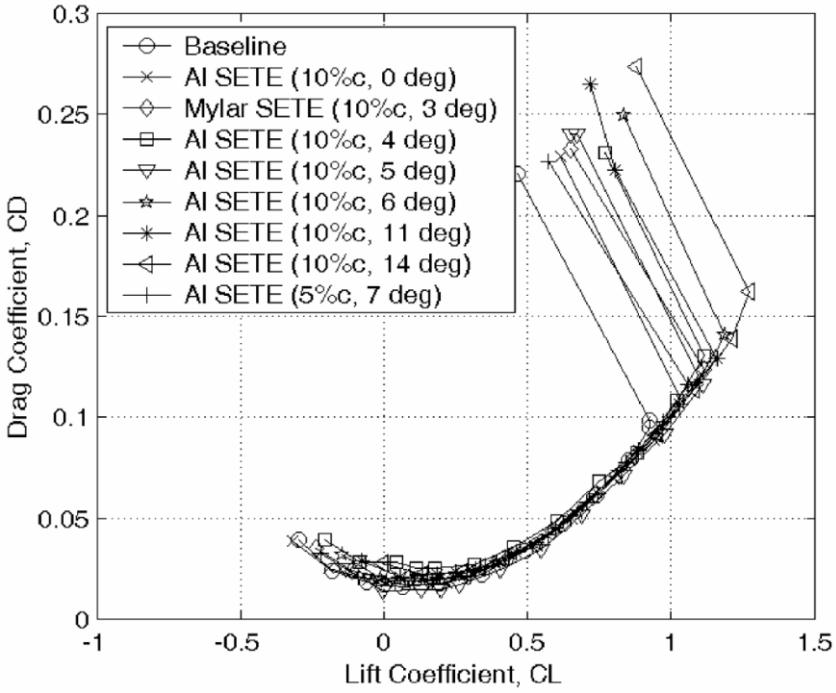

Figure 1-6: Drag polar for a NACA 0012 airfoil model with the SETE (Ref. 6).

The concept of a Static Extended Trailing Edge was then introduced as a morphing rotor blade technology by Léon et al. in 2009 (Ref. 2, 7). This work proved the viability of an extendable chord system as a means of increasing the operating envelope and reducing main rotor power (Figure 1-7).

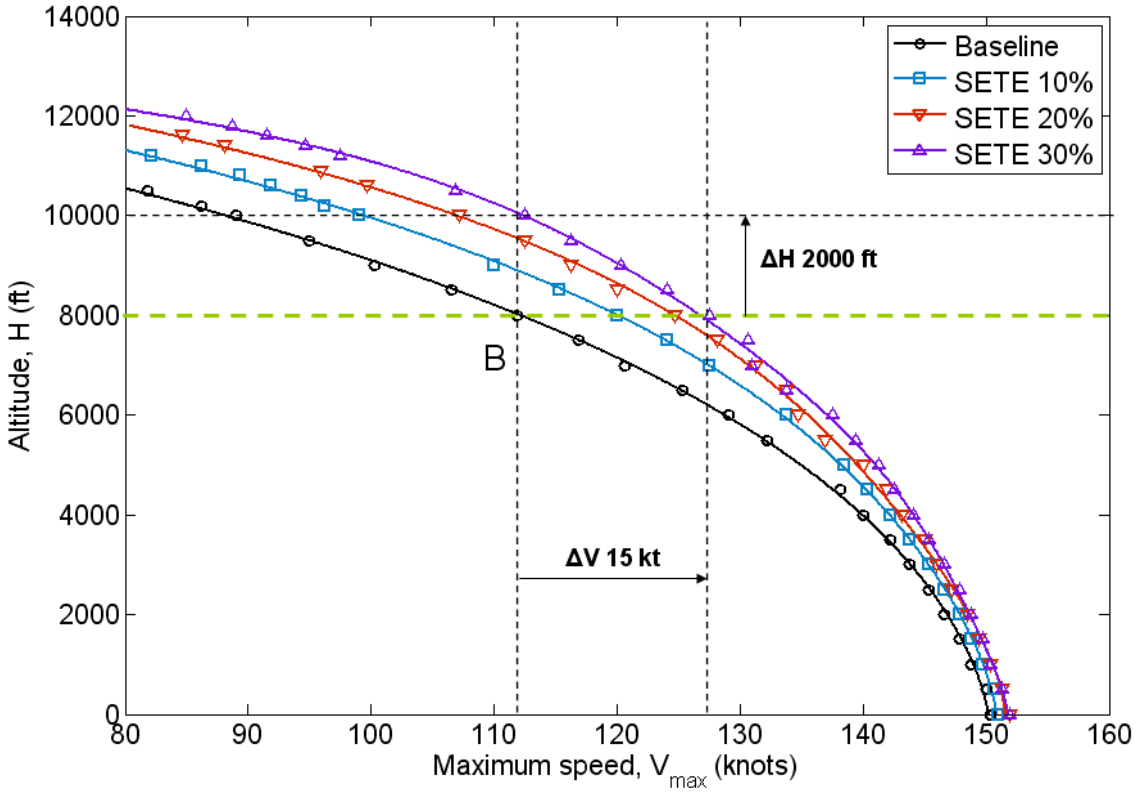

Figure 1-7: Operational envelope boundaries for UH-60 aircraft at 18,000 lbs gross weight with extendable chord sections (Ref. 7).

As shown, an extendable chord system has the potential to not only increase the maximum flight speed but also the maximum altitude for a given gross weight. The authors also recognized that without the presence of retreating blade stall, the extended chord would unnecessarily increase the profile drag of the blade. Thus, the chord needed to be extended only in high thrust situations in which stall in present. Furthermore, due to the limited profile drag

penalty as compared to other high lift devices, an extendable chord system can be actuated quasi-statically This is in contrast to other high lift devices such as Trailing Edge Flaps or Active Gurney Flaps which must be actuated at higher harmonics. The work was continued by Khoshlahjeh et al. in 2011 which included higher fidelity simulations based on a UH-60 type aircraft with a trailing edge plate extension of 20% chord from 63% - 83% radius (Ref. 8). Unlike previous work on this concept, this study implemented Navier-Stokes CFD computations to derive the 2D aerodynamic coefficients and a finite element based elastic blade model. Performance simulations were completed using the Rotorcraft Comprehensive Analysis System (RCAS).

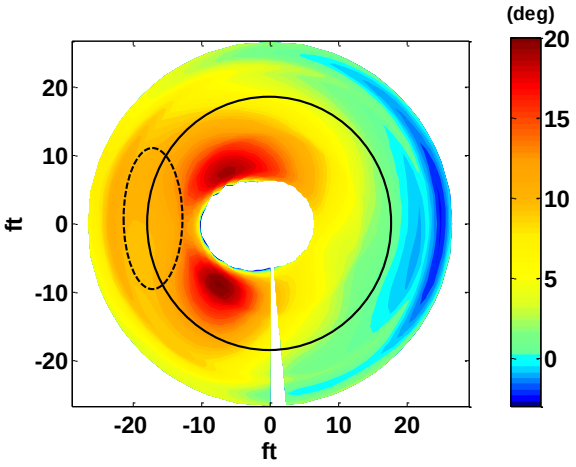

(a)

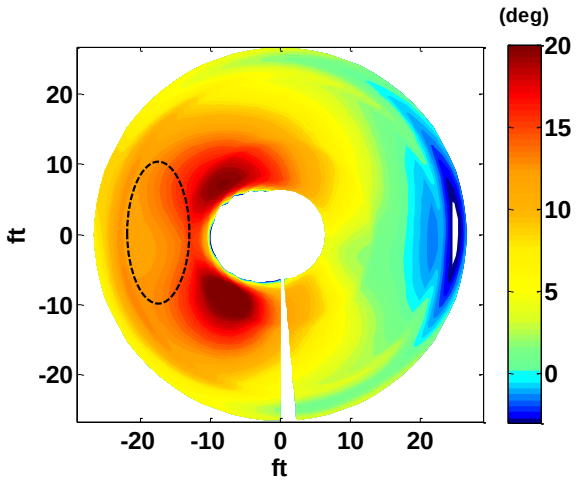

(b)

Figure 1-8: Angles of attack for a UH-60 model at 4,000 ft, 130 kts, and 24,000 lbs (a) with extended trailing edge and (b) baseline configuration (Ref. 8).

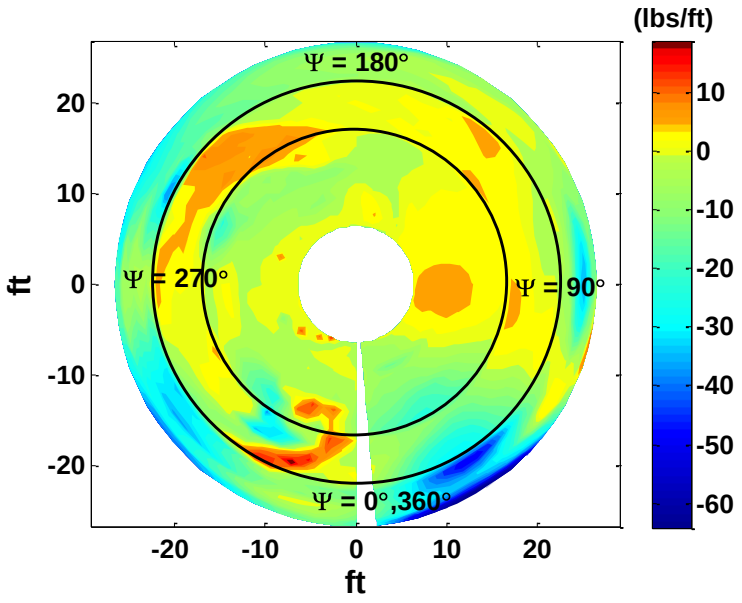

Figure 1-9: Drag difference between configuration with extended trailing edge plate and baseline UH-60 model at 4,000 ft, 130 kts, and 24,000 lbs configuration (Ref. 8).

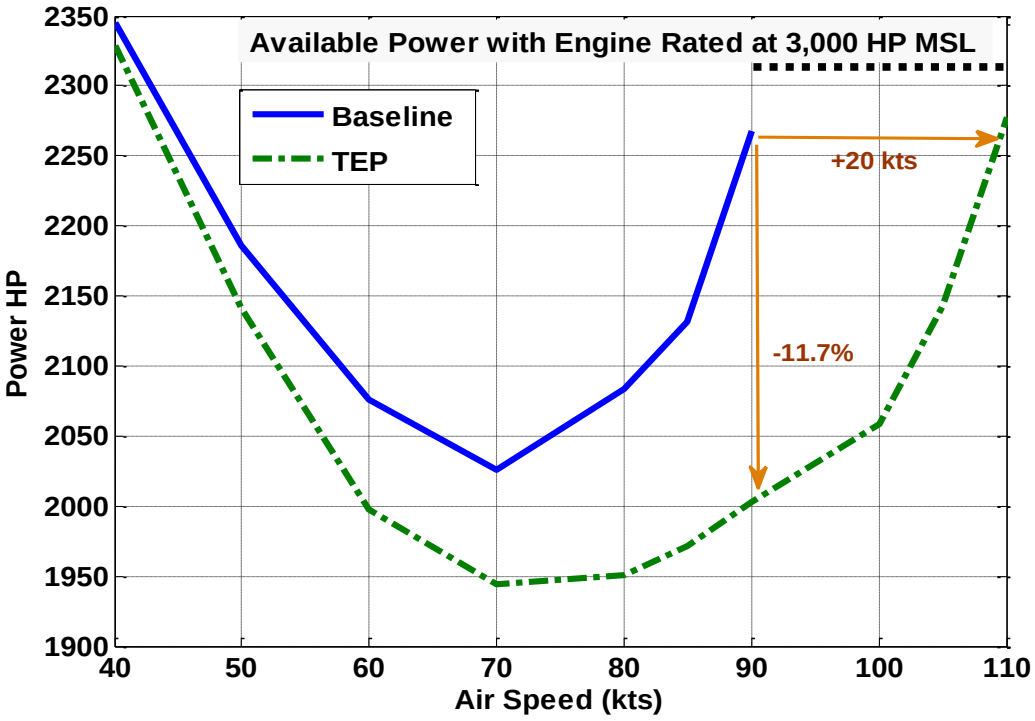

Figure 1-10: Helicopter power as a function of forward speed for baseline and extended trailing edge configurations at 8,000 ft altitude and 24,000 lbs gross weight (Ref. 8).

Interestingly, it was shown that while the trailing edge plate configuration successfully reduced the angles of attack on the retreating side by approximately 2° - 4°, the collective pitch of the blade was only lowered 0.3° (Figure 1-8). The authors attributed these lower angles of attack to the elastic blade twist as a result of the increased nose-down pitching moments at the trailing edge plate section. Accordingly, the reduction in the angle of attack on the retreating blade led to a significant reduction in the drag, especially over the outer rim of the blade (Figure 1-9). This effect was determined to be primary contributor in the reduction in the main rotor power. Figure 1-10 shows the marked improvement in helicopter performance using the extended plate concept. For the given configuration, the maximum forward speed was increased from 90 kts to 110 kts. Alternatively for the same forward flight speed a power reduction of up to 11.7% was realized.

These works have clearly demonstrated the need for a morphing blade structure capable of providing this extended trailing edge plate concept.

1.2.3 Extendable Chord Technology

While there has been much research into various morphing blade technology, the concept of extendable chord sections is still relatively new. Some of the earliest work on rotorcraft chord extension was conducted by Noboru et al. at the Japan Aerospace Exploration Agency (Refs. 9, 10). This study presented an active tab actuated at higher harmonics for rotor noise reduction. The mechanism, shown in Figure 1-11, consisted of a triangular, flat plate pivoted at the trailing edge of the blade and deployed at a 10° angle of incidence. The system achieved a 20% chord extension (at the tip of the plate), deployed at a frequency of 20Hz. Plate motion was driven a rack and pinion apparatus inside the blade that was connected to a push-pull rod spanning from the active tab to the root. The push-pull rod was actuated via swashplate by a higher harmonic control (HHC) motor mounted in the fixed frame. Unfortunately, more details of the active tab's internal mechanism have not been published.

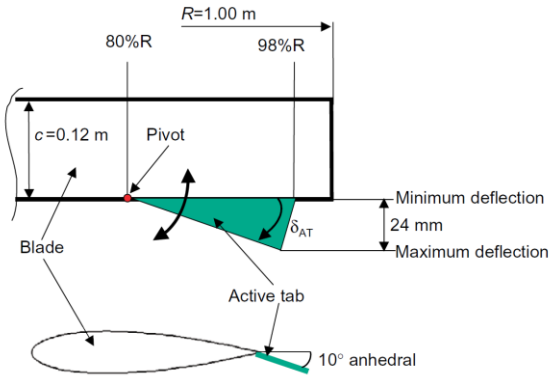

(a)

(b)

Figure 1-11: Active tab (a) schematic and (b) blade installation (Ref. 10).

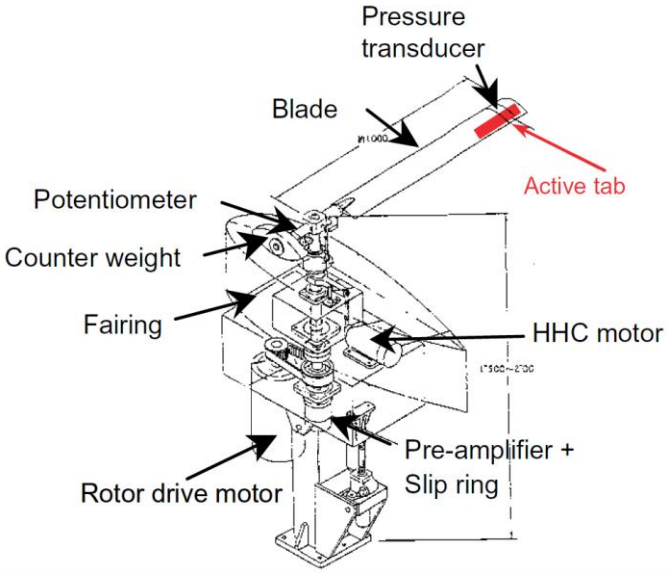

Figure 1-12: Active tab rotor system setup (Ref. 10).

In 2010, researchers at the United Technologies Research Center developed an active trim tab for onboard rotor tracking (Ref. 11, 12). Similar to the current work, this device was not meant to be actuated at higher harmonics. The device, shown in Figure 1-13, was designed to produce ±5° of tab deflection under high centrifugal accelerations. The system uses a custom-built electromechanical actuator which was capable of supplying the maximum required force of 16 lbs. The study addressed the high-g actuation challenges by spinning the prototype at rotational speeds up to 900 RPM on the 36 in radius rotor stand (Figure 1-14). This corresponded to a centrifugal acceleration of approximately 500 g's. The work presented in this thesis follows a similar test procedure for simulating the centrifugal loads.

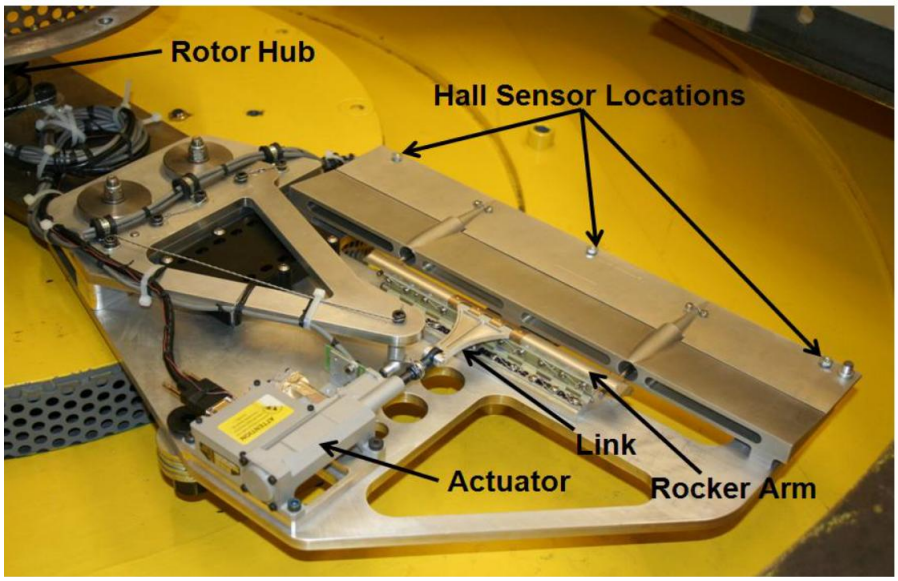

Figure 1-13: UTRC trim tab prototype (Ref. 11).

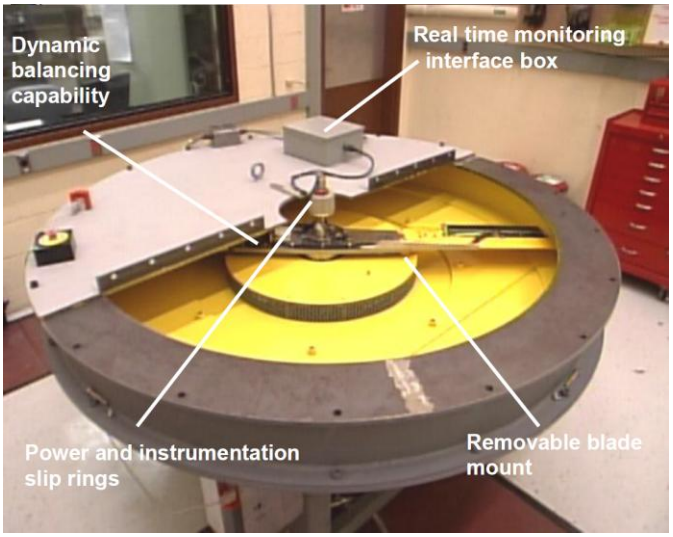

Figure 1-14: UTRC spin test facility (Ref. 11).

Another concept for a rotor blade chord extension, presented by Johnson, involved the use of a bistable arch, as shown in Figure 1-15 (Ref. 13). As opposed to actively controlling the position of the system, this design utilized the bistable nature of the arch to hold the plate in either the retracted or extended equilibrium states. This work presented the use of a SM495 Nitinol shape memory alloy wire as a means of initiating snap through (Figure 1-16).

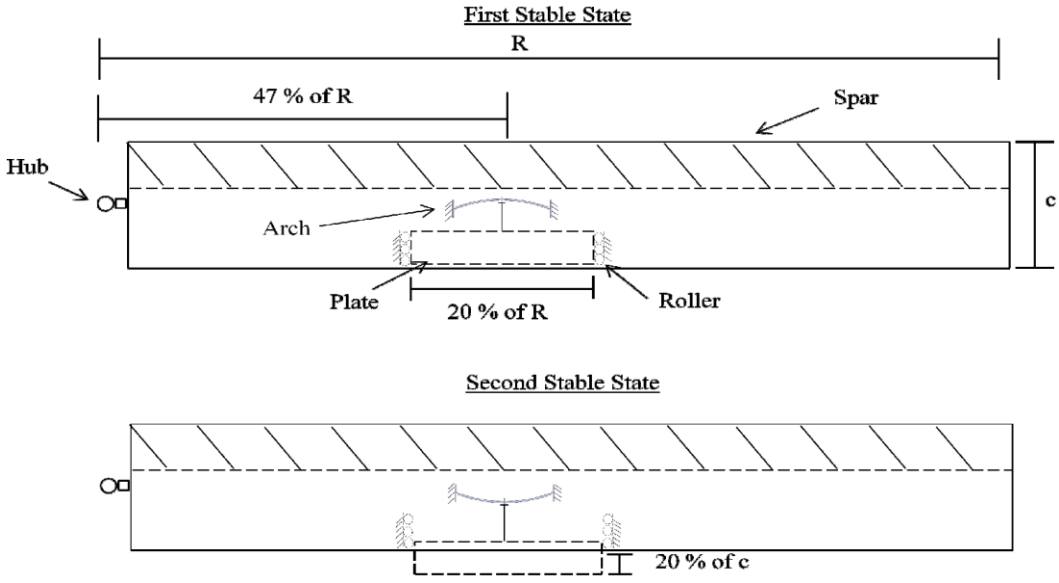

Figure 1-15: Bistable arch chord extension concept (Ref. 13).

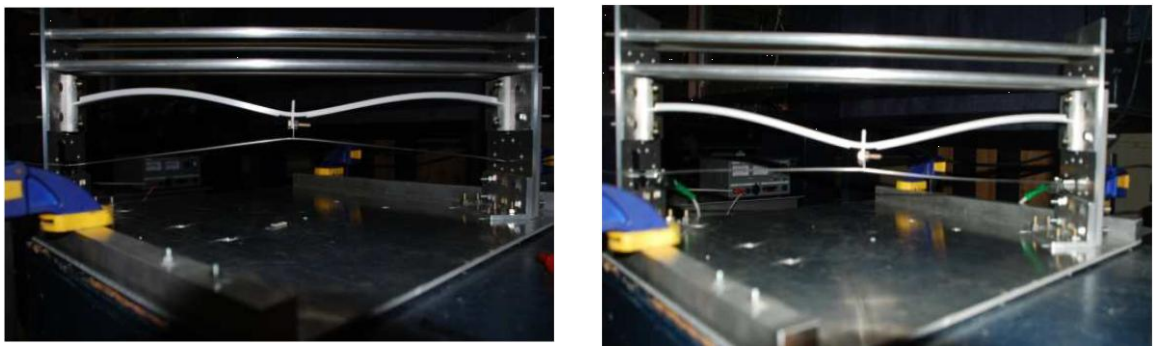

(a) (b)

Figure 1-16: Bistable arch actuation via shape memory alloy wires in the (a) initial and (b) final configurations (Ref. 13).

The advantage to this design is its ability to supply a large stroke while requiring a limited actuation force. The simplicity in design and lightweight nature also make it particularly attractive. On the other hand, due to its bistability, the system can only maintain position in either the fully retracted or fully extended configurations which may prove to be a disadvantage in operation. Furthermore, the author recognizes the need for a modified actuation concept due to the lengthy cool down time of the shape memory alloy.

An alternative approach to an extendable chord device was developed by Barbarino et al. (Ref. 14). Similar to the work conducted by Johnson, this system employs a continuum morphing mechanism rather than discrete elements, such as the rack and pinion apparatus used by Noboru. However, this concept consists of a cellular structure as a means of facilitating extension and does not exhibit bistability. Furthermore, this concept more closely represents true chord extension than previous designs. A continuous change in the blade cross-section is achieved rather than deploying a flat plate from a slit in the trailing edge.

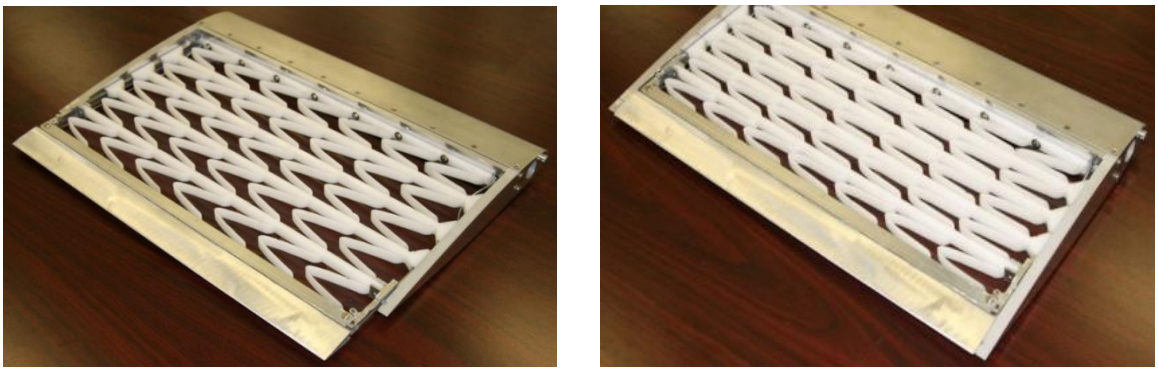

(a) (b)

Figure 1-17: Morphing cellular structure in (a) extended and (b) retracted positions (Ref. 14).

The system is comprised of semi-elliptical ligaments in rows divided by mini-spars along the span. These mini-spars are connected to a flexible skin, not shown, and are designed to carry the out-of-plane loads to maintain the proper airfoil shape. The benchtop prototype shown in Figure 1-17 was fabricated using DELRIN 100ST NC010 polymer for manufacturing purposes. However, analysis was conducted using AL 7075 T6 as the elastic ligament material. The authors also showed that one-way actuation of the system can be used by selecting the extended (or retracted) chord configuration as the neutral state. While actuation of this mechanism could be done via electromechanical motors, linear PZT inchworms, etc., the work suggested passive actuation using centrifugal force may be the most efficient option.

1.3 Current Research Objectives

Obviously, improving helicopter performance is of great importance to the rotorcraft industry, especially in light of the current economic climate. As detailed previously, reducing main rotor power can have significant impacts on helicopter speed, payload, ceiling altitude, endurance, and range. The content of this thesis continues this work by presenting an extendable chord mechanism that is capable of withstanding the high centrifugal loading present in a full-scale rotor blade. As mentioned, the concept is intended to be quasi-statically actuated during flight regimes in which retreating blade stall is present. Building on the previous works, the extended chord will be realized via a flat plate through a slit in the trailing edge of the rotor blade. Furthermore, multiple actuation methods for the system will be investigated.

Subsequent chapters of this thesis will introduce the first design concepts and show the progression to the final prototype. Furthermore, the experimental setup of the extendable chord system on the Pennsylvania State University's Adverse Environment Rotor Test Stand (AERTS) will be detailed. This test was designed to simulate the full-scale centrifugal loading representative of a UH-60 helicopter. The results of this test will then be compared against a numerical analysis of the required actuation force. Finally, conclusions will be drawn about the operability of such a device in a full-scale helicopter blade. Recommendations for future work on this morphing technology will also be presented at the end of this thesis.

Chapter 2

Design Ideology

The various sections of this chapter provide an overview of the design ideology behind the development of the current extendable chord prototype. The initial proof-of-concept benchtop demonstrator is presented along with a discussion of its capabilities and limitations. This is followed by an explanation of the various design challenges when incorporating rotor blade twist. Next, a general concept for the extendable chord prototype which addresses these issues is detailed. Finally, the scaled rotor spin test methodology is explained.

2.1 Initial Benchtop Design

2.1.1 Design Space and Geometric Constraints

Before beginning the design of the extendable chord benchtop demonstrator, it was necessary to develop a clear definition of the overall design space. For the initial concept, the Messerschmitt-Bölkow-Blohm (MBB) BO-105 helicopter blade was selected. The rotor blade specifications are listed in Table 2-1 for this lightweight, multi-purpose utility helicopter.

Table 2-1: BO-105 rotor properties.

Property	Unit	Value
Radius	ft	16.20
Chord	in	10.75
Airfoil		NACA 23012

The small size of this blade ensured that an extendable chord system fitting within these dimensions would not present any problems when applied to larger rotorcraft, such as the UH-60. Obviously, as with any morphing rotor technology, this limited design space presented a considerable challenge. For simplification, the extendable chord concept used an NACA 0012 symmetrical airfoil rather than the cambered NACA 23012 airfoil on the BO 105. Thus, given the 12% thickness ratio, the maximum blade thickness was 1.29 in. Furthermore, the BO 105 C-spar has been switched to a D-spar configuration to provide an attach point for the morphing mechanism. The spar was assumed to extend to the 30% chord location. For the benchtop demonstrator, the spanwise dimension of the actuation system was not subjected to limitations as stringent as the chordwise and thickness dimensions. However, it was preferable for the mechanism to not extend much beyond the spanwise dimension of the extendable chord flat plate from an installation complexity standpoint. For the present study, a 12 in span was selected for the plate and the spanwise dimension constraint on the entire actuation system was set at approximately 25% greater, or at 15.3 in.

Helicopter blades most commonly have a D-spar and it was determined that cutting the spar would have too much of a negative impact on the blade stiffness and strength. Thus the extendable chord mechanism must in no way penetrate the spar, except for small attachment points which would not have a significant impact. Therefore, with the rear of the spar assumed at 30% chord, the remaining 70% (7.53 in) of the chord was available for the extendable plate and the actuation mechanism. Figure 2-1 provides schematics of the design space for the system in the retracted and deployed states.

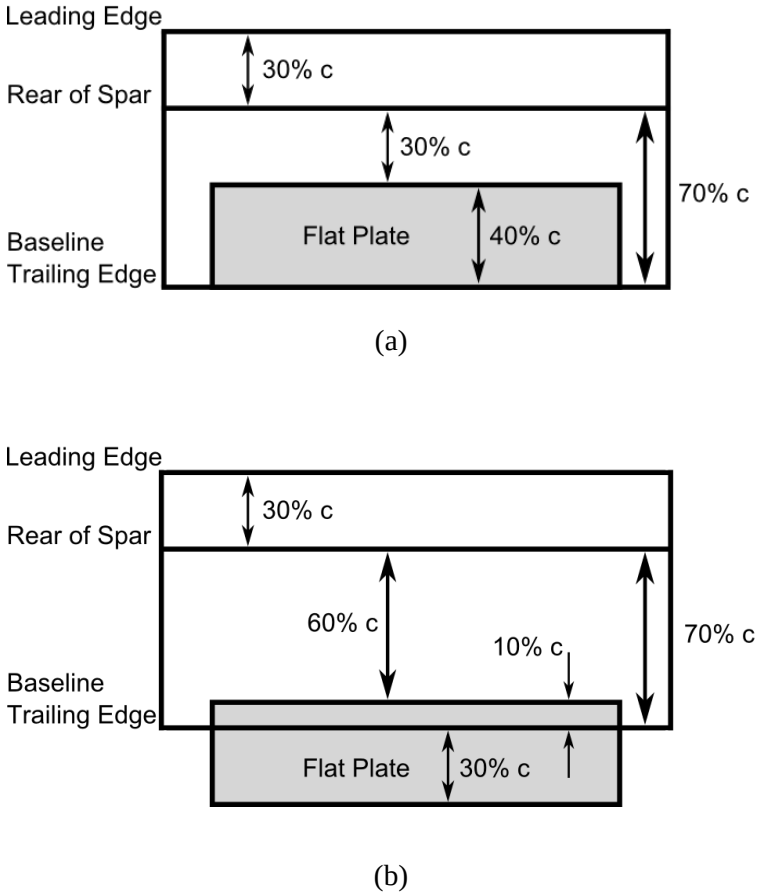

Figure 2-1: Benchtop prototype design space in the (a) retracted and (b) extended configurations.

The desired extension of this demonstrator was 30% chord, and with some overlap desired in the deployed configuration, the chordwise dimension of the plate was set at 40% chord (3.58 in). That left 30% chord (3.23 in) for the actuation mechanism itself in the retracted configuration, since the extendable plate must be entirely contained within the airfoil. Therefore, in the extended configuration, the space for the actuation system was 60% chord. In other words, the actuation system must extend from 30% chord in the stowed condition to 60% chord in the deployed condition.

2.1.2 Morphing Truss Actuation System

Considering the limited chordwise dimension and the tapering thickness towards the trailing edge, it was challenging to design a mechanism which could directly drive the plate in the chordwise direction. Research conducted by Rufino et al. at the Pennsylvania State University on morphing hull concepts for unmanned underwater vehicles was used as an inspiration for the current design (Ref. 15). This work presented a method of increasing the hull diameter of an underwater vehicle using linkages driven axially by a jackscrew device (Figure 2-2).

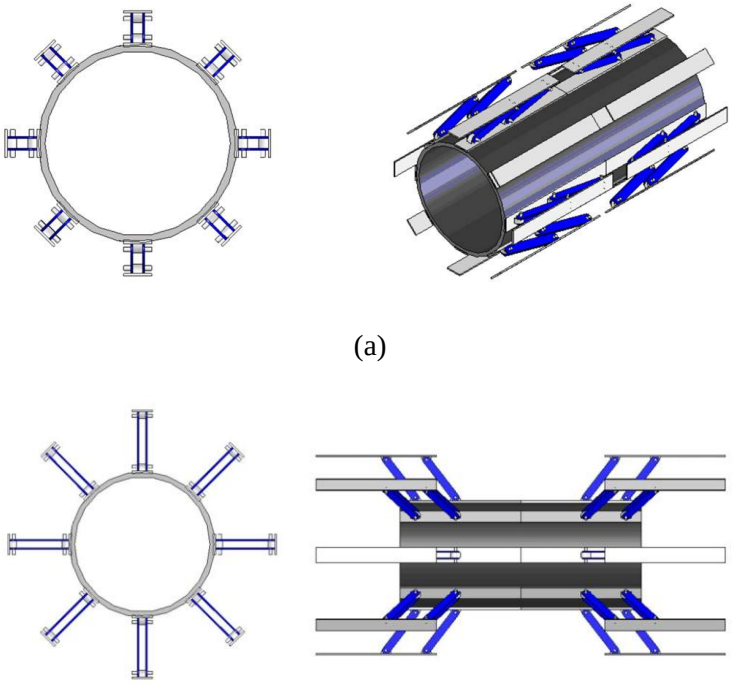

Figure 2-2: (a) Retracted and (b) expanded morphing hull truss structure (Ref. 15).

Applying this concept to the extendable chord system would allow spanwise input displacements to be transferred into the chordwise direction; thus providing more room for actuators in the spanwise direction as well as taking advantage of the thickest part of the airfoil close to the spar. Also, by placing the heavy actuator along the spar, the shift in the center of

gravity towards the trailing edge is reduced which is advantageous for blade stability. Given the current design space, a morphing truss was to be inserted between the rear of the spar and the plate. The truss structure must then occupy 30% chord in the retracted configuration and extend to 60% chord length in the fully-deployed configuration. Preliminary sketches of some possible truss systems are shown in Figure 2-3 through Figure 2-5.

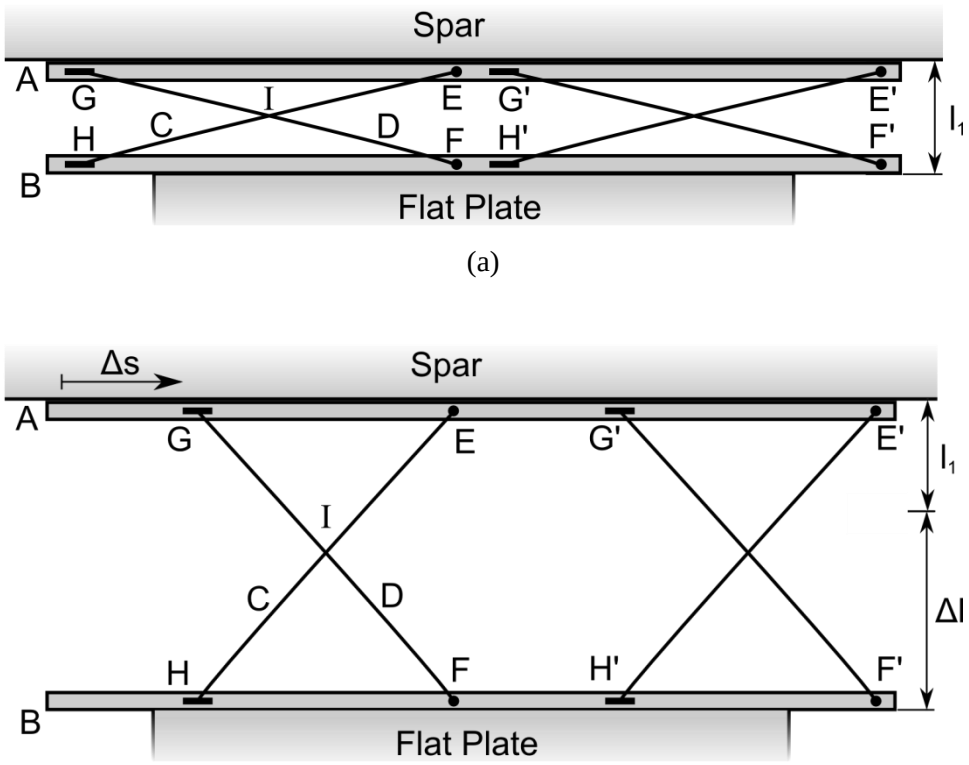

Figure 2-3: The inline X-truss in (a) retracted and (b) extended configurations.

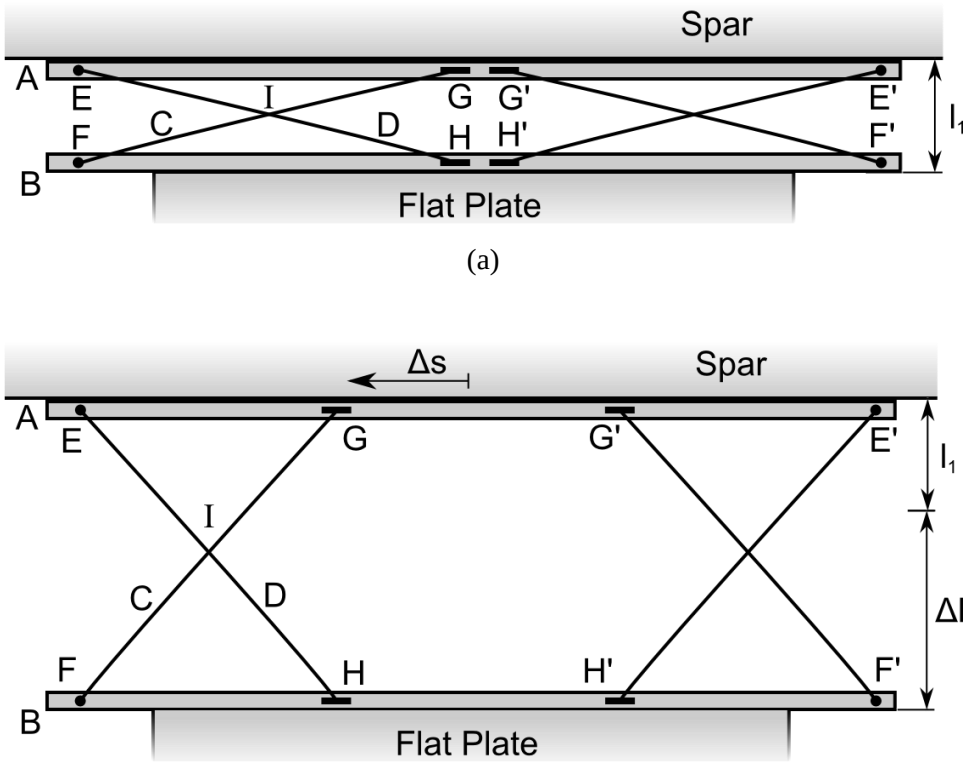

Figure 2-4: The symmetric X-truss in the (a) retracted and (b) extended configurations.

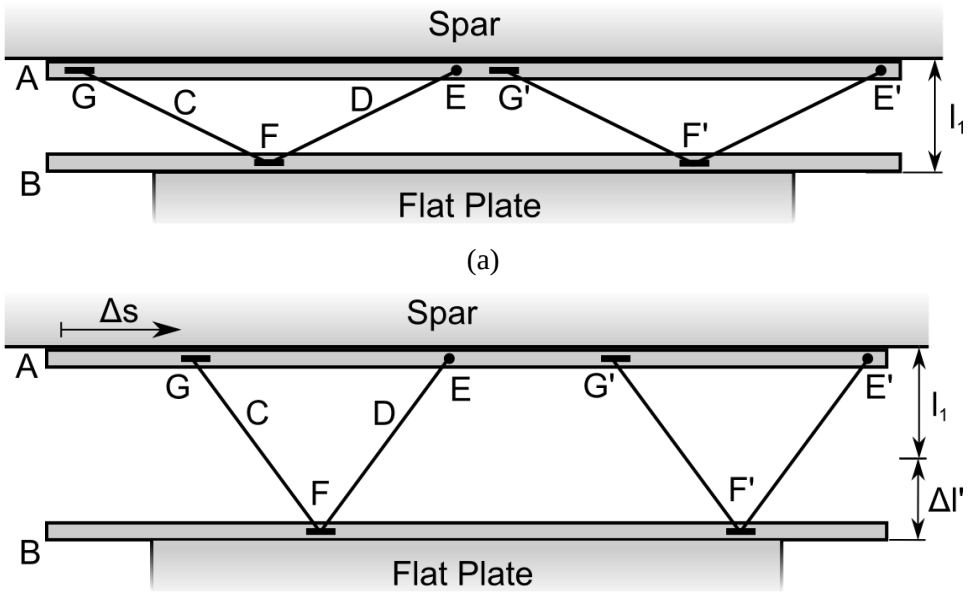

Figure 2-5: The triangular truss in the (a) retracted and (b) extended configurations.

For each of the three designs two repeating units were considered for improved stability. Each included a railing, A, attached to the rear of the spar and a railing, B, attached to the extendable plate. For the inline and symmetric X-trusses (Figure 2-3 and Figure 2-4), points E and F were pinned to the rails which allowed cross-braces C and D to rotate about points E and F, while restricting translation on the rails. The cross-braces were pinned at junction I, and constrained to slide along the rails at points G and H. An actuator was to be connected to point G (the driven point) whereas point H translated due to the kinematic constraints. For the triangular truss (Figure 2-5), the members C and D were pinned at junction F and only point E was pinned to rail A. Point G was again driven along rail A causing point F to slide along rail B due to kinematic constraints. It was determined that to keep actuation requirements low, the spanwise actuation stroke, Δs, required to obtain a certain deployment, Δl and $\Delta l'$, should be minimized. Figure 2-6 shows the chordwise displacement as a function of the spanwise stroke for the X-truss and the triangular truss. Note that in these figures the length of the linkage has been normalized to provide a direct comparison between each system. Alternatively, Figure 2-7 shows a similar plot with an equivalent spanwise dimension for either system in the retracted configuration. Thus, the linkage for the triangular truss was required to be half as long as that for the X-truss. This can be easily understood by thinking of the triangular truss as one half of the X-truss. From the figures it is clear that for either configuration, the X-truss provides a greater amount of chordwise extension for a given spanwise input stroke.

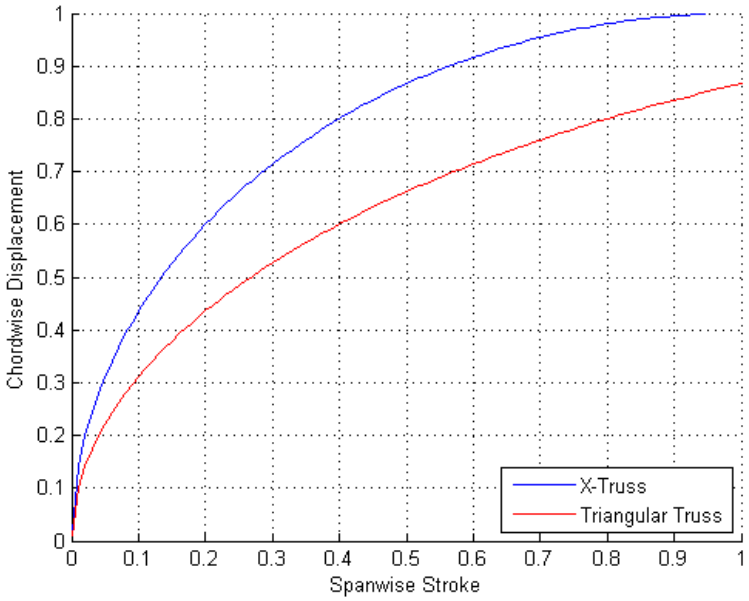

Figure 2-6: Comparison of actuation authority for X-truss and triangular truss with equivalent linkage lengths.

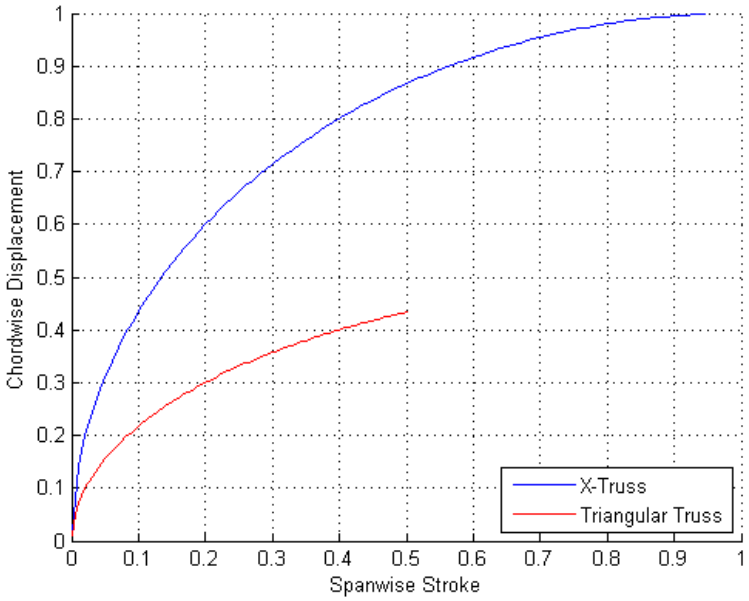

Figure 2-7: Comparison of actuation authority for X-truss and triangular truss with equivalent spanwise dimensions.

Of the two X-trusses, the inline X-truss was selected as moving the points G and G' in the same direction was more convenient. This was to be done by attaching points G and G′ to threaded blocks which are translated along rail A through the rotation of an all thread rod running parallel to the spar. This rotation is controlled by the electromechanical DC motor located in the pocket next to the extendable chord system. As points G and G′ slide, the truss transforms to the extended configuration shown in Figure 2-3b.

2.1.3 Final Benchtop Design

The final benchtop design is shown in Figure 2-8. As seen, cross-brace C is a single inner brace but cross-brace D comprises of two outer braces. This was done to increase structural stability by providing a symmetrical load path. The step in the outer cross-braces was introduced to accommodate its operation as the thickness of the airfoil decreases towards the trailing edge. Another important feature to note is the linear slides connected to the ribs. These are meant to support the in-plane and out-of-plane inertial and aerodynamic loads that will be present in the rotating blade. By reducing the loads on the truss itself, the overall friction as well as the risk of binding should decrease, thus lowering the actuation forces.

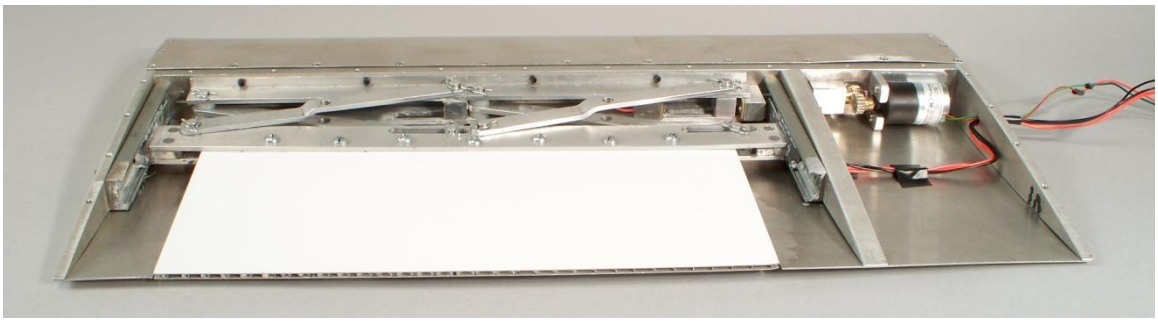

(a)

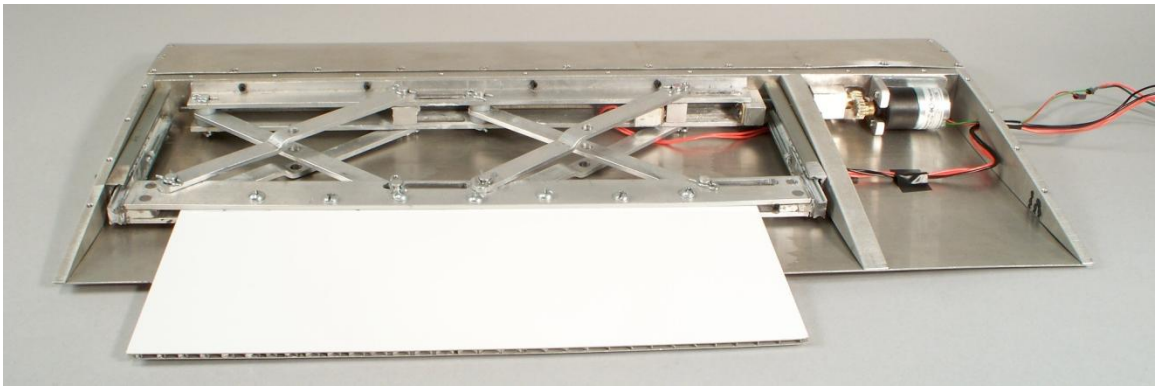

(b)

Figure 2-8: Benchtop prototype in the (a) retracted and (b) extended configurations.

The fabrication of the physical model was separated into two parts: blade structure and the morphing X-truss mechanism. The blade structure includes the spar, ribs, and skin. The ribs were machined out of aluminum using a water jet cutter and are screwed into the spar. The skin is made of aluminum sheet that has been bent to the contour of the airfoil and connected to the ribs and spar via countersunk screws. The division of the skin into leading edge and trailing edge sections allows for easy access to the extendable chord mechanism. Along the spar, two rows of screws, spaced 2 in apart, connects both the leading edge and trailing edge skin sections. A slit has been cut out along the trailing edge of the skin to allow the extendable plate to slide in and out of the blade. The flat plate is bolted to the trailing-edge railing and the pins that connect the cross-braces and railings are secured using hair pin clips. The linear slides and spar railings have been bolted to the ribs and spar, respectively. The entire assembly is driven by a #8-32 aluminum

threaded rod connected to the DC motor using a 1:1 gearing ratio. The motor used in this model is the 1271 brushed DC motor manufactured by Mclennan Servo Supplies Ltd. Specifications for this motor are listed Table 2-2.

Table 2-2: Geared DC motor specifications, model 1271-12-90 (Ref. 16).

Property	**Unit**	**Value**
Length	mm	41
Gear Ratio		90:1
Nominal Voltage	VDC	12
No-load Speed	RPM	30
Rated Speed	RPM	18
Rated Torque	N-cm	1.5
Max No-load Current	mA	20
Rated Current	mA	50
Mass	G	58
Max Radial Shaft Load	N	10
Max Axial Shaft Load	N	5

2.1.1 Benchtop Demonstrator Capabilities

Overall, the benchtop demonstrator has a spanwise length of 20.5 in, the mechanism itself occupying 15.3 in. In the fully retracted state, the mechanism, less the flat plate, has a chordwise dimension of 2.25 in. At full extension, the spanwise displacement, Δs, is 1.5 in which produces a chordwise extension of 3 in. This corresponds to a 28% increase over the baseline chord, very close to the initial goals for this design. However, due to the small thickness of this blade, it was difficult to find a motor capable of supplying the required torque while, at the same time, providing a high speed. Ultimately, the system fully deploys in approximately 1 minute 18 seconds. While acceptable for a benchtop demonstrator, this clearly illustrated the challenges in using an electromechanical actuation system in a morphing rotor technology. Also, significant friction and binding was observed in this system. For this reason, the pinned joint between the three linkages at the center of the X-truss was removed, although this did not affect the overall

extension of the system. Moreover, it was anticipated that at full-scale loads and vibrations, the retaining clips at the pinned joints would likely fail. Lastly, while adequate for the proof-of-concept prototype, the threaded rod actuation method generated a large amount of friction which would most likely be worsened at full-scale loading in a centrifugal environment. All of these issues were taken into serious consideration in subsequent designs.

2.2 Twisted Blade Design Concept

2.2.1 Twisted Plate Extension

While the initial prototype demonstrated the possibility of an extendable chord system in a rotor blade, there had been several significant simplifications in the design process that cannot be made in a flight-worthy device. For instance, with rare exception, most helicopter blades incorporate a nose-down twist variation along the radius. Even with moderate amounts of twist, the lift can be redistributed to significantly increase the aerodynamic efficiency of the blade. The simplest, and often most popular, method is to incorporate a linear twist variation from the root to the tip. Therefore, in any morphing rotor technology, it is necessary to consider this effect.

Before designing an extendable chord mechanism, it was necessary to determine if it is even possible to extend a flat plate from the trailing edge of a twisted section. An exaggerated representation of this concept is shown in Figure 2-9. Fortunately, by twisting the flat plate with the same rate of twist as the surrounding blade section, it is possible to extend the plate continuously from the trailing edge of the airfoil.

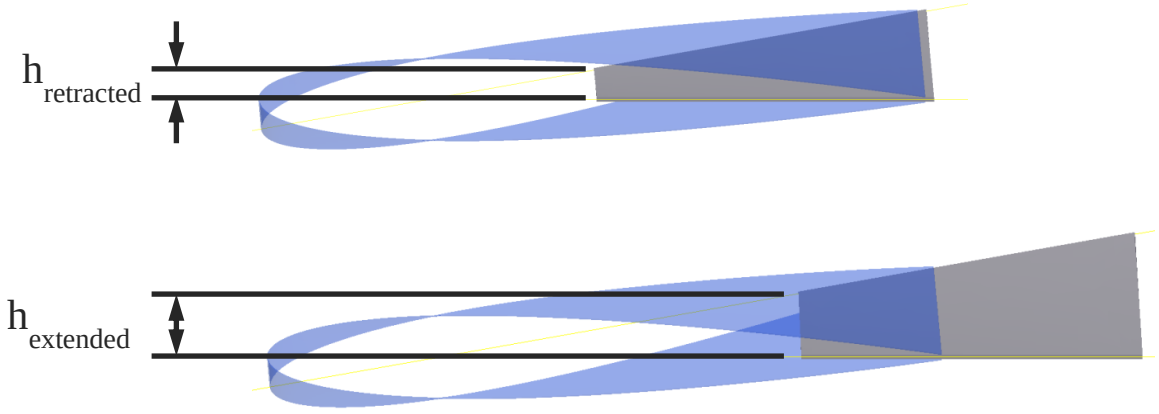

Figure 2-9: Twisted plate concept in the (top) retracted and (bottom) extended configurations.

This simple figure also demonstrates some of the fundamental differences between a twisted and an untwisted blade section which will be described in detail in the following paragraphs. In fact these differences make it impossible to implement any design which includes multiple actuation linkages, such as the X-truss. Therefore, for the twisted design the X-truss system was modified to include only a single linkage that transfers the spanwise displacement into chordwise extension which will be discussed further in the following section.

2.2.2 Single Link Truss Concept

The single link truss concept, shown in Figure 2-10, is nearly identical to the X-truss concept except for the obvious omission of the second linkage. Furthermore, while the second linkage was included for increased stability, it was not necessary from an actuation standpoint and therefore did not have a significant impact on the overall design. Similar to the previous design, point A is displaced in the spanwise direction by an external actuator. Rigid member AB then transmits this motion to the single linkage BC. The linkage then transfers the spanwise

displacement into chordwise extension of points D and E. These two points are supported on either rib using linear motion slides.

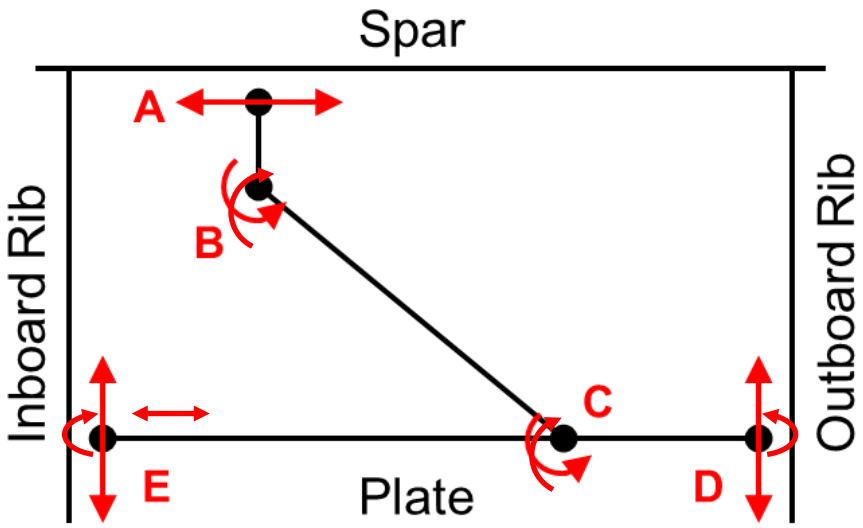

Figure 2-10: Single link system for an untwisted blade section.

When applying this concept to a twisted section, several key differences arise. First, as the plate is extended, it must also rotate about the chordwise axis to maintain smooth deployment through the trailing edge. This is illustrated in Figure 2-9 by the change in out-of-plane distance between the two corners of the plate towards the leading edge. Thus, chordwise rotation elements must be included at points D and E. Secondly, consider the distance between points D and E as the hypotenuse of a right triangle. With a fixed spanwise distance between the ribs, as the height of the triangle is increased from $h_{retracted}$ to $h_{extended}$, the hypotenuse must also increase. Therefore, the twisted blade system must incorporate an extension element along the line connecting points D and E. Finally, the out-of-plane motion of the linkage must be accounted for using three-axis rotation rod ends at points B and C.

As the plate is extended, points D and E move to point D' and E', respectively. Since these points must follow the local chordline and the spanwise distance S is constant, the out-of-plane distance between D' and E' must increase. Moreover, from simple geometry, it is obvious that the distance between D' and E' is greater than the distance between D and E. Consequently, points D and E must slide in the chordwise direction as well as allow for a rotation about the local chordwise axis and incorporate an extensional element to account for the change in length. In addition, points B and C must now allow for rotation about all three axes.

Up to this point, the twisted design concept has been kept intentionally generic. This was done to ensure the operability of this system in any linearly twisted blade and can accommodate multiple actuation methods. Following the benchtop prototype, it was clear that a thorough investigation of possible actuators must be conducted. For the present study, both electromechanical and pneumatic actuators were considered due to their force output and speed capabilities as well as the capabilities of the available test facility. As this work does not focus on actuator design, only commercial, "off-the-shelf" products were considered.

2.3 Experimental Setup

2.3.1 Test Facility

As stated previously, the goal of this study was to evaluate the operability of an extendable chord system in a full-scale centrifugal field. This experiment was conducted using the Adverse Environment Rotor Test Stand at the Pennsylvania State University (Figure 2-11). Some of the relevant data on this facility has been compiled in Table 2-3.

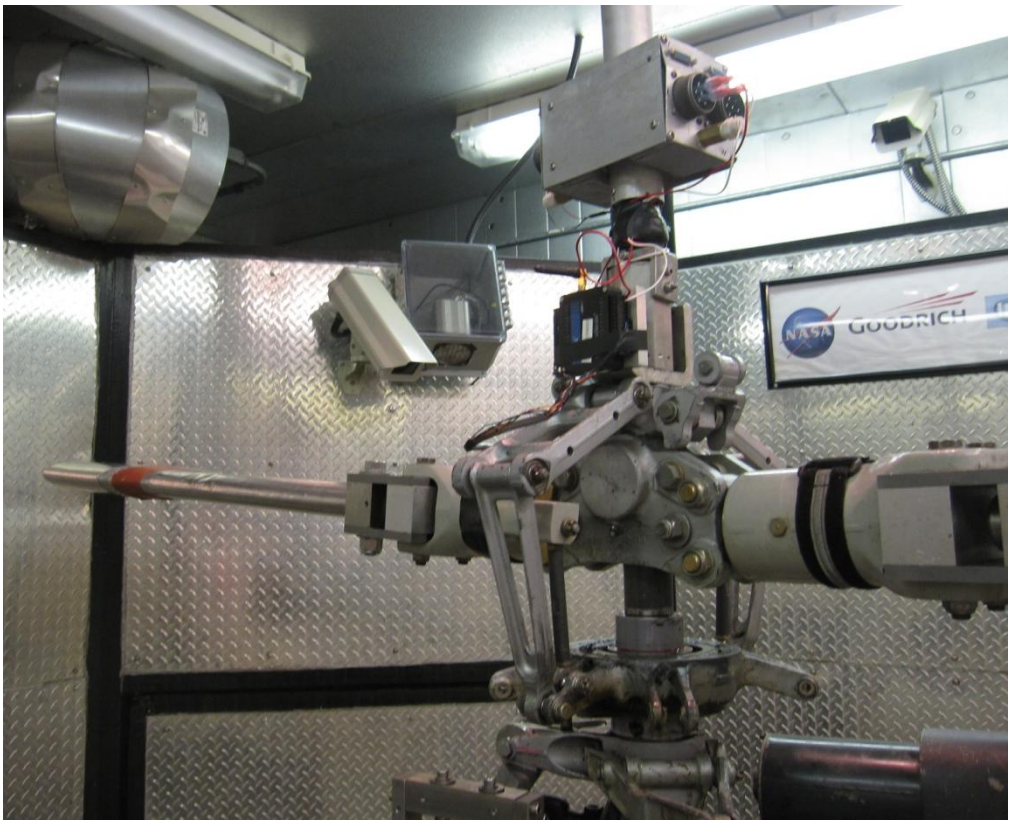

Figure 2-11: PSU AERTS facility.

Table 2-3: AERTS facility capabilities (Ref.17).

Property	**Unit**	**Value**
Motor Power	hp	84 (unlimited), 120 (3 minute limit)
Motor Torque	in-lbs	696 (unlimited), 995 (3 minute limit)
Rotational Speed	RPM	1,000
Rotor Tip Radius	ft	4.5
Blade Grip CF Load	lbs	12,000
Hub Precone	°	3
Slip Ring Power Channel Voltage	V	800
Slip Ring Power Channel Current	A	15
Slip Ring Signal Channel Voltage	V	100
Slip Ring Signal Channel Current	A	2
Shaft Torque Sensor	in-lbs	1,500
Maximum Air Pressure	psi	105

This facility includes an electrical slip ring and pneumatic rotary union. The electrical slip ring has 24 power channels and 24 signal channels. On the other hand, the pneumatic rotary

union has two channels, one of which is connected to an air compressor while the other is left open to atmospheric pressure. Although the compressor is capable of providing very high pressures, the maximum pressure is limited to 105 psi to ensure the safety of the slip ring at higher rotational speeds.

The rotor hub installed in the facility is based on the QH-50. In addition to the rotor stand itself, the facility also provided the inner blade structure to which the extendable chord test section was attached. This structure, shown in Figure 2-12, consists of three major components: blade grip, small-chord midsection, and fairing.

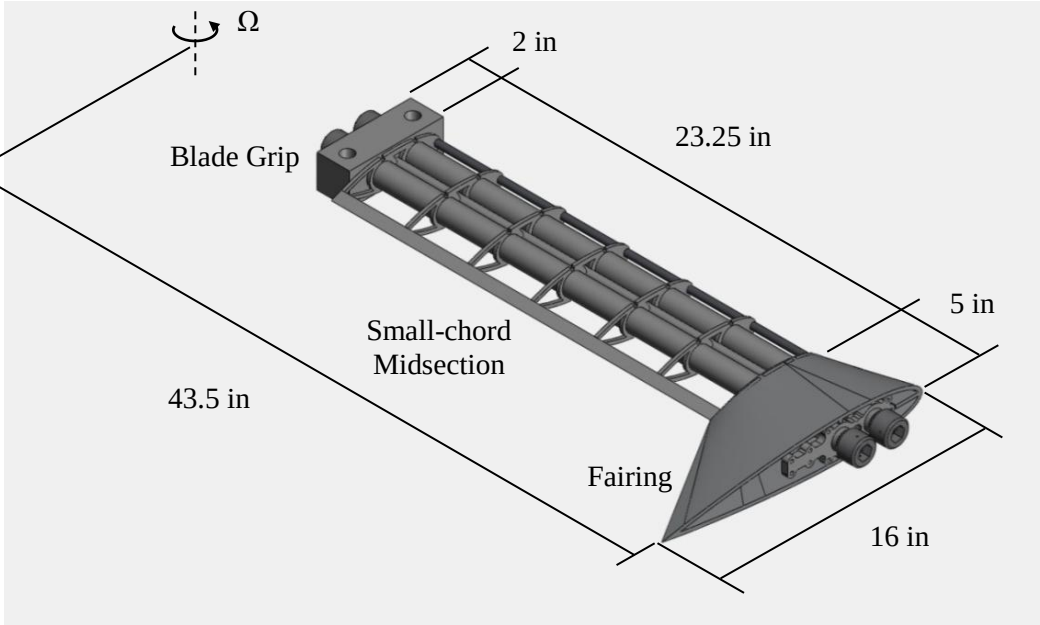

Figure 2-12: AERTS inner blade structure.

The blade grip is simply a solid block of aluminum which attaches the blade to the hub. The midsection has two 1.25 in diameter solid aluminum rods acting as the main spar and seven aluminum ribs. Between the two spar rods is an aluminum pipe which is used as a conduit to pass electrical wires from the hub to the test section. The leading edge also has a 0.375 in diameter tungsten rod to move the center of gravity of the blade forward for improved stability. Although

not shown, this portion is wrapped in aluminum sheet to provide the airfoil shape. Finally, the aluminum fairing provides a smooth transition from the 6.5 in chord midsection to the test section which has an NACA 0015 airfoil with a 16 in chord. The two spar rods are continuous from the blade grip through the fairing and are bolted to the test section using 1”-8 bolts. Furthermore, there is a small aluminum adapter inside the fairing which attaches to the test section to provide a more secure connection. The 30.25 in span of the inner blade section combined with the distance from the blade grip to the hub yields a 43.5 in radius from the test section to the center of rotation. The weight of these components contributes significantly to the maximum hub centrifugal loads.

2.3.2 Centrifugal Prototype Design Space

As shown, the test section is joined to the inner blade by an aluminum fairing. Thus, the extendable chord test section must use an NACA 0015 airfoil with a 16 in chord in order to match the profile of the fairing. Given the radius of the inner blade section and the maximum radius allowable inside the facility, the test section span was constrained at a maximum of 12 in total. While much of the design process focused on adapting the extendable chord system to a twisted blade, test section in this study does not include twist for manufacturing simplicity. However, it is important to note that all of the components required by a twisted blade have been included in all designs. The structural shell includes the ribs, spar, and skin (Figure 2-13).

Figure 2-13: Extendable chord system structural shell without aluminum sheet skin.

As with the benchtop demonstrator, the design space is limited to the space aft of the spar to minimize impact on the blade's structural properties. The space forward of the spar may only be used to secure the extendable chord structure and connect the test section to the inner blade (as a side note, this area was also used in the final prototype to house the various electrical wires).

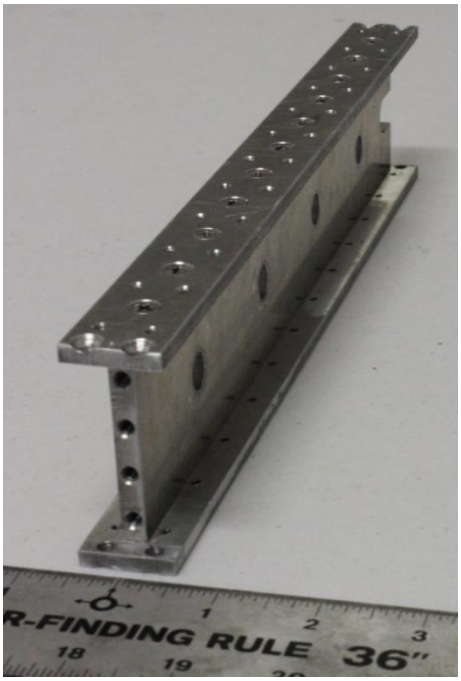

Figure 2-14: Spar structure for extendable chord system.

Figure 2-15: Outer (top) and inner (bottom) ribs of extendable chord system.

The fabrication of this structural shell is similar to the benchtop demonstrator. The test section spar is shown in Figure 2-14. The spar is shaped as an I-beam and consists of two horizontal flanges attached to the vertical web using countersunk screws. Each component is made of aluminum, Al 6061. Both inner and outer ribs are also cut from Al 6061 using a water-jet cutter and have a thickness of 0.25 in (Figure 2-15). The two large holes in the inner rib are for the two 1”–8 bolts which secure the test section to the inner blade. The ribs have been screwed to the vertical web and each horizontal flange. With an overall span of 12 in and 0.25 in thick ribs, the internal design space has a spanwise dimension of 11.5 in. In addition, with the spar located at the quarter-chord location, the chordwise dimension of the mechanism is limited to 11.875 in. However, much of this space towards the trailing edge is strictly limited due to the decreasing thickness.

2.3.3 Test Conditions

In order to determine the appropriate conditions for this test, it was necessary to select a baseline helicopter for comparison. To maintain consistency with aerodynamic and performance

work on this technology, the experiment aimed to match the centrifugal forces present in a UH-60 with an extendable chord system centered around 73% blade radius (Ref. 8). Table 2-4 was created to determine the rotational speed required to match the full-scale loads given the rotor properties of the UH-60 and the capabilities of the AERTS facility.

Table 2-4: Centrifugal acceleration for UH-60 and AERTS rotors.

Property	**Unit**	**UH-60**	**AERTS Full-Scale CF**	**AERTS 80% CF**
Rotational Speed	RPM	257.83	560.40	500.00
Rotor Radius	ft	26.83	4.67	4.67
Spanwise Position of Ext.	r/R	0.73	0.89	0.89
Chord System	ft	19.59	4.15	4.15
Centrifugal Acceleration	g's	443.83	443.83	353.31

As shown, to achieve full-scale centrifugal acceleration, 444 g's, the extendable chord test must be run at 560 RPM due to the reduced radius of the device. While this is within the 1,000 RPM limitations of the AERTS, the maximum attainable rotational speed was limited to 500 RPM (80% full-scale centrifugal acceleration) due hub forces and vibrations. Subsequent design work has been conducted based on 500 RPM rotational speed.

Furthermore, before beginning the design of the prototype, it was necessary to determine the desired output data. Obviously, as this test is aimed at proving the operability of an extendable chord system, the plate extension is of particular interest. Moreover, measurements of the actuator stroke and force would provide a better understanding of the mechanism's efficiency. Finally, to accurately assess the input energy requirements, the voltage and current or pressure should be measured for the electromechanical and pneumatic actuators, respectively. This information will be collected on-board and transferred from the rotating frame to the fixed frame using either the signal channels of the slip ring installed in the AERTS facility or a wireless transmitting device.

Chapter 3

Centrifugal Test Prototype: Electromechanical Actuator

This chapter covers the design and test of the centrifugal test prototype of the extendable chord system using an electromechanical actuator. It has been shown that electromechanical actuators can be particularly desirable for morphing rotor blade technologies. Not only do electromechanical actuators have the ability to produce very high torque densities, but they have also been proven to perform well in high-G conditions (Ref. 11, 12). However, it is important to note that a significant amount of research effort went into the development of the actuator used in this work. For cost considerations, the current work focuses on off-the-shelf electromechanical actuators. The subsequent sections address the requirements for the extendable chord concept as well as the specific requirements for this test. The design process is then outlined. This includes a numerical estimation of the system loads leading to the selection of appropriate structural components as well as a finite element analysis of the test section structural shell. Finally, a presentation and discussion of rotor test stand results is provided.

3.1 Design Requirements

As with any morphing rotor technology, the extendable chord system must meet a certain set of requirements. First and foremost, the device must be able to withstand the significant loads

present in the rotating environment. For this concept, the inertial, centrifugal loads constitute a large majority of the overall loads on the system which has become the genesis of this work. Secondly, the device must provide a substantial aerodynamic benefit. As previous work has shown, a chord extension on the order of even 10% has demonstrated performance improvements at the outer edges of the flight envelope. Thus, the design should exhibit at least a 10% chord increase with a goal of 20%. Furthermore, the design should maintain stability in the event of an actuator failure. Lastly, the design should have minimal impact on the existing blade. This would ensure that this technology could be implemented on current helicopters without requiring a complete redesign of the rotor blades. By limiting the extendable chord system to the space aft of the spar, the effect on the blade structural properties should be reduced. The weight of the system should also be minimized as this affects blade stability. As the weight of the blade section aft of the spar increases, the local center of gravity moves aft which can have a detrimental effect on blade pitch-flap stability. Due to the high torsional rigidity of the AERTS blade structure and by implementing a 0° angle of attack during this test; however, blade stability was not anticipated be an issue for this test and thus was not a priority during the design of the extendable chord system. However, while this work does not specifically address this issue, the weight of the system has been considered during every step of the design process.

3.2 Initial Electromechanically Actuated Design

In order to ensure the safety and operability of the extendable chord device, it was necessary to develop a method of estimating the loads present in the rotating frame. This is an iterative process since the loads depend on the component design and the component design depends on the loads. Figure 3-1 shows the first design iteration.

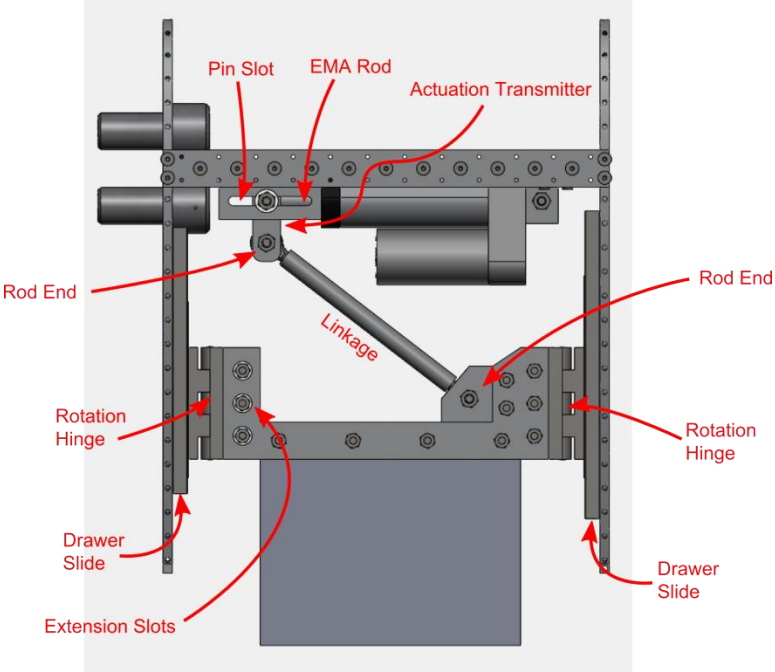

Figure 3-1: First iteration of the electromechanically actuated centrifugal test prototype with partial plate deployment.

As shown, the system incorporates each of the necessary design elements for a twisted blade section. Heavy duty drawer slides have been used to allow the chordwise motion of the plate while a slotted pin along the spar is used for the actuator motion. An actuation transmitter has been included in the design which moves the rotation point of the linkage further aft of the spar to provide more space for the electromechanical actuator. The EMA dimensions are based upon a generic actuator which has been used in previous studies. A specific actuator will be selected after determining actuation requirements and may have a different geometric profile. Rod ends have been attached to either end of the linkage which allow for the required rotation about all three axes. The extension plate has been clamped between two pieces of metal which also provide support for the linkage rod end and the rotation hinges. The extension element has been incorporated using slots in the plate assembly which connect to the inner hinge.

3.2.1 Load Estimation

Based on the geometry and mass properties of this initial design, it was possible to create the following force and moment analysis.

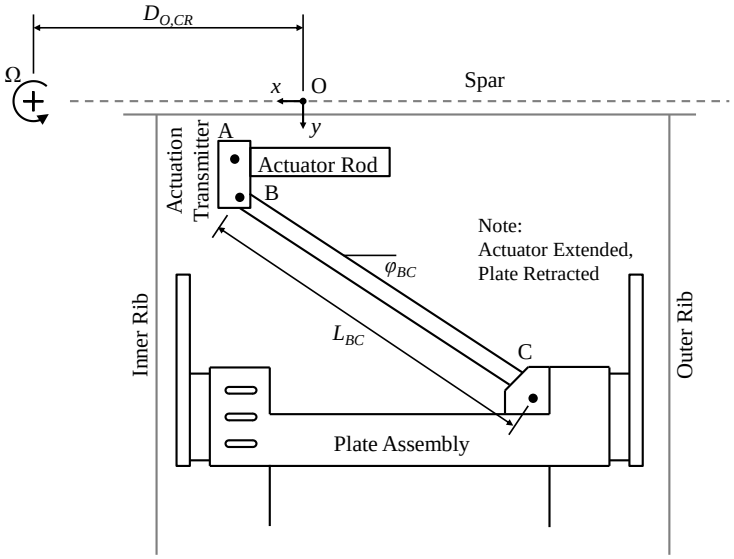

Figure 3-2: Electromechanically actuated extendable chord system kinematics in the retracted configuration.

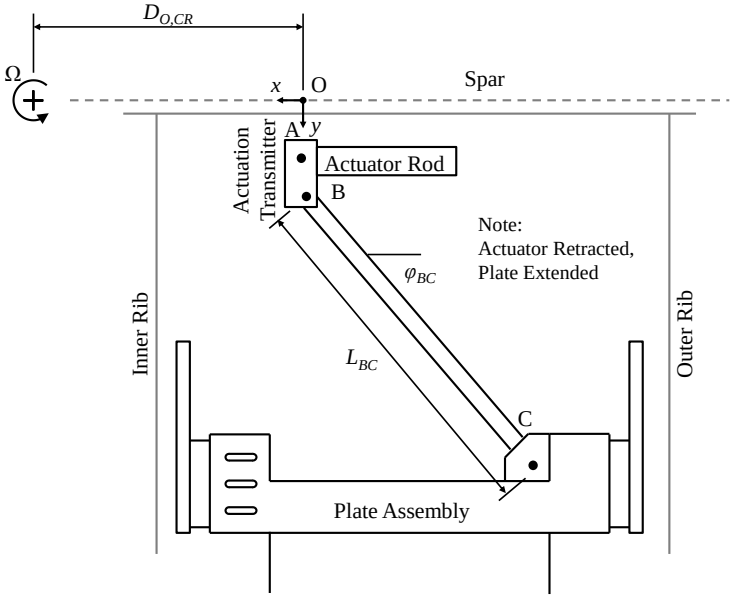

Figure 3-3: Electromechanically actuated extendable chord system kinematics in the extended configuration.

The origin, point O, is aligned chordwise with the center of rotation and corresponds to the point along the radius for which the actuator is fully retracted (i.e. plate extension). The kinematics of this system are simple and can be solved using Eqn. 1.

$$x_B - x_C\ ^2 + \ y_B - y_C\ ^2 = {L_{BC}}^2 \tag{1}$$

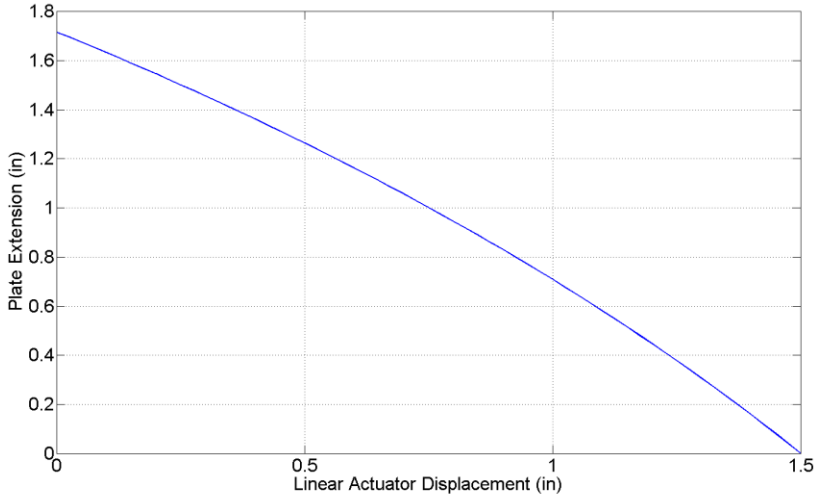

Figure 3-4: Initial design plate extension.

Figure 3-4 shows the amount of flat plate extension as a function of the actuator stroke. Obviously, when the actuator is fully deployed, the plate is fully retracted (and vice versa). The maximum stroke achieved by this system is 1.717 in which corresponds to a 10.7% increase in chord, meeting the minimum requirements set forth.

The force and moment analysis can be broken up into four major components: actuation transmitter and moving EMA rod, linkage, plate assembly, and inner slide component. While the first three are rather self explanatory, the inner slide may not be immediately obvious. This component constitutes the sliding element on the inner rib as well as the corresponding hinge.

These components are attached to the plate assembly via slots and therefore only the chordwise forces contribute to the overall system and not the spanwise forces or moments (Figure 3-5).

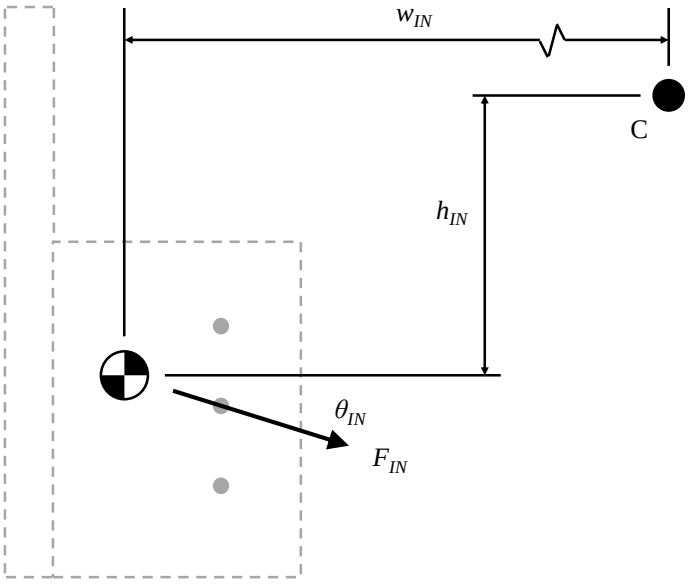

Figure 3-5: Applied forces due to inner rib slide and hinge.

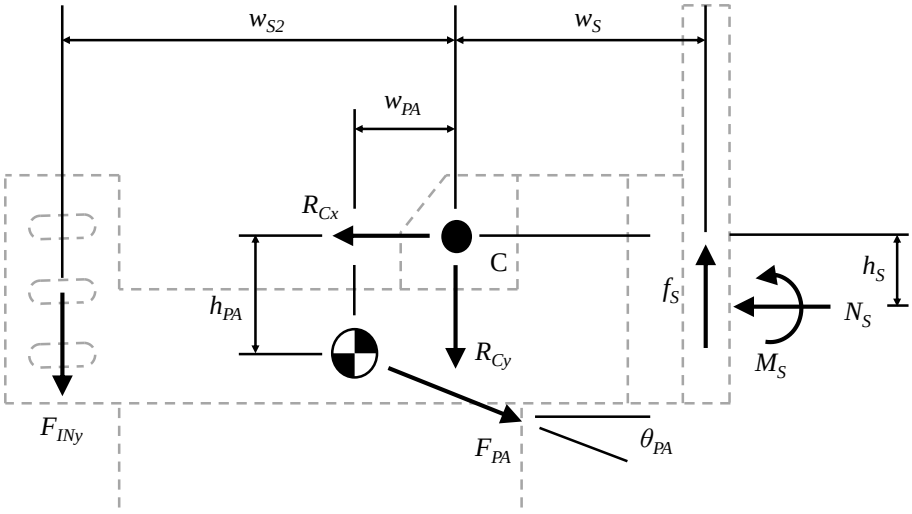

Figure 3-6: Force and moment diagram of plate assembly.

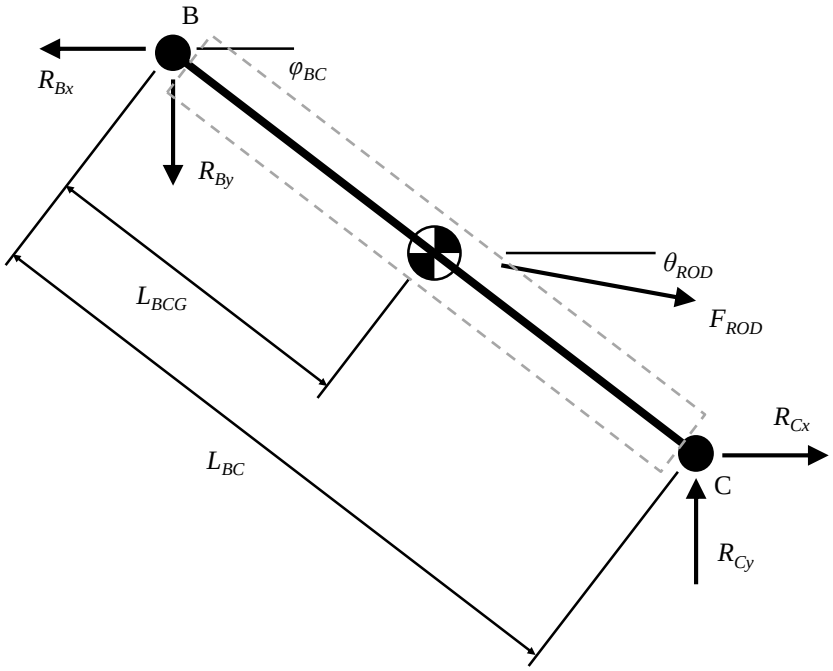

Figure 3-7: Force and moment diagram of the linkage.

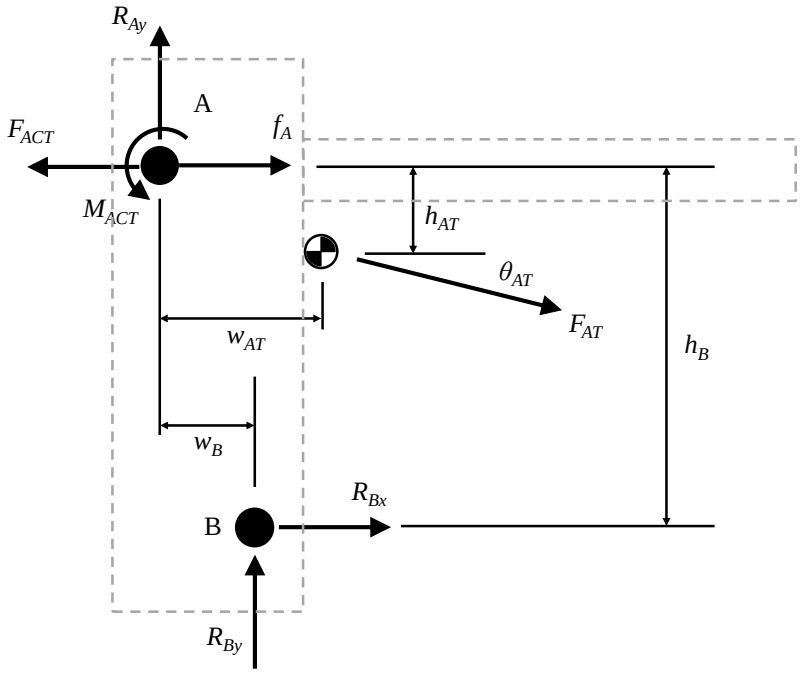

Figure 3-8: Force and moment diagram of actuation transmitter and EMA rod.

The free body diagrams shown in the previous figures were then used to generate a system of equations to solve for the internal and external loads.

From Figure 3-6:

$$F_x = R_{Cx} + N_S - F_{PA}\cos\theta_{PA} = 0 \tag{2}$$

$$F_y = R_{Cy} + f_S + F_{PA}\sin\theta_{PA} + F_{IN}\sin\theta_{IN} = 0 \tag{3}$$

$$\begin{aligned} M_Z = M_S + F_{PA}\sin\theta_{PA} w_{PA} + F_{PA}\cos\theta_{PA}\, h_{PA} - f_S w_S \\ - N_S h_S + F_{IN}\sin\theta_{IN} w_{S2} = 0 \end{aligned} \tag{4}$$

From Figure 3-7:

$$F_x = R_{Bx} - R_{Cx} - F_{ROD}\cos\theta_{ROD} = 0 \tag{5}$$

$$F_y = R_{By} - R_{Cy} + F_{ROD}\cos\theta_{ROD} = 0 \tag{6}$$

$$\begin{aligned} M_Z = {} & R_{Cx} l_{BC}\sin\theta_{BC} + R_{Cy} l_{BC}\cos\theta_{BC} \\ & + F_{ROD}\cos\theta_{ROD} l_{BCG}\sin\varphi_{BC} \\ & - F_{ROD}\sin\theta_{ROD} l_{BCG}\cos\varphi_{BC} = 0 \end{aligned} \tag{7}$$

From Figure 3-8:

$$F_x = F_{ACT} - f_A - R_{Bx} - F_{AT}\cos\theta_{AT} = 0 \tag{8}$$

$$F_y = -R_{Ay} - R_{By} + F_{AT}\sin\theta_{AT} = 0 \tag{9}$$

$$\begin{aligned} M_z = {} & M_{ACT} + R_{By} w_B + R_{Bx} h_B \\ & + F_{AT}\cos\theta_{AT} h_{AT} - F_{AT}\sin\theta_{AT} w_{AT} = 0 \end{aligned} \tag{10}$$

Eqn. 11 combines these equations into a 9 x 9 matrix of equations where the right-hand-side of the system represents the applied loads. Notice that the applied loads arise entirely due to rotation of the system. Although friction has been included in this model, it is implemented based on a linear coefficient of friction for which the normal forces do not appear in a stationary system. While an inherent amount of friction will exist on the benchtop, this should be much less significant than the friction that develops under the centrifugal loading. Thus, the model should be able to determine approximate values for design purposes. The force and moment calculations presented here assumed a 500 RPM limit.

$$A\ x = b \tag{11}$$

where

$$A = \begin{bmatrix} 1 & -\mu_{Al,Al} & 0 & -1 & 0 & 0 & 0 & 0 & 0 \\ 0 & 1 & 0 & 0 & 1 & 0 & 0 & 0 & 0 \\ 0 & 0 & 1 & h_B & w_B & 0 & 0 & 0 & 0 \\ 0 & 0 & 0 & 1 & 0 & -1 & 0 & 0 & 0 \\ 0 & 0 & 0 & 0 & 1 & 0 & -1 & 0 & 0 \\ 0 & 0 & 0 & 0 & 0 & L_{BC}sin\theta_{BC} & L_{BC}sin\theta_{BC} & 0 & 0 \\ 0 & 0 & 0 & 0 & 0 & 1 & 0 & 1 & 0 \\ 0 & 0 & 0 & 0 & 0 & 0 & 1 & \mu_S & 0 \\ 0 & 0 & 0 & 0 & 0 & 0 & 0 & h_s + \mu_S w_s & -1 \end{bmatrix},$$

$$x = \begin{matrix} F_{ACT} \\ R_{Ay} \\ M_{ACT} \\ R_{Bx} \\ R_{By} \\ R_{Cx} \\ R_{Cy} \\ N_S \\ M_S \end{matrix} \quad , and\ b = \Omega^2 \quad \begin{matrix} M_{AT}R_{AT}\cos\theta_{AT} \\ M_{AT}R_{AT}\sin\theta_{AT} \\ M_{AT}R_{AT}\ w_{AT}\sin\theta_{AT} - h_{AT}\cos\theta_{AT} \\ M_{ROD}R_{ROD}\cos\theta_{ROD} \\ -M_{ROD}R_{ROD}\sin\theta_{ROD} \\ M_{ROD}R_{ROD}L_{BCG}\ \sin\theta_{ROD}\cos\theta_{BC} - \cos\theta_{ROD}\sin\theta_{BC} \\ M_{PA}R_{PA}\cos\theta_{PA} \\ -M_{PA}R_{PA}\sin\theta_{PA} \\ M_{PA}R_{PA}\ w_{PA}\sin\theta_{PA} + h_{PA}\cos\theta_{PA}\ + F_{IN}\sin\theta_{IN}\ /\Omega^2 \end{matrix},$$

Of particular interest are the actuator, linear slide, and linkage loads. The geometry and mass properties from the SolidWorks model have been implemented into the system of equations

to obtain the following results. As a minor note, these figures have been produced assuming the extendable chord system is retracting. This was done because the direction of the mechanism only affects the friction forces which act to increase the actuation force during retraction and decrease the actuation force in extension. Therefore, the highest actuation requirements occur during retraction of the plate.

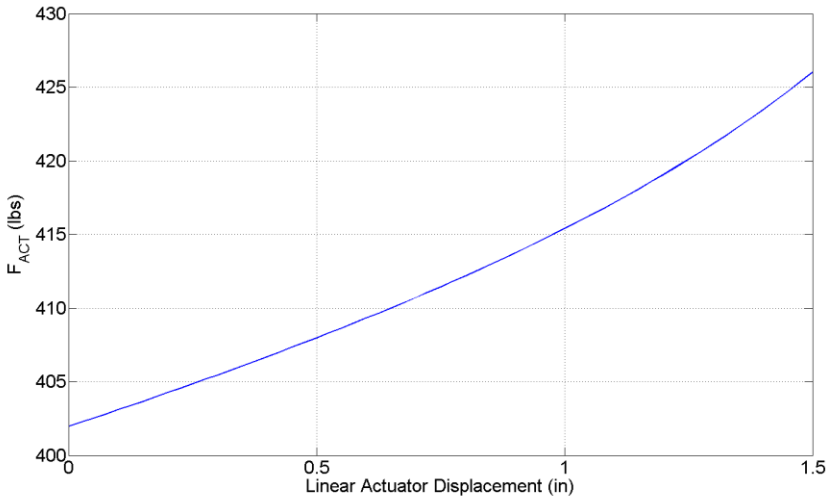

Figure 3-9: Initial design actuation force requirements during plate retraction at 500 RPM.

As shown, the maximum required force of the electromechanical actuator is 426 lbs. Using this value as the minimum force output, it was possible to select a more suitable electromechanical actuator. The linear actuator selected for the centrifugal test was manufactured by Ultra Motion, the specifications for which are listed in Table 3-1.

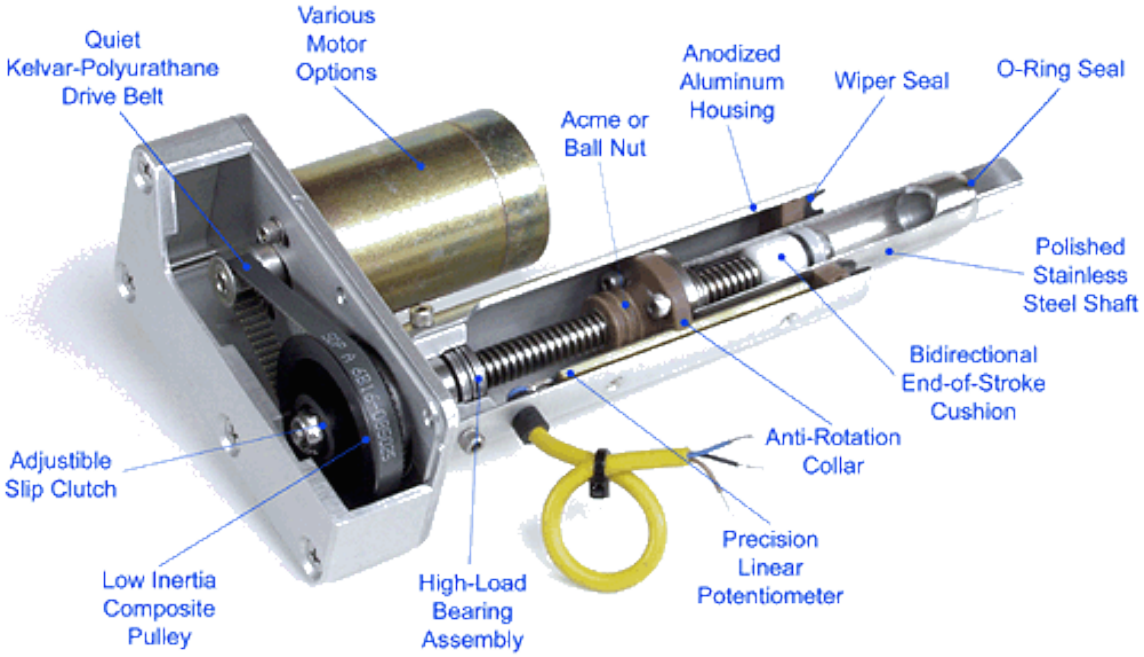

Figure 3-10: Ultra Motion Bug linear actuator (Ref. 18).

Table 3-1: Ultra Motion Bug linear actuator properties (Ref. 18).

Property	**Unit**	**Value**
Part Number		3-A.25-DCG94_65-2-P-RC4/RC4
Stroke	in	2
Max Force	lbs	500
Max Speed	in/sec	0.12
No-load Current	A	0.10
Stall Current	A	2.90
Weight	lbs	2.08

This model was chosen due to its 500lbs force output as well as its relatively fast actuation speed when compared to other EMAs with similar force capabilities. One of the most important elements of this motor was its size. Given the NACA 0015 airfoil with a 16 in chord for the test section, the maximum thickness at the quarter-chord is 2.4 in. Fortunately, this actuator is enclosed in a 2 x 4 in envelope which just barely fit inside the airfoil profile.

The force and moment analysis also demonstrated the need for high strength linear slides along the rails. The drawer slides, similar to those used in the benchtop model, can support a

maximum normal load of 112 lbs (moment limits are unknown). However, as seen in Figure 3-11 and Figure 3-12, the maximum normal force and moment seen by the outer rib linear slide is 373.8 lbs and 19.9 lb-ft, respectively, which far exceed the capabilities of a typical drawer slide.

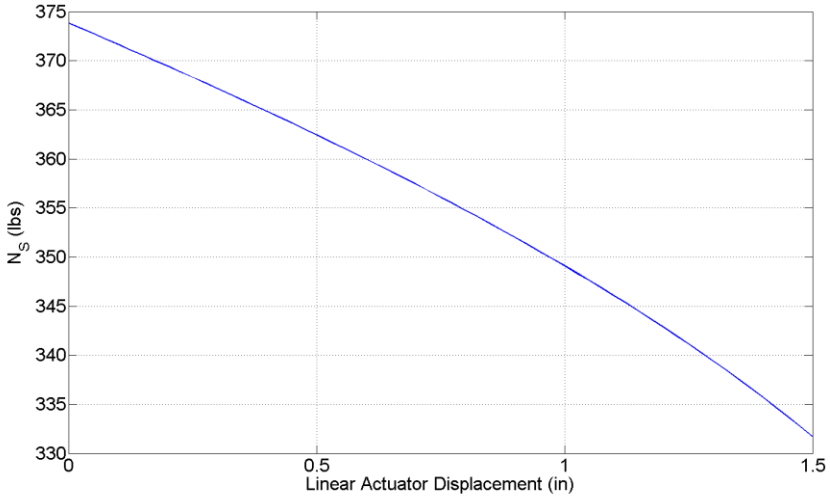

Figure 3-11: Initial design linear slide normal force during plate retraction at 500 RPM.

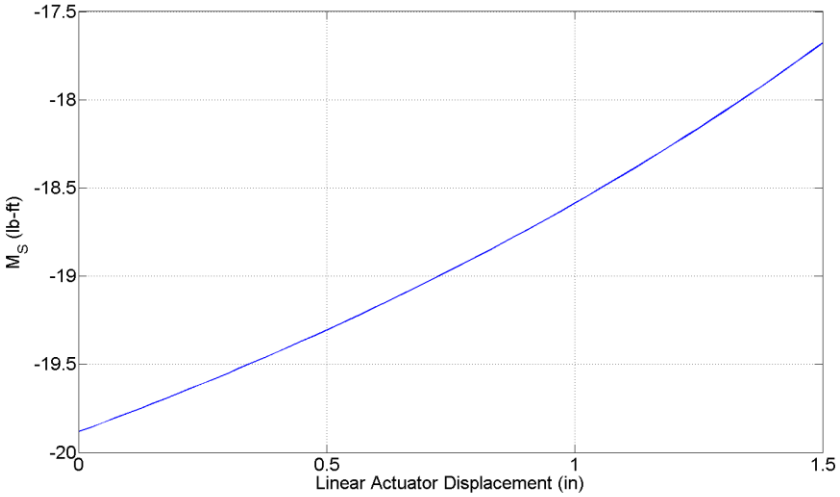

Figure 3-12: Initial design linear slide moment during plate retraction at 500 RPM.

Therefore, it was necessary to acquire an improved linear motion slide. The LH15AN linear guide provided by NSK Americas demonstrates the ability to support a dynamic normal force up to 2,428 lbs and a static moment of 2,243 lb-ft (Ref. 19). Obviously the structural limits of this slide are well above any force seen in the extendable chord system. The issue with this component is then the increased geometric profile shown in Figure 3-13. However, with careful design this can easily be resolved.

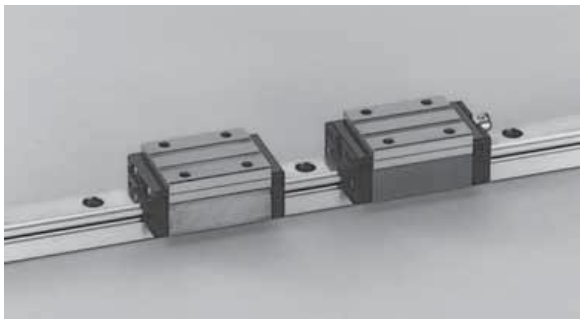

Figure 3-13: LH15AN linear guide (Ref. 19)

The final, load-supporting element in the extendable chord system is the linkage. Using the force and moment analysis for the linkage shown in Figure 3-7**Error! Reference source not found.**, the maximum estimated axial force in the linkage was calculated to be 139 lbs. Using Eqns. 12-14, and assuming 40 ksi yield strength for Al 6061, the linkage should have a diameter of no less than 0.07 in. Obviously, given such a low axial load, failure of the linkage in tension should not be an issue.

$$\sigma = \frac{F}{A} \tag{12}$$

$$A = \frac{1}{4}\pi D^2 \tag{13}$$

$$D_{min} = 2 * \sqrt{\frac{F}{\pi \sigma_{yield}}} \tag{14}$$

This first design iteration also demonstrated the difficulties in measuring the force requirements of the extendable chord system. While it would be desirable to place a load cell directly on the end of the electromechanical actuator, this is unfeasible due to the limited spanwise dimension. Therefore, the load cell must be placed elsewhere, such as on the linkage, in order to get a measurement of the actuation force. In this configuration, the load cell must have a limit load well over the 139 lbs estimated in the first iteration design.

3.2.2 Measurements and Sensors

It was then necessary to determine what measurements would be taken during the spin tests. First, it was desirable to have a direct measurement of the actuator output force. This was to be done using an axial load cell mounted at the end of the actuator. The load cell used in the final prototype, shown in Figure 3-14, has a 300 lbs load limit which is less than the anticipated actuation force. The reason for this will be described in the next section.

Figure 3-14: LC202-300 load cell (Ref. 20).

Due to the fact that the electromechanical actuator has a built in potentiometer and that the relationship between actuator displacement and plate extension is clearly defined, it was not necessary to have a direct measurement of the plate position. However, it was still desirable to

include a potentiometer on the plate assembly as a redundant measurement system. Rather than using a standard linear potentiometer which uses a metal tab to attach to the point of measurement, this system incorporates a touch based membrane potentiometer. The SoftPot, manufactured by Spectra Symbol, uses a wiper mounted to the plate assembly which presses down on the potentiometer to measure the plate extension (Ref. 21).

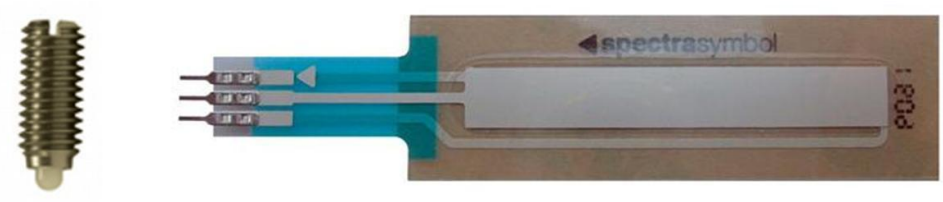

Figure 3-15: SoftPot membrane potentiometer (Ref. 21).

Each of these sensors was connected to a cable running through the conduit tube through the inner blade structure and connected to a wireless transmitter mounted on the rotor hub. For this study, the MicroStrain V-Link –mXRS Wireless Voltage Node was then used to transmit the information from the rotating frame to the fixed frame (Figure 3-16).

Figure 3-16: V-Link® -mXRS™ wireless transmitter (Ref. 22).

This wireless transmitter featured an onboard 3V sensor excitation which eliminated the need to power the sensors externally. Moreover, the transmitter featured four full differential channels, one of which was used by the load cell, and three single ended inputs, used by the potentiometers.

Finally, the power required to actuate the mechanism was to be determined by recording the average current supplied by the power source located within the control room.

3.3 Updated Electromechanically Actuated Prototype

After many design iterations, the updated prototype for the centrifugal test of an extendable chord structure using an electromechanical actuation system was developed (Figure 3-17). As shown in the figure, except for a few minor adjustments, the actuation method is largely similar.

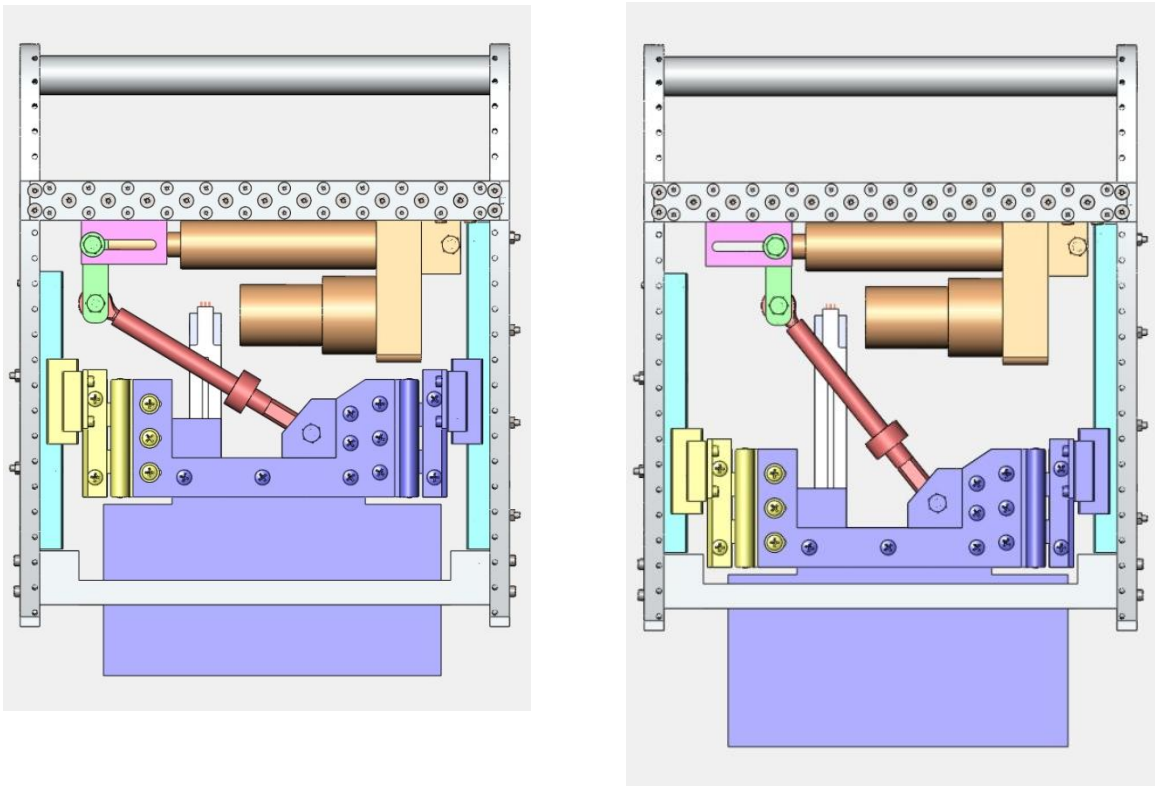

(a) (b)

Figure 3-17: CAD model of electromechanically actuated extendable chord system in the (a) retracted and (b) extended configurations.

First of all, the Ultra Motion Bug linear actuator, shown in orange, is secured to the spar via a mounting block, shown in light red. The actuation rod is then pinned to the (green) actuation transmitter. The pin connecting these elements is restricted to move in the spanwise direction by the (pink) guide rail. The spanwise displacement is then then converted into chordwise extension by the (red) linkage. Although the initial intention of the load cell was to directly measure the actuator force, this was not possible due to the limited spanwise dimension of the test section. Rather, the load cell has been placed along the linkage as shown. The output could then be used to validate the numerical analysis. The plate assembly, shown in purple, again is used to clamp the flat plate, made of aluminum honeycomb to reduce weight, and the rotation hinges required by the blade twist kinematics. The inner rib linear slide, shown in yellow, is

connected to the rest of the plate assembly using extensible slots with screws which allow spanwise motion while restricting chordwise displacement.

While the actuation mechanism has been relatively unchanged, there are a few significant structural changes from the initial design. For example, a leading edge mass has been included in order to move the section center of mass forward for improved stability. This was implemented in the design using an Al 6061 rod with a 1 in diameter. Another major change between the initial design and the final design is the increase in the rib thickness of both the outer and inner ribs from 0.25 in to 0.50 in. The reason for this change will be described in subsequent sections. Additionally, one other change in the design is the trailing edge support. Initial thought was that rather than deploying a full size honeycomb plate through the trailing edge, an equivalently weighted steel plate would be that would not extend past the trailing edge even when fully deployed. This was considered to minimize the difference in loading between the blade with the extended chord and the counter balance blade. The test section would then be able to use the existing, closed-section, triangular trailing edge support. However, it was determined that by running the rotor at a 0° collective pitch, this imbalance would be minimal and should not affect the test. Therefore, the initial triangular trailing edge, which would not allow for an extended chord, had to be replaced by a trailing edge support with a rectangular slot through which the plate may extend. This would allow visual confirmation of plate extension using the cameras mounted in the AERTS facility.

3.4 Revised Force and Moment Analysis

A new force and moment analysis was then conducted based upon the updated mass and geometry. Since only the dimensions of the design had been modified, it was possible to use the

analysis presented earlier in this chapter. The results are shown in Figure 3-18 through Figure 3-21.

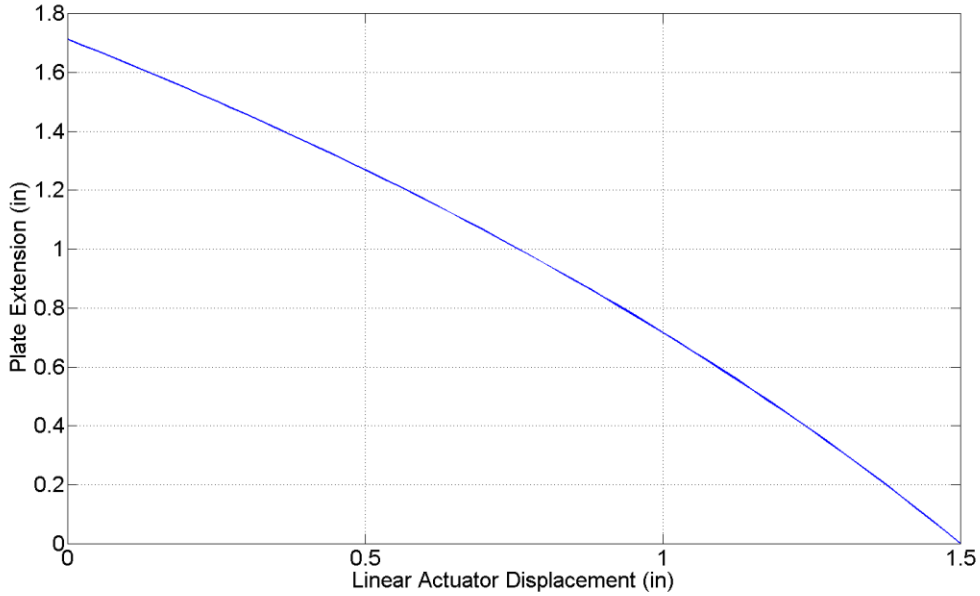

Figure 3-18: Plate extension of EMA extendable chord system.

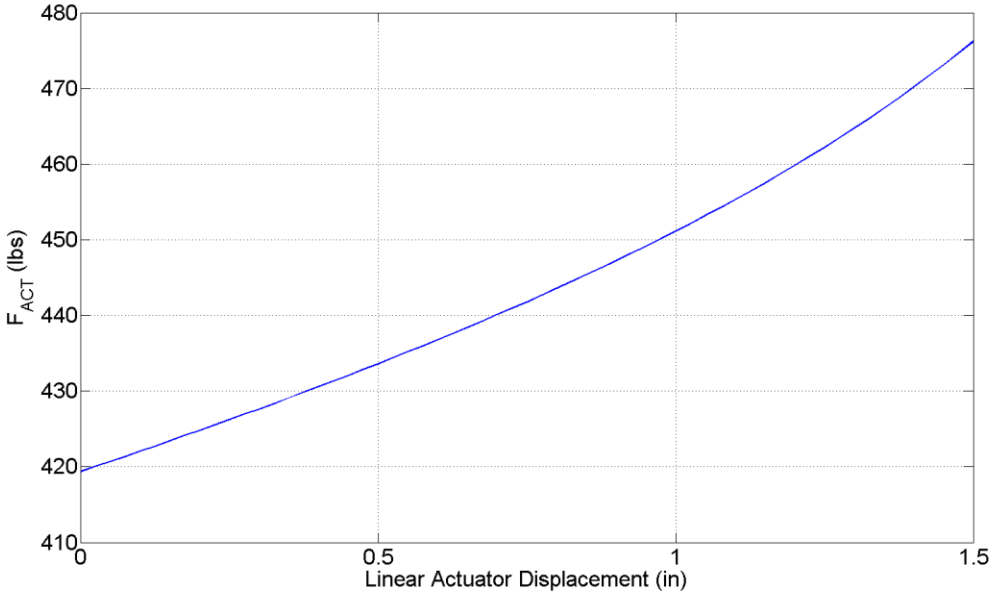

Figure 3-19: Actuation force requirements during plate retraction at 500 RPM.

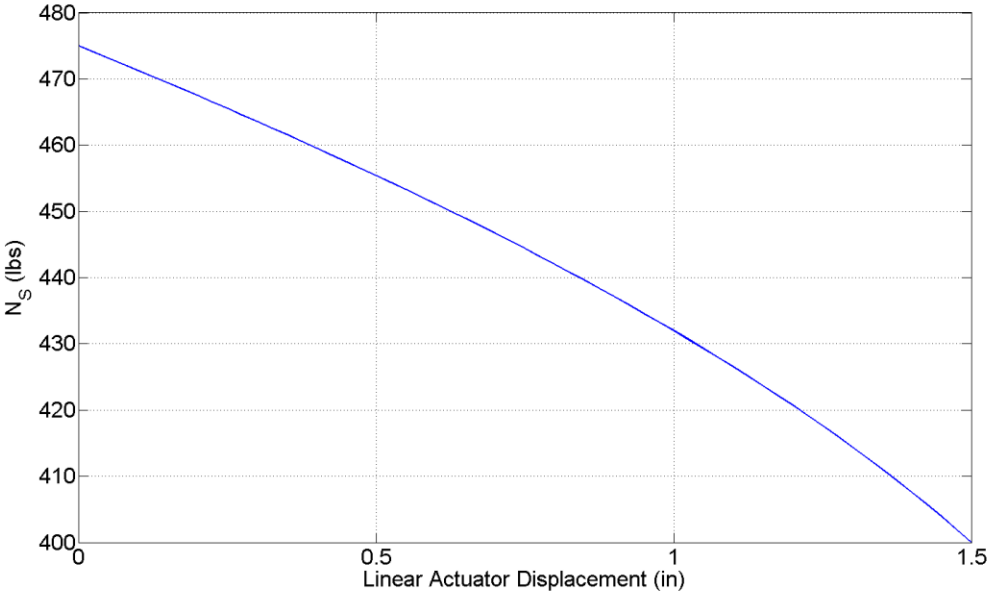

Figure 3-20: Outer rib linear slide normal force during plate retraction at 500 RPM

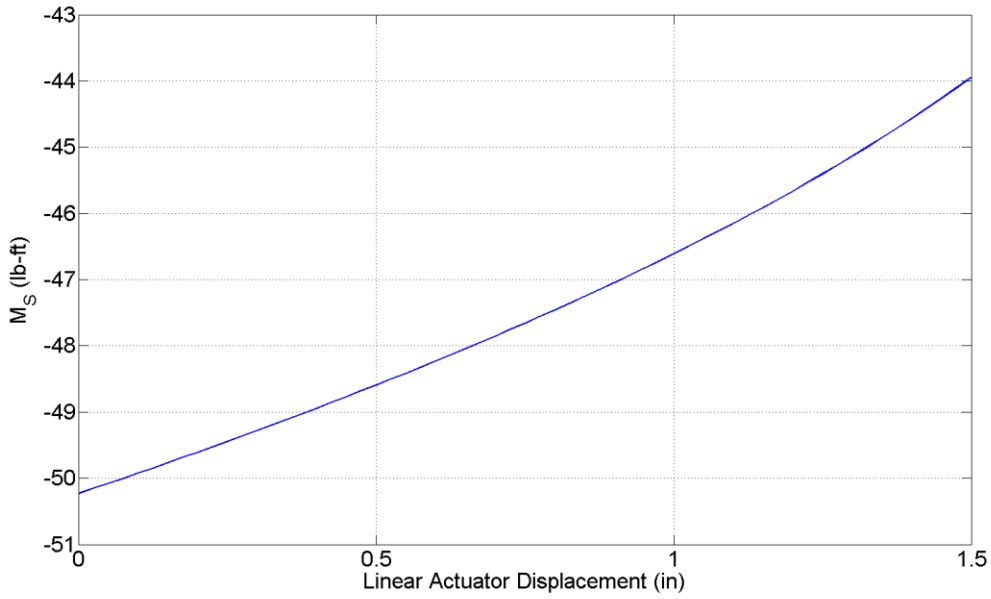

Figure 3-21: Outer rib linear slide moment during plate retraction at 500 RPM.

As shown, the maximum extension is 1.714 in which is very similar to the initial design. On the other hand, the actuation force requirement has now increased to a maximum of 476 lbs. While still within the 500 lbs maximum force output for this motor, this underscores the need for

a high force actuator with a small geometric profile. Furthermore, the load on the outer rib linear slide has also increased significantly; although still well within the design limits for this component.

Unlike the previous analysis which simply presented the maximum axial force in the plain linkage, this analysis also took into account the load cell. The force and moment diagram for the load cell is shown in Figure 3-22.

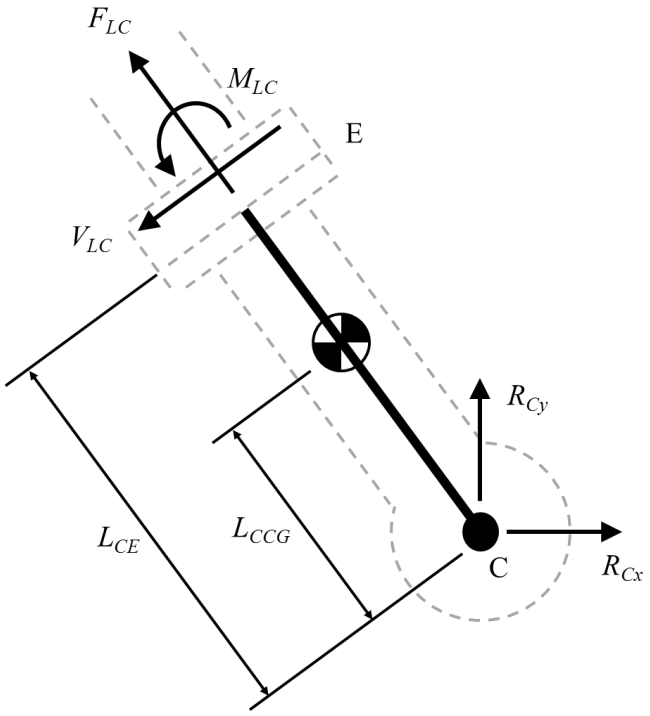

Figure 3-22: Load cell force and moment diagram.

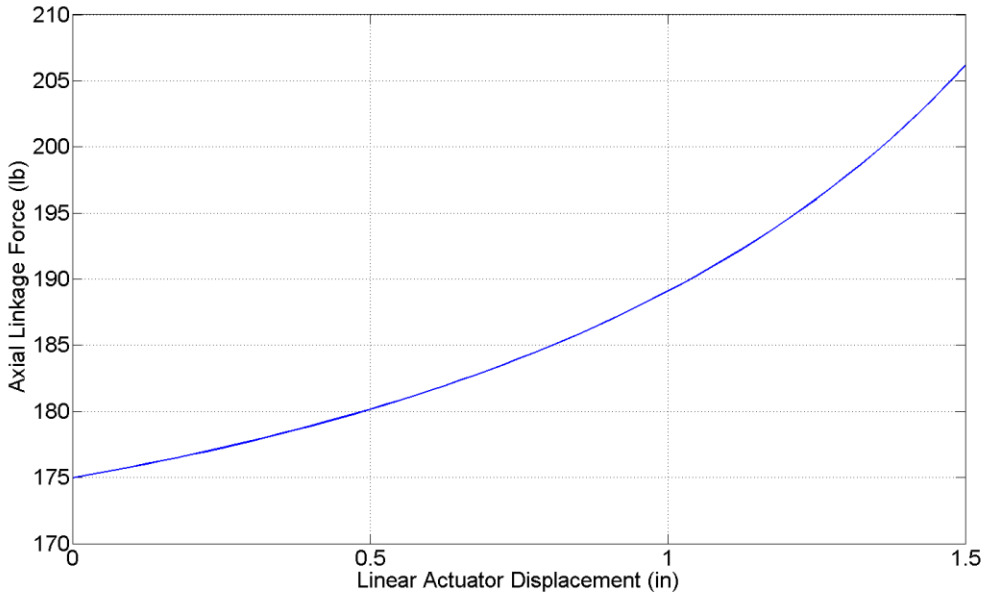

Figure 3-23: Axial linkage force during plate retraction at 500 RPM.

Given the location of the load cell, the measured force as a function of actuator displacement is shown in Figure 3-23. Although this force is higher than the initial estimation, the LC202-300 load cell was still shown to be sufficient.

3.5 Finite Element Analysis

3.5.1 Initial Structural Shell

A finite element analysis of the structural shell was conducted to ensure the safety of the system when in the rotating environment. This analysis was conducted using only the structural elements of the test section and not the extendable chord mechanism itself. Therefore, the model included the main spar, ribs, leading edge mass, and trailing edge piece. The finite element

analysis was conducted using ANSYS, version 13.0 (Ref. 23). Material properties for the model are shown in Table 3-2.

Table 3-2: Structural shell material properties.

Component	**Material**	**Young's Modulus (psi)**	**Yield Stength (psi)**	**Density (lb/in^3)**
Ribs	Al 6061	10×10^6	40×10^3	0.0975
Spar	Al 6061	10×10^6	40×10^3	0.0975
Linear Slide Rails	Steel	30.5×10^6	90×10^3	0.278
LE Mass	Brass	14.5×10^6	69.4×10^3	0.307
TE Piece	Al 6061	10×10^6	40×10^3	0.0975

The ribs were modeled using two-dimensional shell elements (SHELL181) while the spar, leading edge mass, and trailing edge piece were each modeled using beam elements (BEAM188). The appropriate cross sectional data has been implemented for each component.

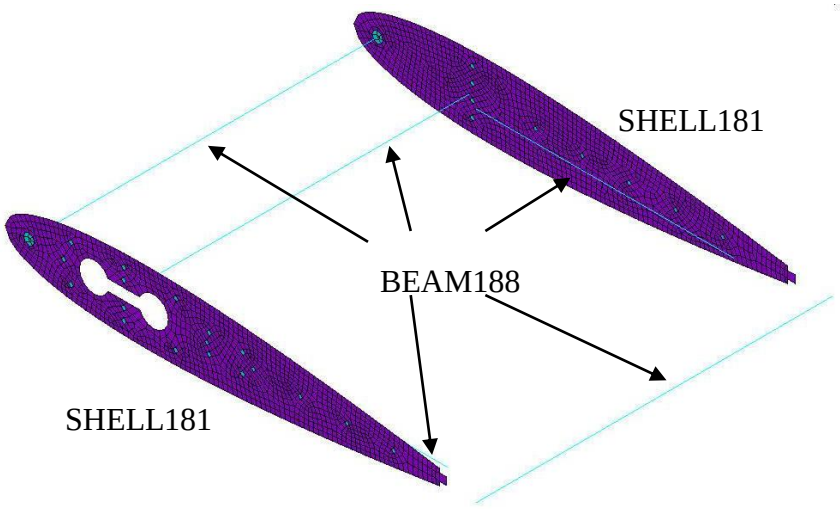

Figure 3-24: Finite element model of structural shell.

Figure 3-24 shows the test finite element model of the structural shell with the cross-sectional data displayed. It is important to remember that while this figure shows three-

dimensional elements, this is merely a representation of the cross-section and the actual elements still retain their original type (i.e. beam or shell).

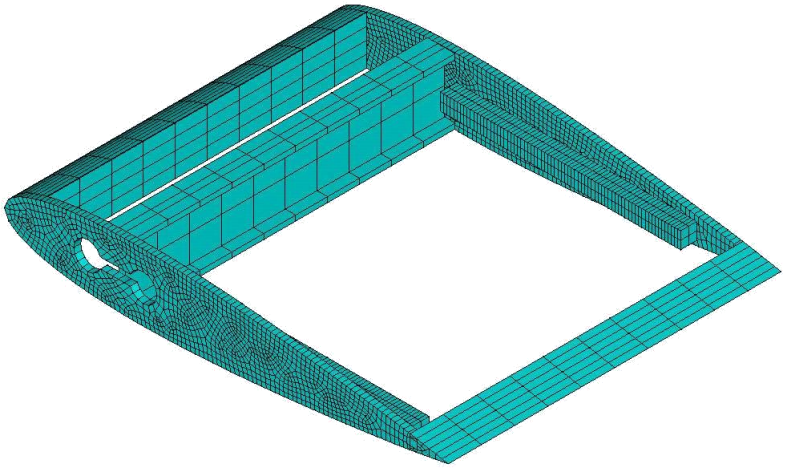

Figure 3-25: Finite element model of structural shell with cross-section data displayed.

As is evident, this model is based on a previous design iteration which included the thinner (0.25 in) ribs, a heavy brass nose piece cut to the contour of the leading edge, and the triangular trialing edge piece which did not allow for plate extension. The model has fixed boundary conditions where the test section connects to the inner blade structure. This occurs at the main mounting bolts as well as the adapter screws (Figure 3-26). Furthermore, the components have been connected to each other using coupled degrees of freedom at the appropriate screw locations.

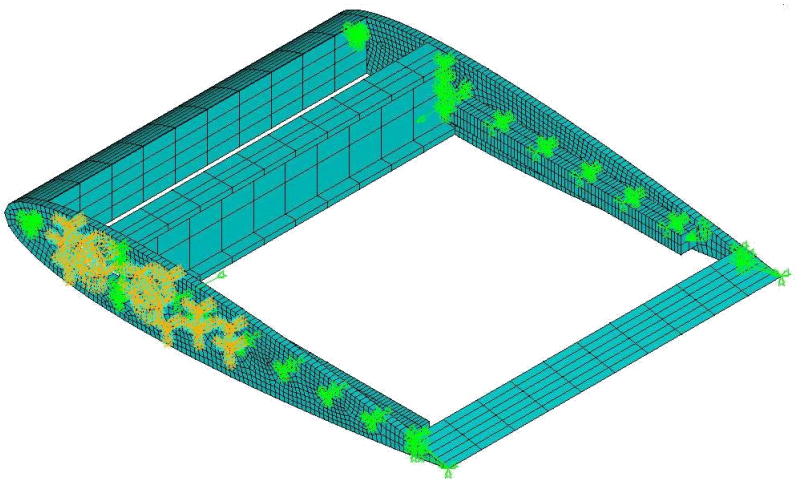

Figure 3-26: Boundary conditions of structural shell finite element analysis.

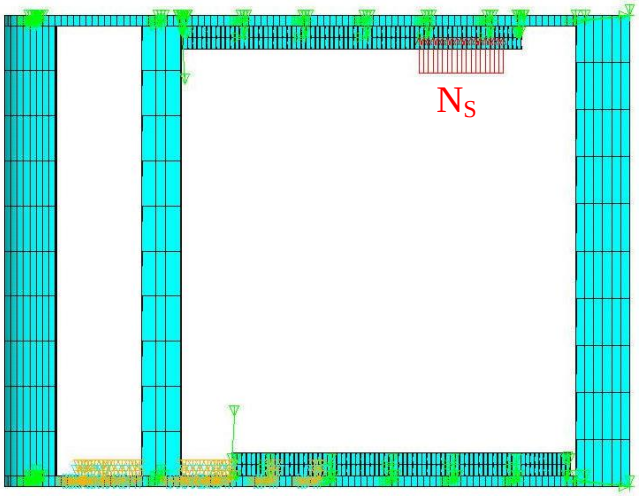

Figure 3-27: Applied loads on structural shell finite element analysis.

The applied loads have been calculated using the aforementioned force and moment analysis. However, for this model only the normal load was applied to the outer rib linear slide; it did not include the moment on the slide. Furthermore, this model did not include the spar guide rail restraining force or the loads transferred to the spar from the actuator. The applied force, N_S, was distributed evenly over the length of the carriage at the fully extended position. It is for this configuration that this force and its moment arm are the largest and will thus create the highest

stresses and displacements. Finally, the system has been subjected to centrifugal loading within ANSYS based on a rotational speed of 500 RPM.

The results of the static finite element analysis are shown in Figure 3-28 and Figure 3-29. Obviously the ribs have exceeded the 40 ksi yield strength, with the inner rib experiencing a maximum stress of 87.32 ksi at the leading edge.

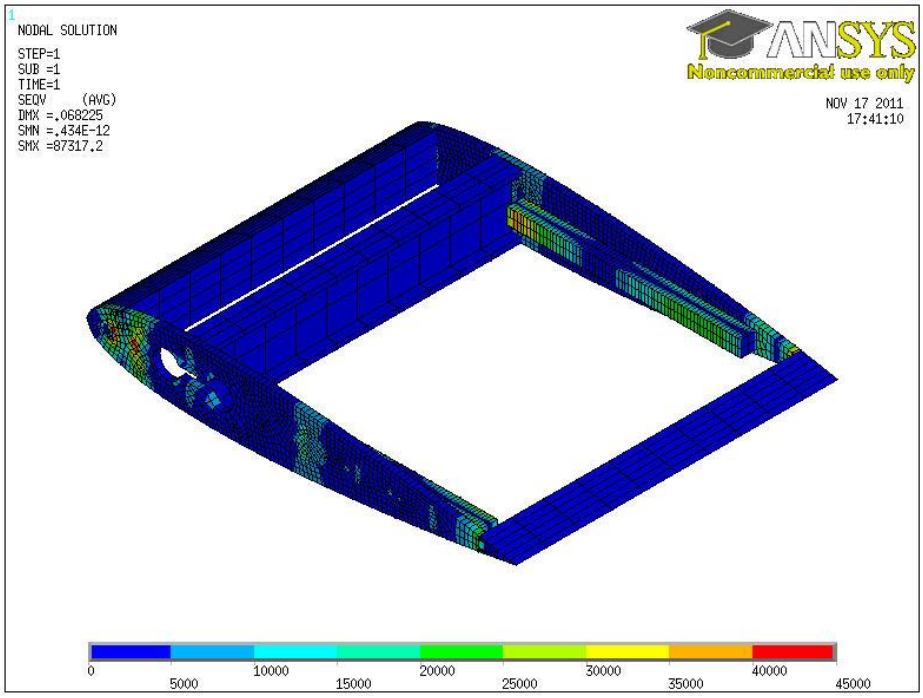

(a)

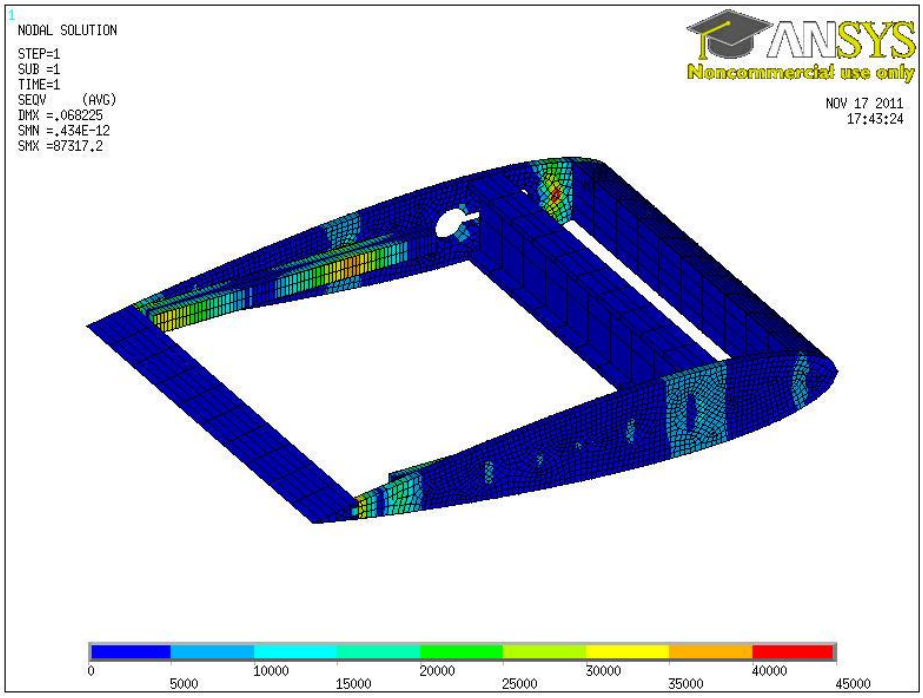

(b)

Figure 3-28: Von Mises stress distribution.

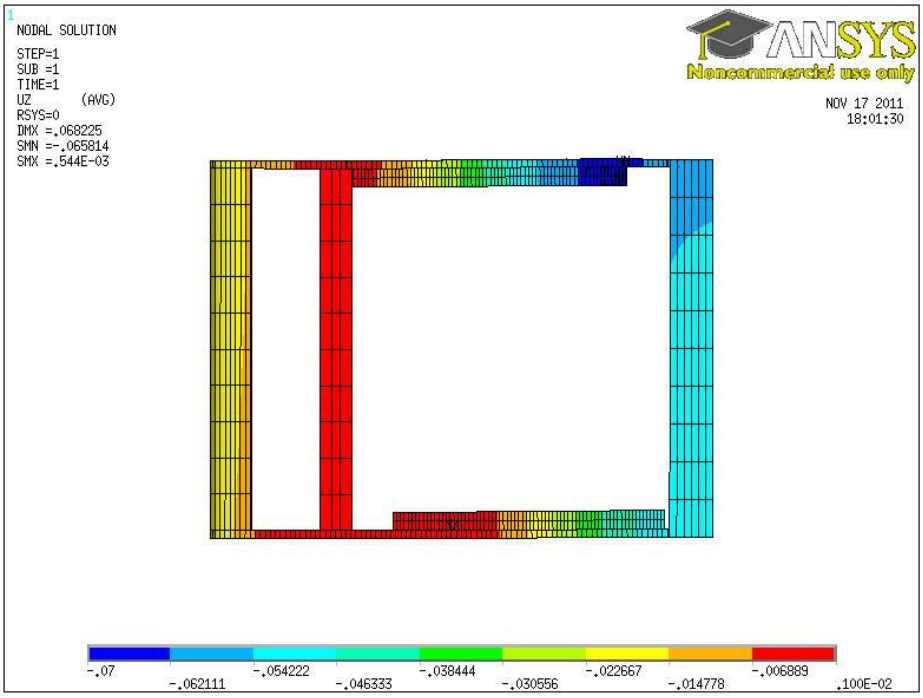

Figure 3-29: Displacement distribution.

Furthermore, due to the relatively low bending stiffness in the ribs, the displacement of the outer rib has a maximum value of 0.0658 in which may be significant enough to induce binding in the linear slides. Finally, by summing the reaction forces in the fixed or coupled degrees of freedom, it was possible to get an estimate of the loads in the screws. Figure 3-30 shows the critical screws with a factor of safety less than two. The limit loads for the screws and nuts have been calculated using the Machinery's Handbook (Ref. 24).

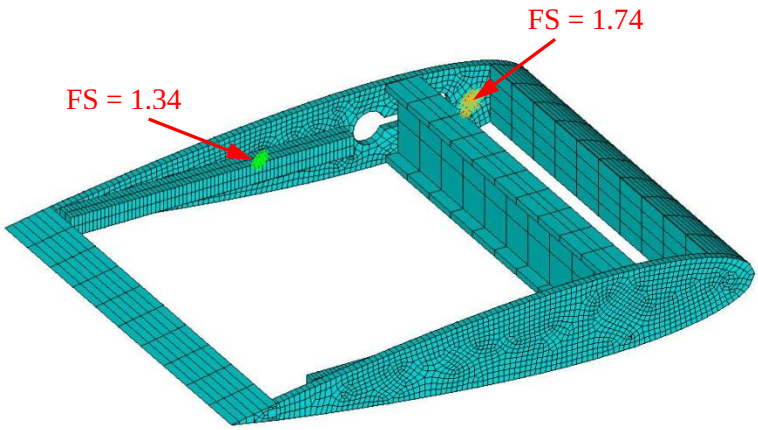

Figure 3-30: Critical connectors.

3.5.2 Modified Structural Shell

Obviously, the design must be modified to support the applied loads without failure. This was accomplished by doubling the thickness of the ribs from 0.25 in to 0.50 in which would provide a higher bending stiffness (Figure 3-31).

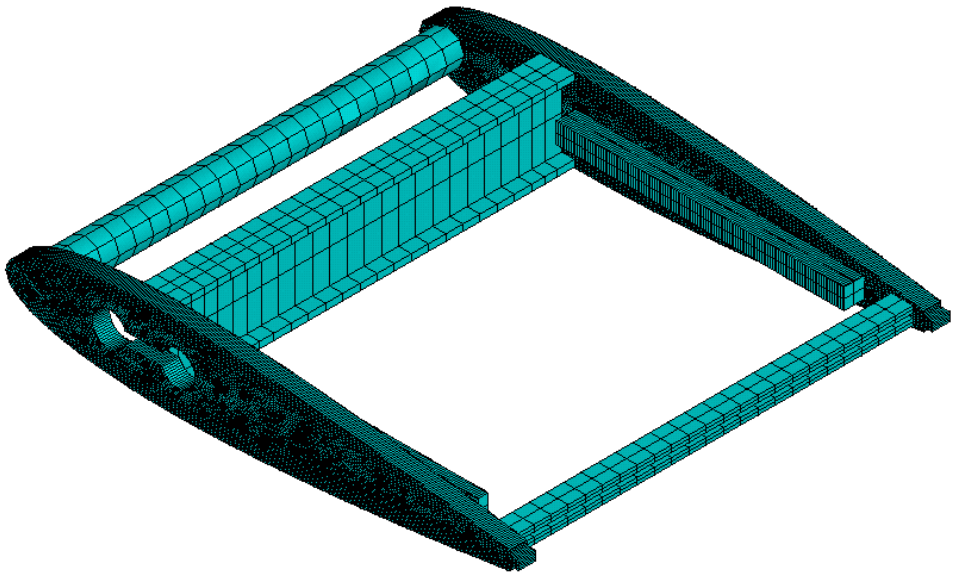

Figure 3-31: Modified structural shell finite element model.

Additionally, the heavy brass leading edge nose piece was replaced by the 1 in diameter Al 6061 rod seen in the final design. Although this moved the center of gravity further aft, it was deemed that the flutter would not be an issue given the high torsional rigidity of the inner blade structure. It was also at this point that the closed-section, triangular trailing edge was replaced by the slotted trailing edge support which allowed for the extendable chord to be physically realized. Furthermore, the loading condition model was improved to more accurately represent all of the loads present on the structural shell (Figure 3-32).

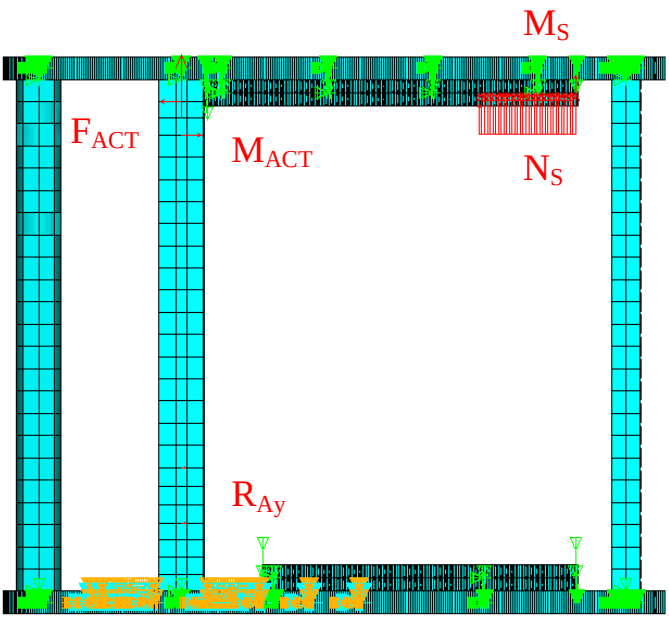

Figure 3-32: Modified structural shell applied loads.

By reducing the leading edge mass and increasing the rib thickness, it was possible to significantly reduce the stresses in the structure. Figure 3-33 shows the von Mises stress distribution for the final structural shell design. The maximum stress is now 22.0 ksi and occurs not at the leading edge but at the furthest point aft where the inner rib connects to the inner blade adapter. Note that the scale for the stress distribution has changed from the previous plot which

was set to show the areas where the structure has failed. This was done to show a better representation of the stress distribution throughout structure.

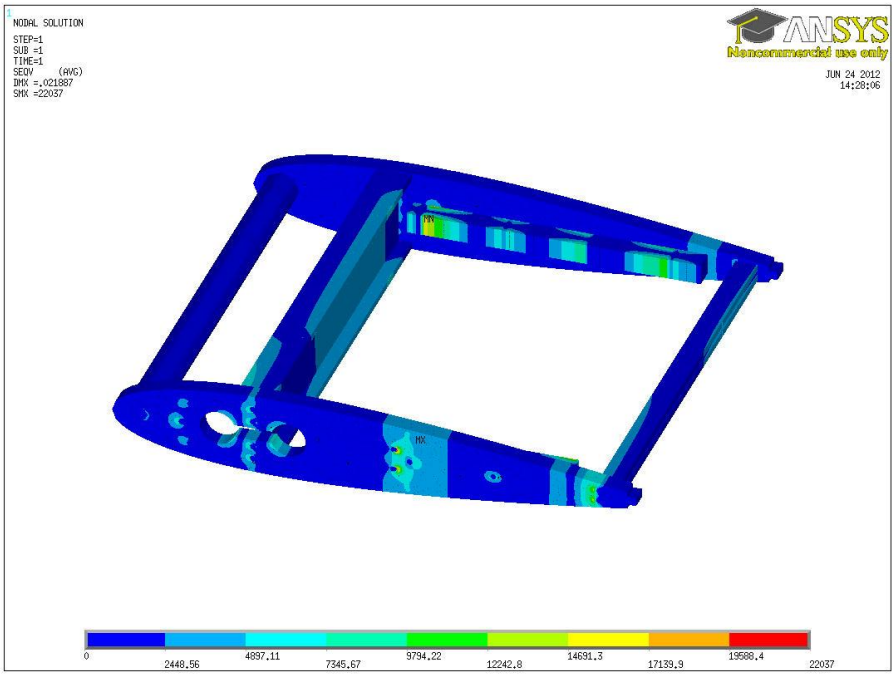

Figure 3-33: Von Mises stress distribution of modified structural shell.

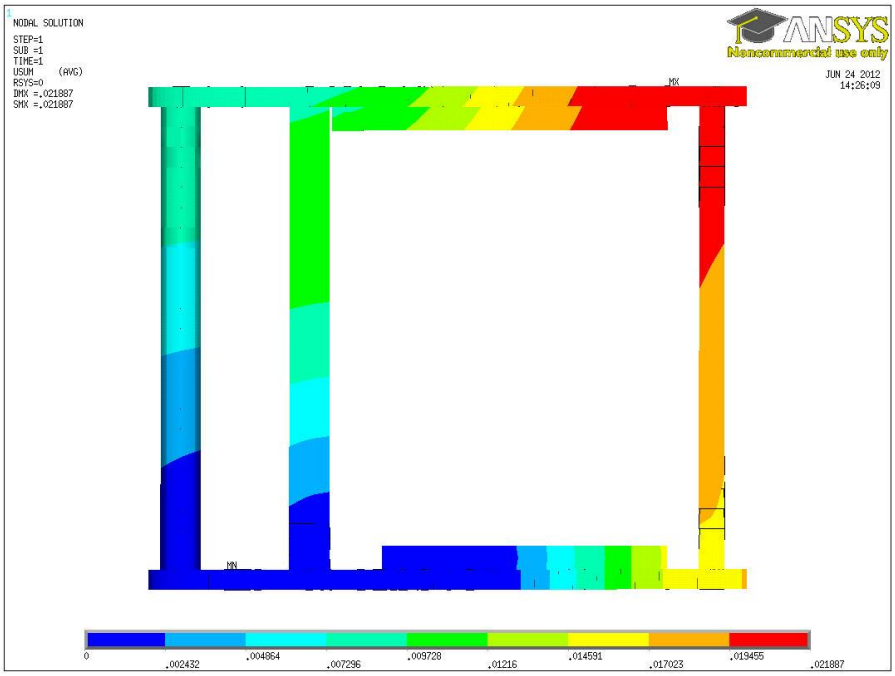

Figure 3-34: Displacement distribution of modified structural shell.

The displacement, shown in Figure 3-34, has also reduced significantly to a maximum of 0.022 in. However, it remains to be seen during the test if this is large enough to result in a binding of the system. Finally, the fixed and coupled boundary conditions must be investigated to determine if any of the screws have failed.

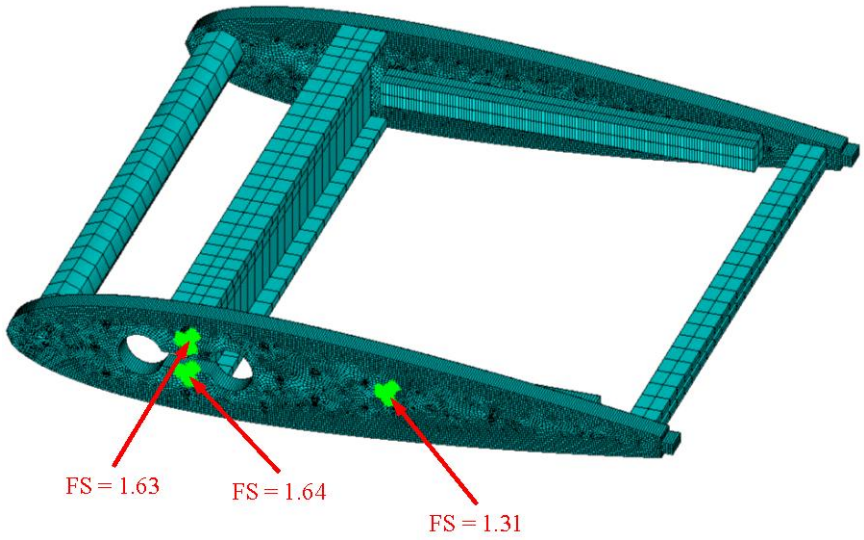

Figure 3-35: Critical connectors for modified structural shell.

While none of the connectors had failed, several of the connectors had a factor of safety slightly less than two (Figure 3-35). This included two of the four screws connecting the inner rib to the vertical spar web as well as the middle screw attaching the linear slide to the inner rib. It is important to note, however, that the screws connecting the top and bottom flanges to the inner and outer ribs have not been included. Clearly, this help relieve some of the load on the spar screws and therefore the low factor of safety in two of the screws was not a major concern. However, as a safety measure, the analysis was rerun removing the connections with a factor of safety less than two to ensure that even in the event of a failure at these locations, the entire

structure would still remain intact. The stress, displacement, and screw loads are very similar to the previous results and thus have not been presented here. Ultimately, the finite element analysis proved that with the current design, the structural shell system would not fail.

3.6 Counter Weight Fabrication

It was necessary to fabricate a dummy mass for the other blade in order to mitigate the large 1/rev loads on the hub due to the fact that the centrifugal test will incorporate only one extendable chord system. This dummy mass was to use the same 16 in chord, NACA 0015 airfoil shape with a 12 in span. Note that the final span for the test section is 12.5 in due to the increased rib thickness which has not been included on the dummy mass. Therefore, it will use the original 0.25 in thick ribs and the exact same spar design. Finally, the dummy mass will also be attached to a second inner blade structure in the same manner as the test section.

3.6.1 Test Section Center of Gravity

Before beginning the design of the counter weight, the center of gravity of the extendable chord test section must first be determined. The first generation prototype can be seen in Figure 3-36.

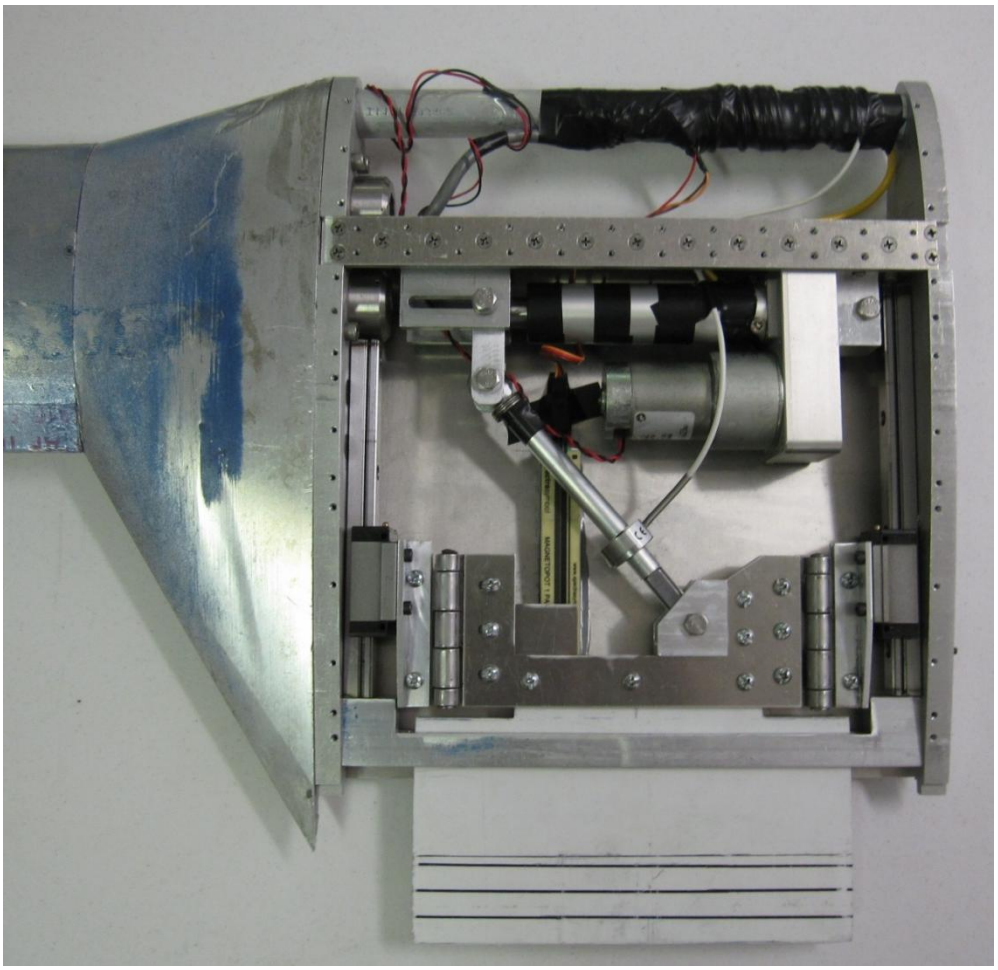

Figure 3-36: First generation electromechanically actuated prototype.

As the center of gravity of the test blade occurs nearly at the midplane through the thickness, only the two-dimensional center of gravity is of interest. This was calculated by measuring the weight at three distinct points independently using a scale. By ensuring that the test section was positioned in the same way every time, a single scale could be used in conjunction with two fixed points. This was accomplished by ensuring that the spar was always level (Figure 3-37).

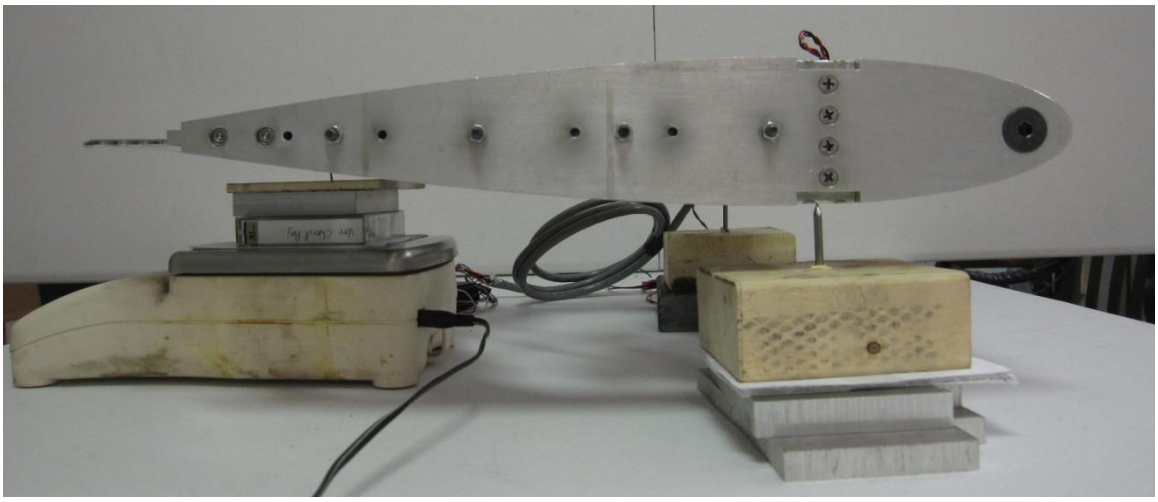

Figure 3-37: Three point center of gravity calculation.

With the location and weight at the three points known, a weighted average could be used to calculate the center of gravity for the test section via Eqns. 15 and 16 (Figure 3-38). Obviously as the system deploys, the center of gravity will move aft. Thus, this calculation was completed for both the fully retracted and fully extended configurations. The exact position of the test section center of gravity will be presented in the next section along with a comparison to the counter weight center of gravity.

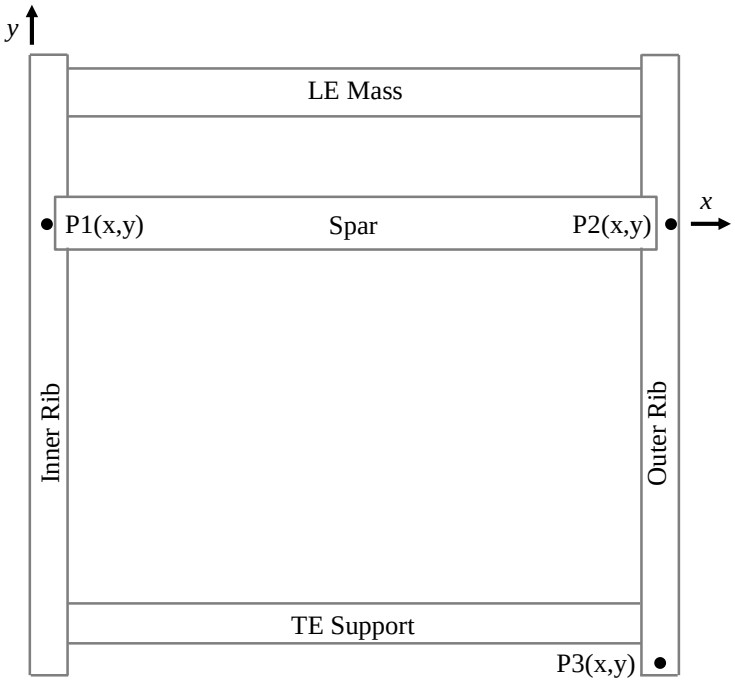

Figure 3-38: Center of gravity calculation sketch.

$$x_{CG} = \frac{\sum_{i=1}^{3} W_i x_i}{\sum_{i=1}^{3} W_i} \quad (15)$$

$$y_{CG} = \frac{\sum_{i=1}^{3} W_i y_i}{\sum_{i=1}^{3} W_i} \quad (16)$$

3.6.2 Counter Weight Design

The information gathered was then used to create a SolidWorks model of the counter balance section which approximated the center of gravity of the extendable chord structure (Figure 3-39).

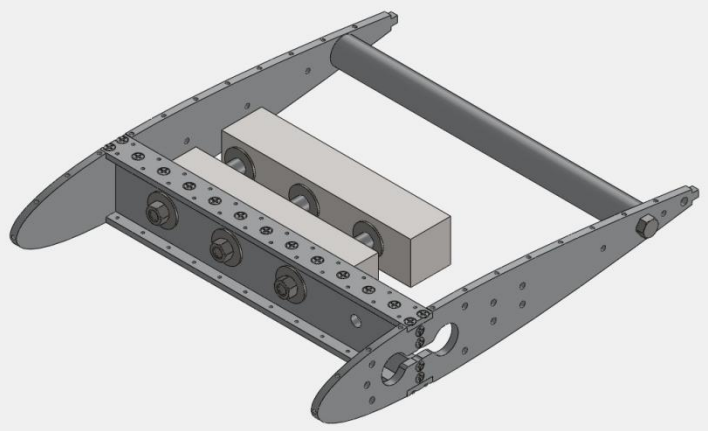

Figure 3-39: CAD model of counter balance.

As shown, the weight of the extendable chord mechanism has been replaced by two large steel blocks and an aluminum trailing edge rod. The steel blocks have been connected to the spar using three 3/8”-16 stainless steel hex bolts with aluminum spacers to set the correct chordwise position.

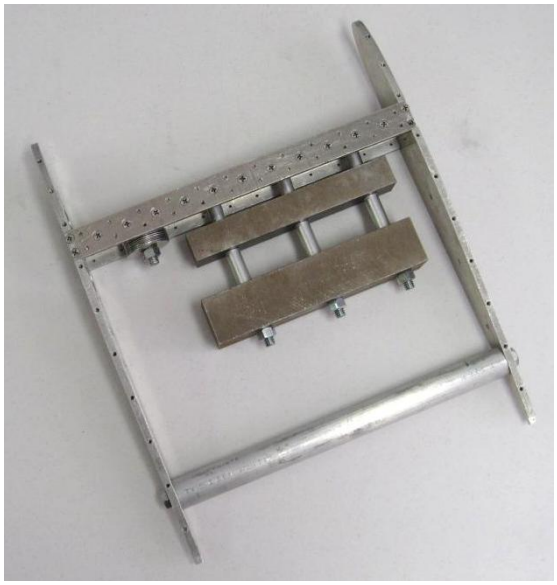

Figure 3-40: EMA prototype counter balance.

The final counter weight design is shown in Figure 3-40 which had to be slightly adjusted due to inaccuracies in the CAD model. This was easily accomplished using a small number of steel washers bolted to the spar.

The weight of the test section was calculated by summing the weight measured at all three points. In the retracted and extended configuration this value was found to be 196.20 oz and 196.35 oz, respectively. The reason for the discrepancy is due to minor inaccuracies which most likely resulted from the spar not being exactly level for every measurement. However, a difference of 0.15 oz is within acceptable tolerances. On the other hand, the counter weight has a total weight of 196.40 oz; a difference of 0.20 oz, or 0.10% (as compared to the retracted state measurement). This result combined with the fact that the location of the center of gravity is within 0.16 in (for both cases) provided sufficient evidence that the test section blade and dummy blade would be properly balanced during the centrifugal test.

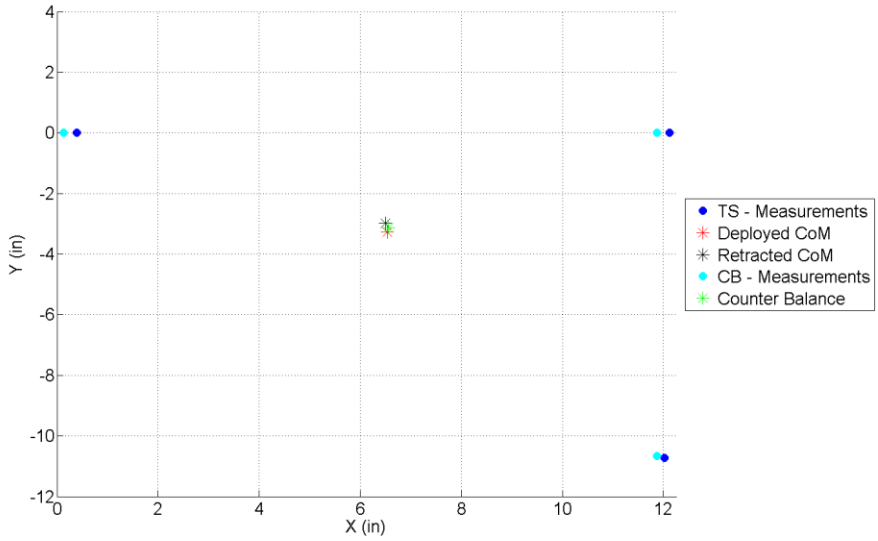

Figure 3-41: Center of gravity comparison.

3.7 Initial Rotor Tests

The following sections detail the results of the initial centrifugal tests of the extendable chord system. As previously mentioned, these tests were conducted on the Penn State Adverse Environment Rotor Test Stand. Figure 3-42 shows this facility with the extendable chord and counter weight blades installed on the rotor.

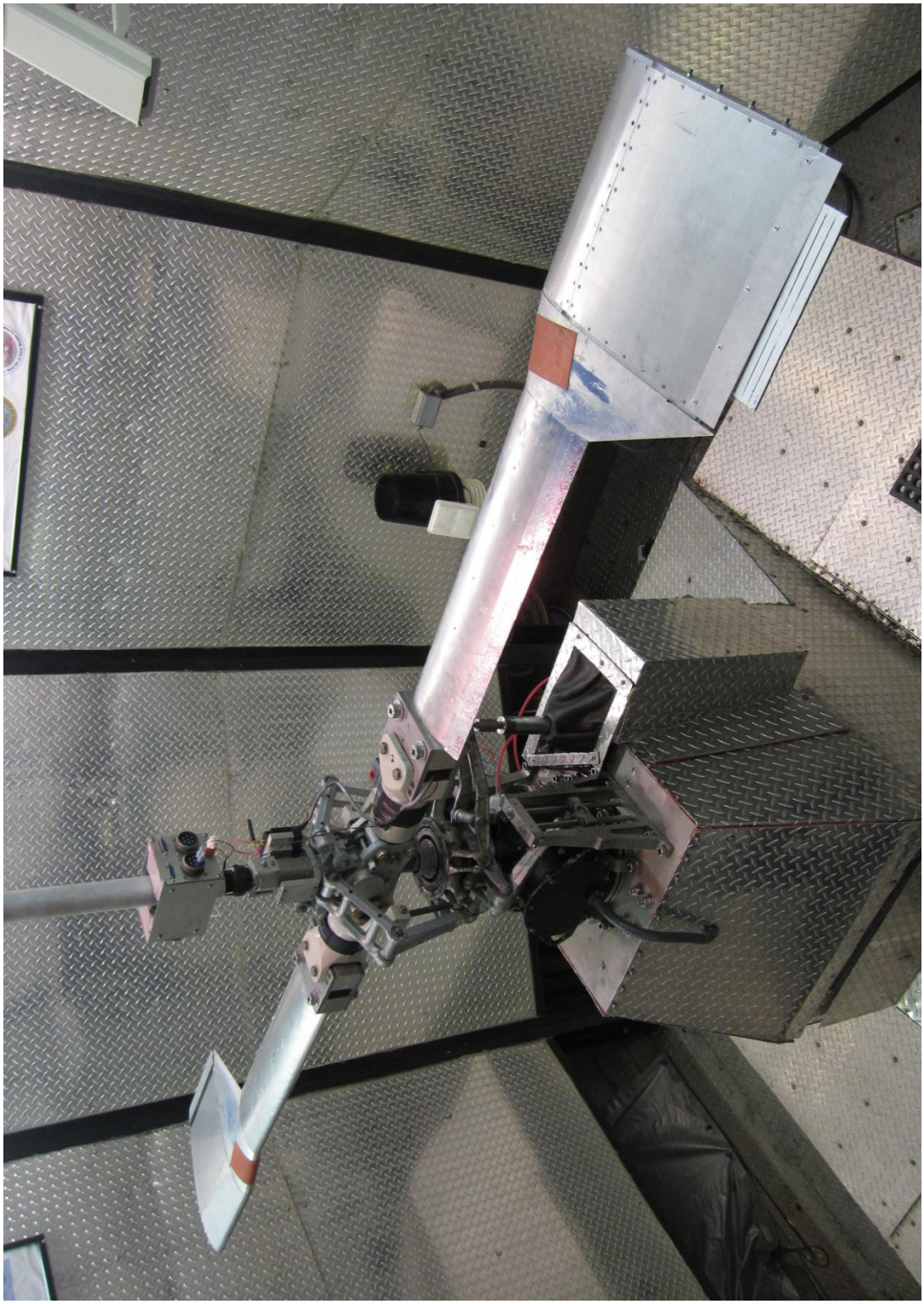

Figure 3-42: Extendable chord system installed in AERTS facility.

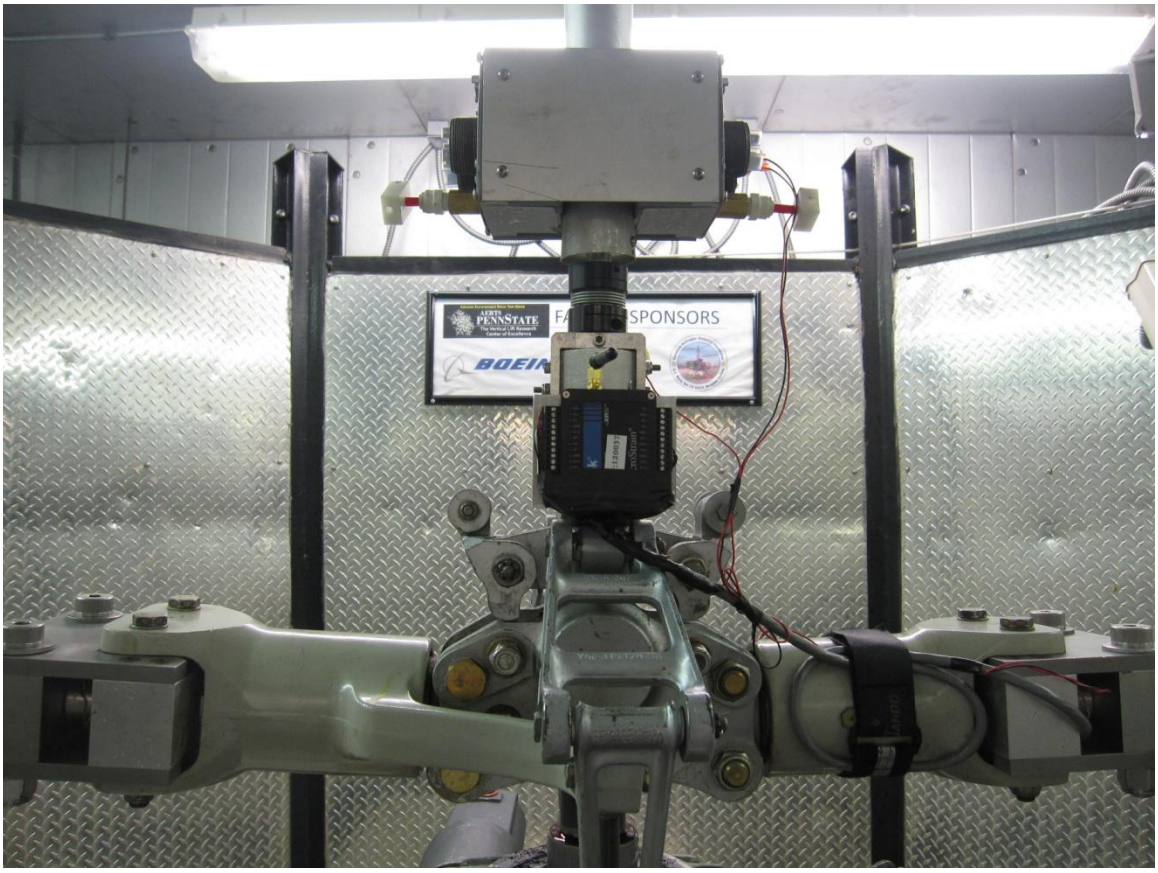

Figure 3-43: Rotor hub with wireless transmitter and slip ring.

As shown, the electromechanical actuator is powered using the red and black wires attached to the slip ring. All of the system measurements are passed via the gray cable through the inner blade structure to the wireless transmitter (Figure 3-43). The data is then streamed in real time to USB base station inside the control room (Figure 3-44). Also shown in this figure is the power source which supplied the 24 VDC to the actuator. The direction of the actuator was controlled simply by switching the positive and negative leads. All of the rotor stand properties, such as rotational speed, blade pitch, etc., are controlled using the panel shown in Figure 3-45.

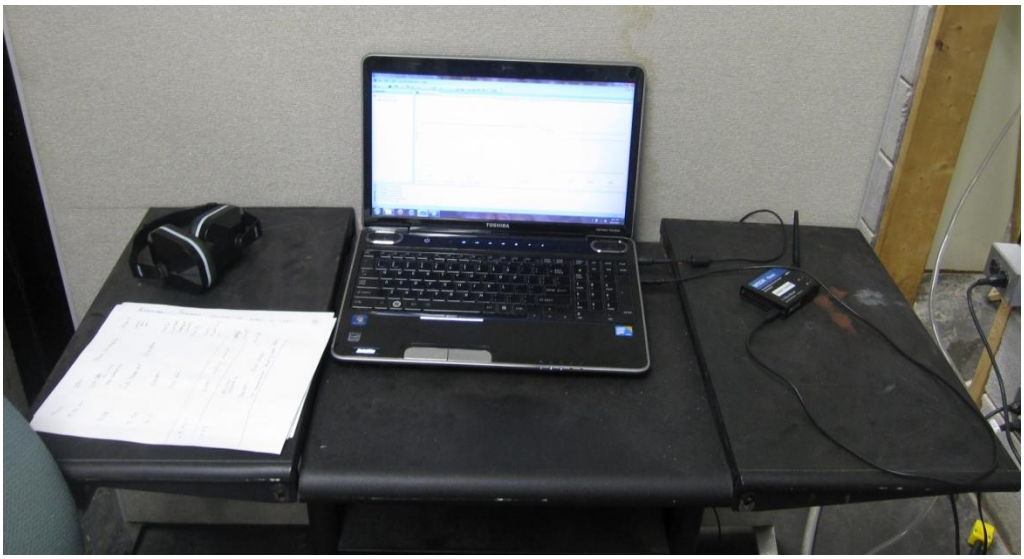

Figure 3-44: Workstation and USB wireless receiver.

Figure 3-45: AERTS control room.

Unfortunately, the first set of tests failed to meet the goals of the experiment in terms of chord extension at acceptable acceleration limits. The prototype was thoroughly investigated after each test and modifications were made to improve the system, the details of which follow.

3.7.1 Actuation Transmitter Failure

The first centrifugal test on the rotor test stand was conducted using the aforementioned extendable chord design shown in Figure 3-36. While static tests, i.e. 0 RPM, for this system showed proper plate deployment, the structure failed to actuate with the rotor spinning. This failure was observed even at very low rotational speeds. After stopping the rotor, the system would immediately resume normal operation, and the plate would deploy. It was hypothesized that the actuation transmitter may have been jamming under the centrifugal loading.

An investigation into this hypothesis was conducted with the blades removed from the rotor stand. It was seen that even with a small chordwise load (applied by hand) on the plate assembly, the resultant moment would cause a rotation of the actuation transmitter. This slight rotation would cause the actuation transmitter to be jammed against the guide rail which would worsen as the actuator output force increased to overcome the increase in friction. Ultimately, it was determined that in order to solve this issue, the moment had to either be reduced or eliminated entirely.

The first solution involved shortening the overall length of the actuation transmitter, thereby reducing the moment arm between the linkage pin and the actuator pin. Figure 3-46 and Figure 3-47 show the difference between the two actuation transmitters. The shorter actuation transmitter has a moment arm of 0.75 in, half that of the original design.

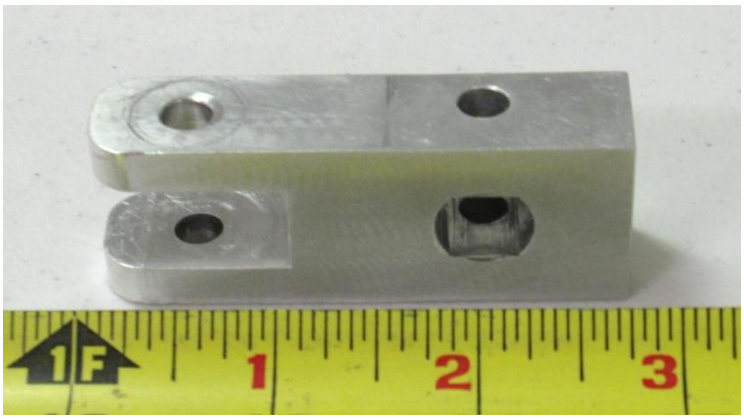

Figure 3-46: Initial actuation transmitter.

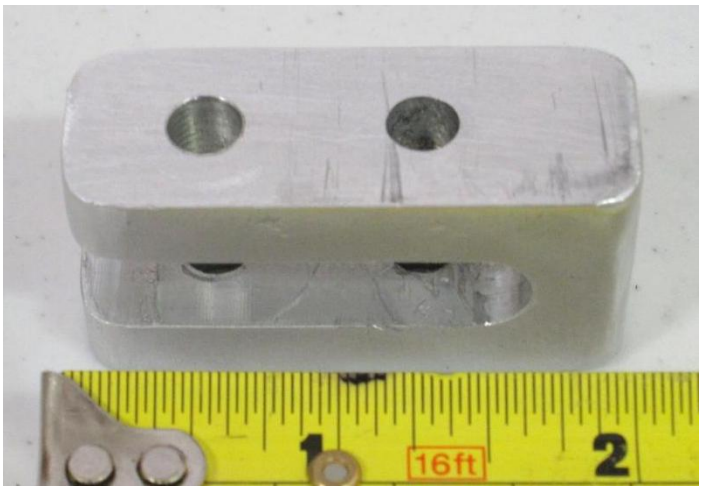

Figure 3-47: Shortened actuation transmitter.

Benchtop testing of the system was conducted in an attempt to reproduce the environment in which this failure was observed. By knowing the radial location and weight of the plate assembly, it was possible to calculate the chordwise component of the centrifugal force that would be transferred to the linkage. The maximum load was found to be approximately 175 lbs at full scale centrifugal acceleration. This load was then applied to the plate assembly by hanging weights attached to a cable-pulley system (Figure 3-48).

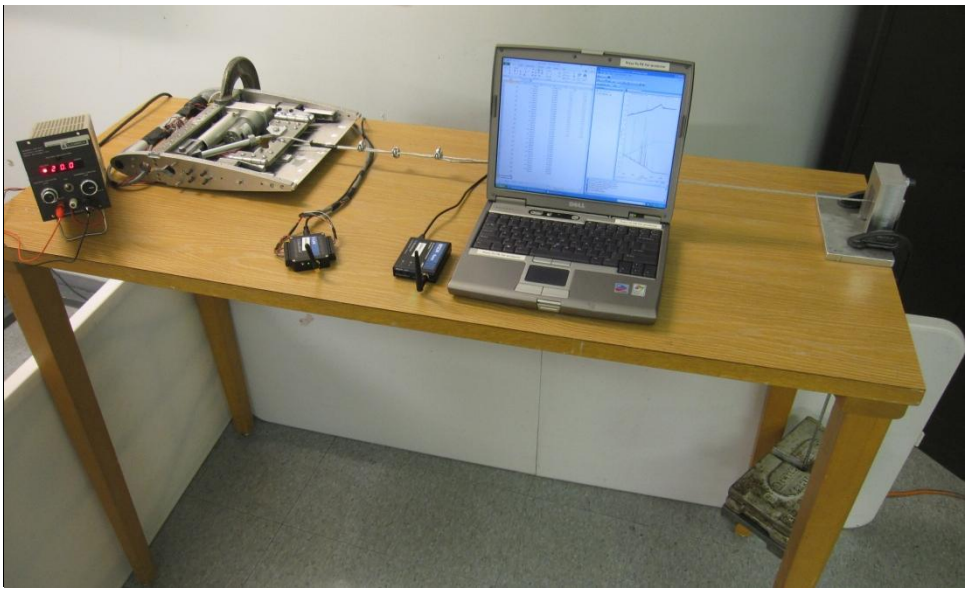

Figure 3-48: Benchtop testing setup.

This configuration proved to be more successful than the previous design which failed with even the slightest chordwise load. The deployment and retraction time range observed during these test have been compiled in Table 3-3.

Table 3-3: Deployment and retraction time during benchtop testing.

Chordwise Force (lbs)	**Deployment Time (s)**	**Retraction Time (s)**
0	9.2	10.5
21	8.3	7.3
41	8.0	8.0
61	7.7	8.9
81	7.0	11.8
101	7.8	N/A
111	8.2	N/A

In general, as the hanging weight was increased from 0 lbs to 101 lbs, the deployment time decreases while the retraction time increases. This is to be expected as the chordwise load is assisting deployment and opposing retraction. However, when the weight reaches 101 lbs and

111 lbs, the system deploys properly but stalls during retraction. Upon investigation, this again was a result of the jamming due to rotation. This can easily be seen in Figure 3-49.

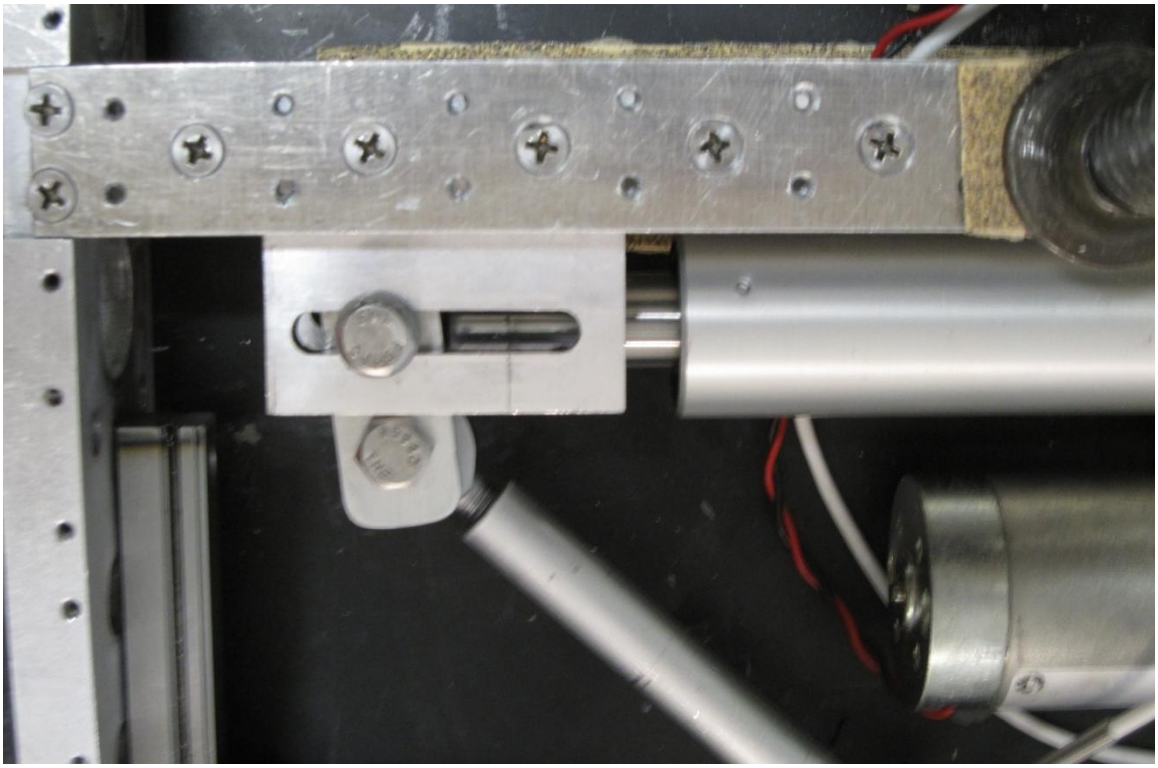

Figure 3-49: Jamming of the actuation transmitter for the second generation prototype.

This slight rotation again causes the corner of the actuation transmitter to be pressed firmly up against the vertical wall of the guide rail near the spar, thus increasing friction exponentially. While the hanging load of 111 lbs corresponds to a rotor stand rotational speed of approximately 460 RPM, this may likely occur much sooner due to spanwise loading, vibrations, etc. which have not been included in this test. Therefore, it was determined that to ensure operation of this system on the rotor stand, the moment at this point must be eliminated.

Removing the actuation transmitter moment was accomplished by creating a coincident joint between the linkage and the actuator (Figure 3-50). Essentially, the actuation transmitter has been eliminated as a separate component and is now incorporated into the linkage itself.

Benchtop tests of this configuration were successful up to, and including, 199 lbs which was the maximum available. Similar to the previous test, the deployment time decreases slightly and the retraction time increases with increasing chordwise load. Due to the new geometry, the chordwise extension is slightly reduced to a maximum of approximately 1.3 in which demonstrates a good correlation with the analytical kinematics. Furthermore, the force and moment analysis was updated to account for the removal of the extra degrees of freedom. The results of this analysis will be presented later in the chapter and compared against the experimental results.

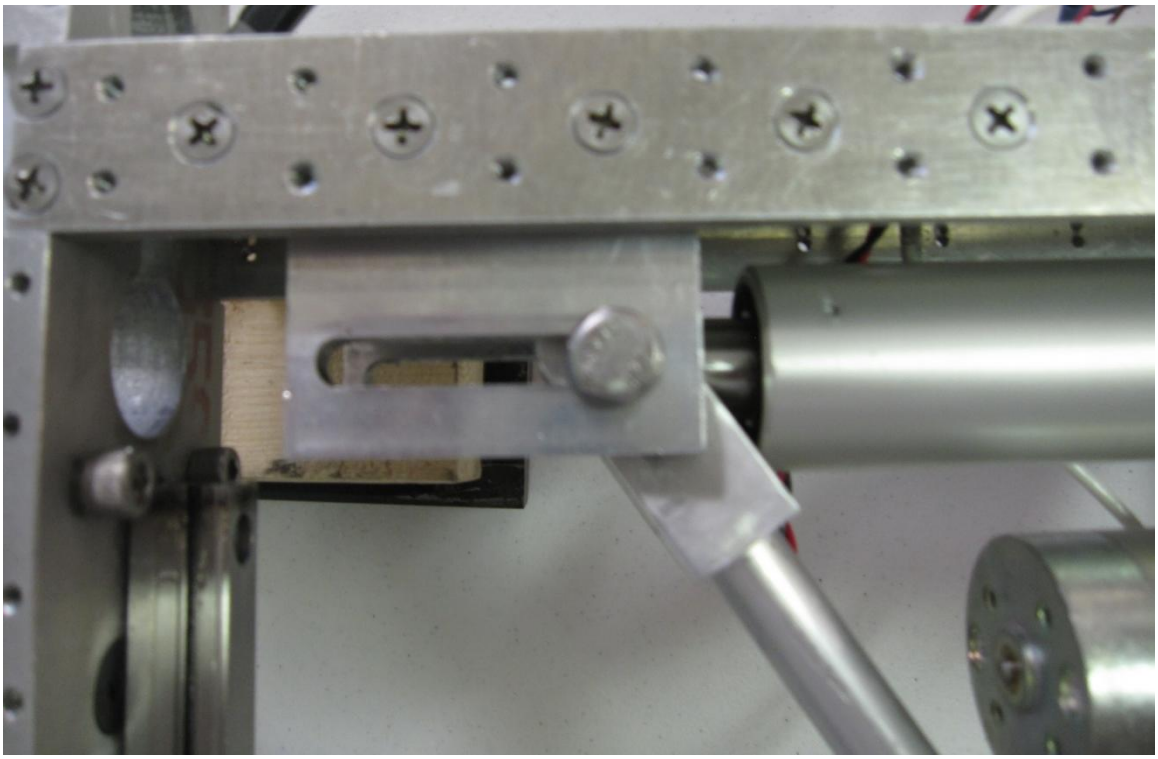

Figure 3-50: Third generation coincident actuation transmitter.

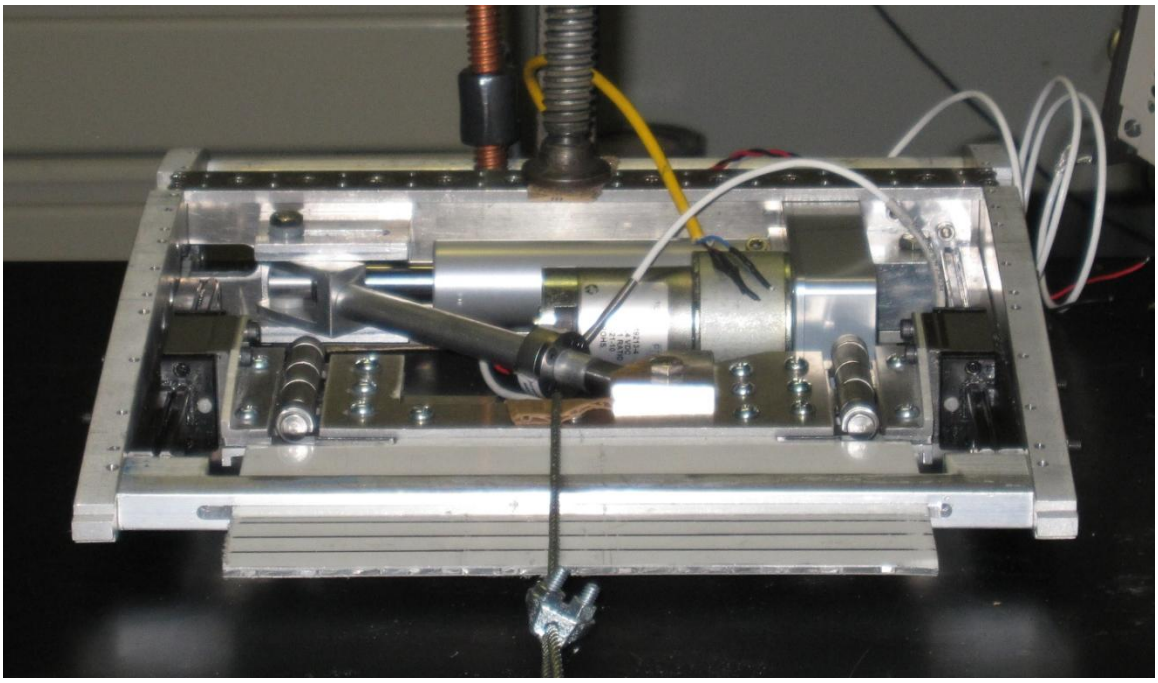

Figure 3-51: Rear view of third generation actuation transmitter during benchtop testing.

While this modification solves the jamming issue, it does so at the expense of a necessary design element: three-axis rotation of the linkage. The linkage is now constrained to rotate about the pinned joint which only allows for planar motion. Ultimately, this system would not be suitable for a twisted blade section. This could be corrected in future designs by incorporating an actuator with a C-shaped attachment, similar to the one currently on the linkage, which is then pinned to the original rod end. This was not done in the current study due to space constraints in the spanwise direction.

3.7.2 Electromechanical Actuator Failure

With the apparent jamming issue solved, the extendable chord system was once again installed onto the AERTS. However, once again the system failed to actuate at rotational speeds above 150 RPM, or approximately 31.8 g's. Unlike the previous test though, this time the current

through the actuator spiked to 2 A, which was limited by the power source itself. Even after slowing the rotor, the actuator failed to operate. Instead, a quiet clicking sound was observed whenever voltage was applied in either direction. Only after attempting to manually displace the plate and cycling the power on the actuator would the system resume proper operation. This type of behavior indicated an electrical short inside the actuator.

To ensure that the extendable chord system itself was not binding in any way, the actuator was disconnected from the linkage and rotated at various speeds. Correct performance was observed for the isolated actuator at 0, 71, and 100 RPM; or 0, 7.1, and 14.1 g's, respectively. However, at rotational speeds above 145 RPM (29.7 g's) the actuator shorted out and failed to operate. While this experiment failed to validate the extendable chord system, it does however demonstrate the difficulties associated with selecting and designing an actuation system for morphing rotor blades.

This actuator was then removed from the system and returned to Ultra Motion for further investigation. It was determined that under the centrifugal loads, a springs supporting a thrust washer on one of the gears in the gear train was being compressed causing a binding between two gears. This issue was solved by the manufacturer by modifying the thrust washer such that the spring was no longer required to support the gear. Upon receiving the modified Bug actuator, benchtop testing was conducted during which the actuator performed successfully. Considering the fact that the actuator failed only under centrifugal loads, which benchtop testing could not reproduce, the results of this test are nearly identical to the previous version and thus will not be presented here.

3.8 Modified Electromechanical Actuator

The subsequent sections of this chapter present the spin test results of the extendable chord system using the coincident actuation transmitter and modified electromechanical actuator detailed previously. Figure 3-52 show this system installed in the AERTS facility.

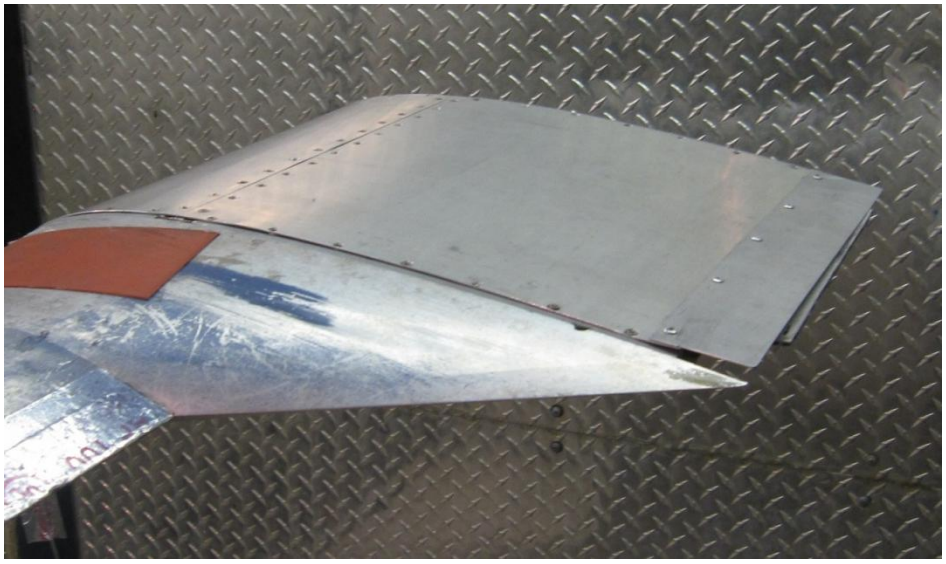

(a)

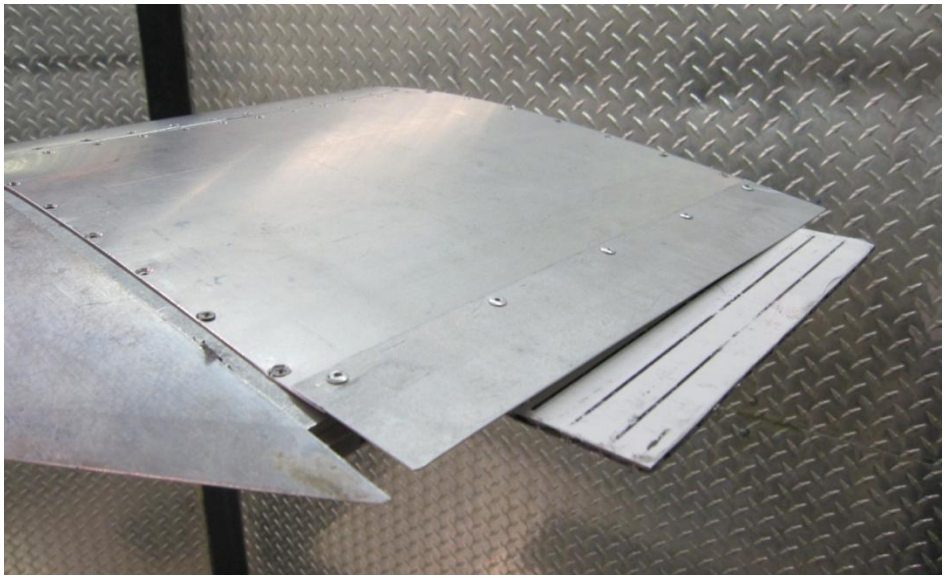

(b)

Figure 3-52: Modified EMA system in the AERTS facility in the (a) retracted and (b) extended configurations with skin.

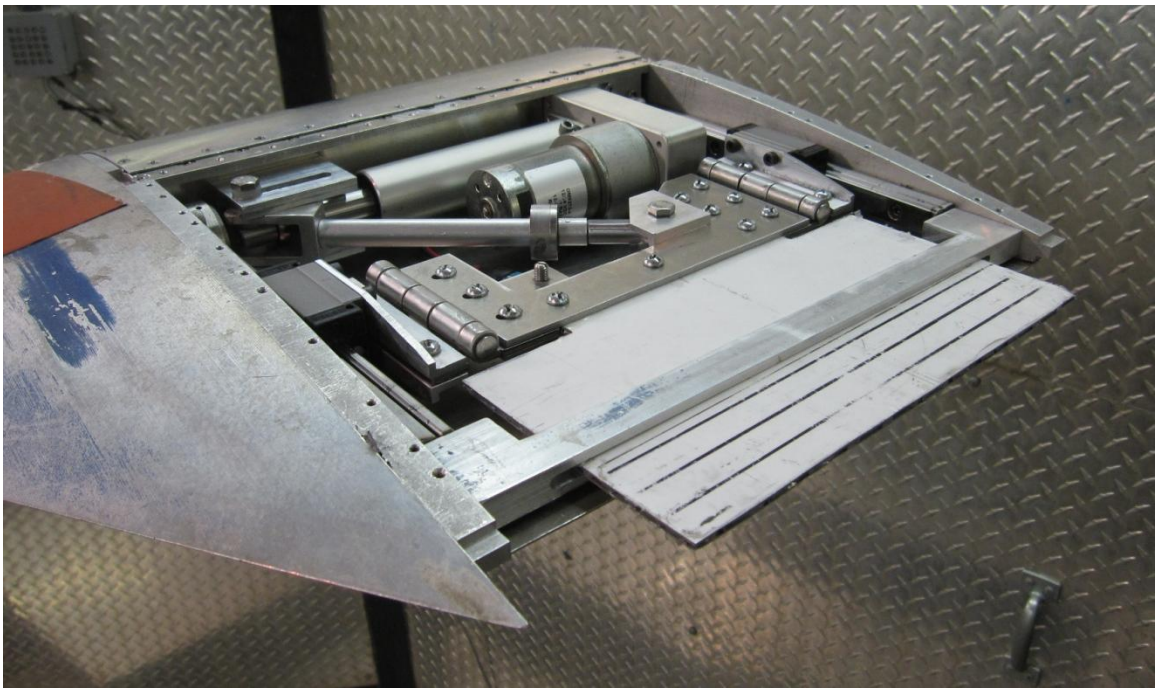

(a)

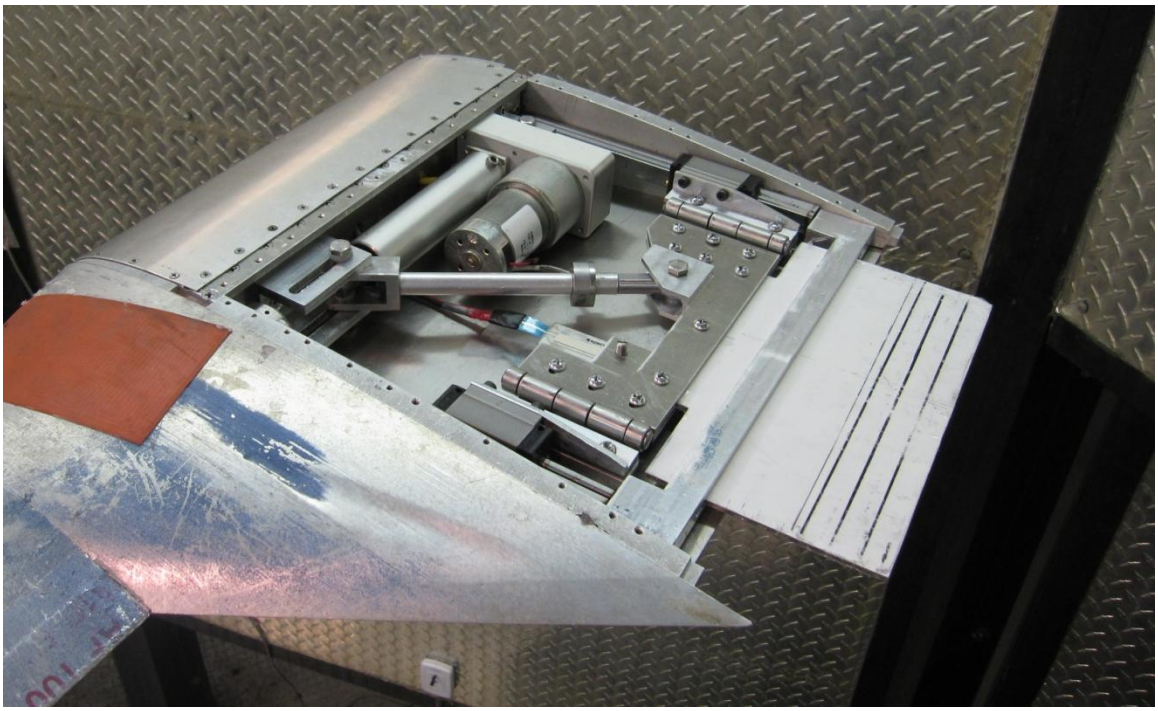

(b)

Figure 3-53: Modified EMA system in the AERTS facility in the (a) retracted and (b) extended configurations without skin.

The extendable chord system was actuated at multiple rotational speeds: 0, 125, 150, 200, 250, 300, 350, 375, 385, 390, and 400 RPM. Data was collected during both extension and retraction of the system. As previously mentioned, this includes actuator displacement, plate extension, load cell force, actuator current, and rotor speed. Unfortunately, the SoftPot used to measure the plate displacement experienced an error during testing. This was caused by the deformation of the aluminum skin to which the potentiometer was mounted. The skin was displaced downward due to the vertical centrifugal load on the mounting block resulting from the 3° precone. It is important to note, however, that the SoftPot measurement exhibited a very good correlation to the actuator displacement and the analytical kinematics of the system during benchtop testing. This fact, along with a qualitative visual confirmation from the cameras, provided sufficient evidence that the relationship between actuator displacement and plate extension remained constant during the spin test and that the device reached its maximum extension of 1.3 in (when applicable).

3.8.1 Results

Overall, the spin tests demonstrated the operability of the extendable chord system up to a rotational speed of 385 RPM. This corresponded to a centrifugal acceleration of approximately 209.5 g's, which was significantly below the full scale acceleration (444 g's) and the 500 RPM goal of the test as well (353.3 g's). Figure 3-54 and Figure 3-55 show the time history of the displacement of the electromechanical actuator for various rotational speeds.

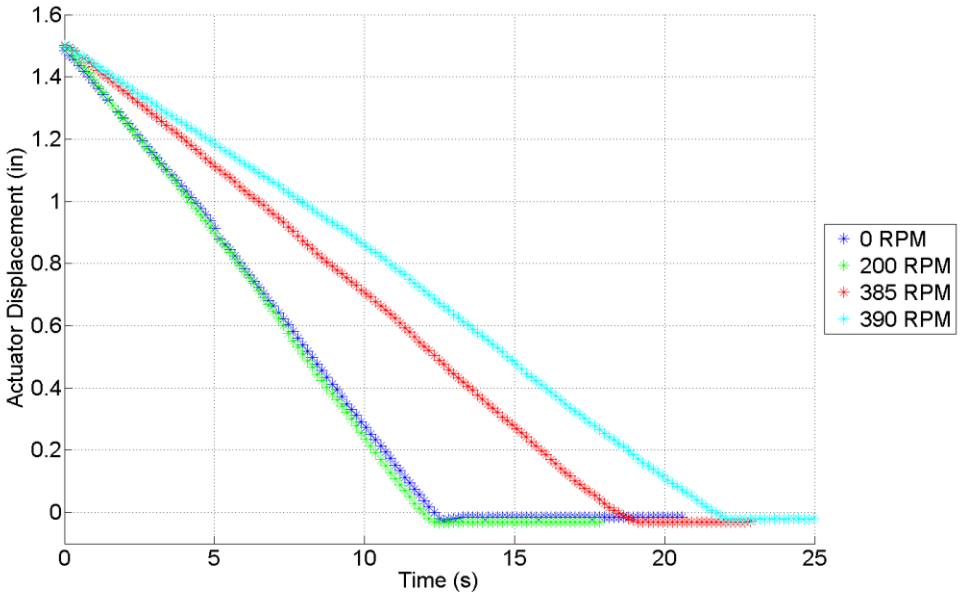

Figure 3-54: Time history of EMA displacement during plate extension.

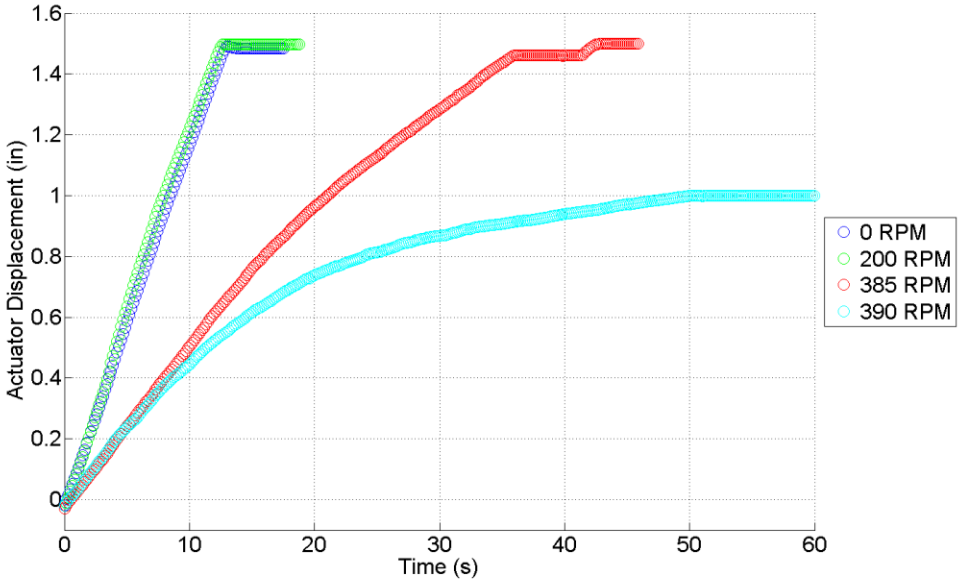

Figure 3-55: Time history of EMA displacement during plate retraction.

Table 3-4: EMA actuation time for various rotational speeds.

Rotational Speed (RPM)	Deployment Time (s)	Retraction Time (s)
0	12.6	13.0
200	12.5	12.6
385	19.3	37.3
390	22.2	N/A

As previously mentioned, while the extendable chord system successfully deployed and retracted for rotational speeds up to 385 RPM, the device stalled during retraction at 390 RPM. Furthermore, while the rate of extension and retraction is similar for the 200 RPM test as the static rotor test, the actuation time significantly increases for higher centrifugal accelerations. However, since this device is meant to be quasi-steady, whether or not these actuation time limits are acceptable would depend upon the needs of the specific mission.

Not only does the actuation time increase with centrifugal acceleration, but the current through the actuator does as well. The average current for a given rotational speed is displayed in Figure 3-56. This current reading was monitored using the digital output on the power source. Considering the 24 VDC input voltage, the motor power can also be calculated (Figure 3-57). Obviously the current (and power) is higher for retraction due to the increase in the actuation force. In a non-rotating system, it would be possible to use these measurements to obtain an approximate actuator force through an efficiency curve. However, when applying this calibration to the motor in the rotating frame, the output force calculated is unrealistically large. Although the Bug actuator with the modified gearing is functioning, the efficiency of the system is clearly reduced. For instance, the maximum current for this actuator on the benchtop was measured to be 0.79 A. In the rotating frame, on the other hand, the maximum current was found to be 1.65 A during retraction at 385 RPM. This corresponds to 40 W of power required to actuate the system.

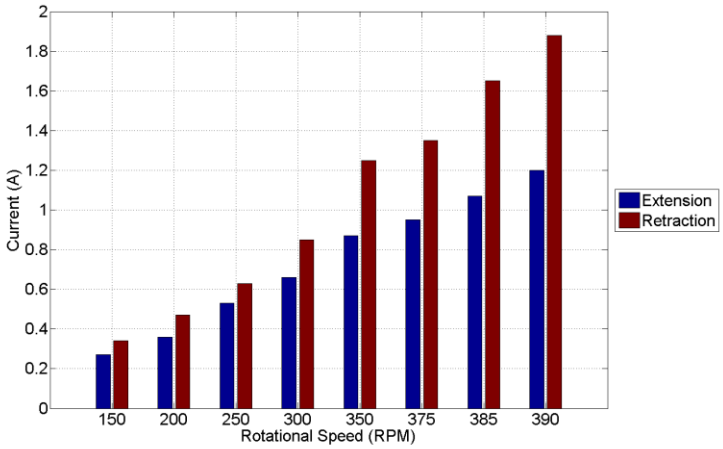

Figure 3-56: Average current through EMA during actuation of extendable chord system.

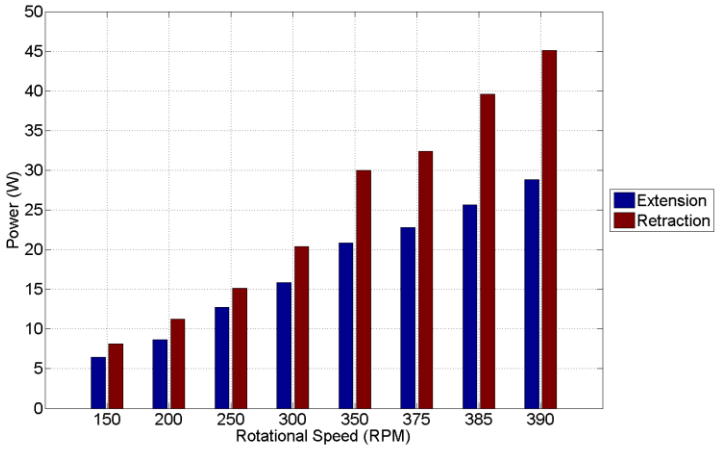

Figure 3-57: Average power through EMA during actuation of extendable chord system.

The output from the LC202-300 load cell can be seen in Figure 3-58. Obviously, there is a significant increase in the force as the RPM increases. It is important to note that the decrease in force as the device is extended (i.e. actuator displacement tends to 0) is a result of the nut securing the linkage to the plate assembly impacting the bottom skin. Thus, the amount of force required by the linkage to hold the plate assembly is reduced. It can also be seen that, as expected, the force in the linkage is increased during retraction due to the friction in the system.

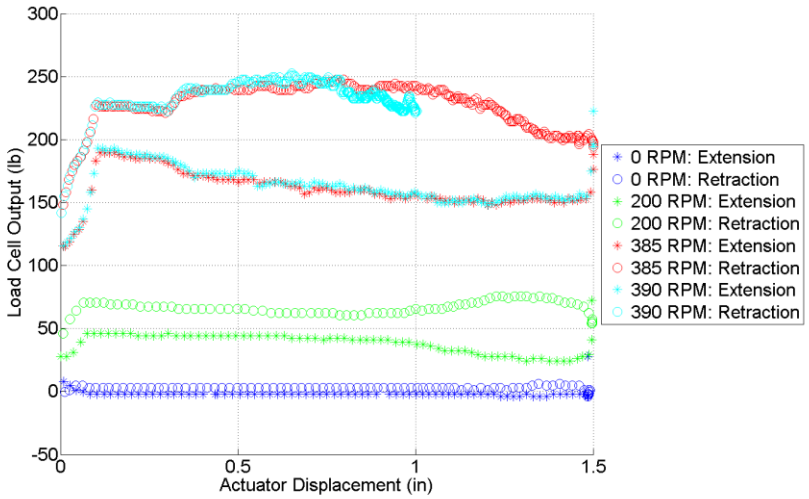

Figure 3-58: LC202-300 output during EMA extendable chord system actuation.

3.8.2 Comparison with Analytical Solution

The numerical estimation for the axial force in the load cell can be seen in Figure 3-59. Clearly, there is a large discrepancy between the two with the measured force being more than double the estimated force.

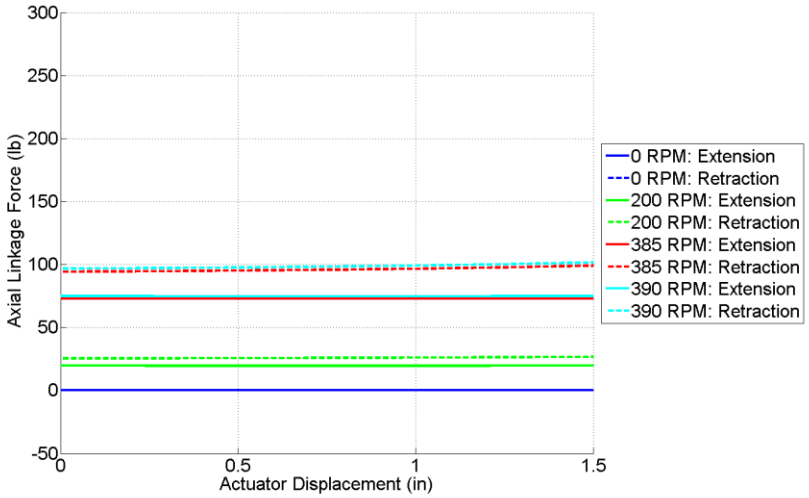

Figure 3-59: Numerical solution of axial linkage force.

There are two possible explanations for this effect. The first assumes that the load cell force during the experiment is higher due to various phenomena not captured by the rigid body analysis. For example, elastic deformations within the system, such as the ribs, linear slides, etc., would certainly affect the loads in the linkage. Unfortunately, capturing this effect would involve the use of more sophisticated models, which was not pursued as part of this research.

On the other hand, a second hypothesis is that the load cell did not provide an accurate measurement of the axial force under centrifugal loading. Considering the fact that the load cell is designed to operate axially, this is could be significantly contributing to the difference between the numerical analysis and the experimental results. Although there is no external load directly applied to the linkage, the weight of the linkage and the load cell generate a transverse shear force under a centrifugal acceleration. The shear force at the load cell calculated using the numerical analysis may be up to 8.5 lbs. Using this as a guide, a first order estimation of the shear effects on the LC202-300 load cell was conducted on the benchtop (Figure 3-60).

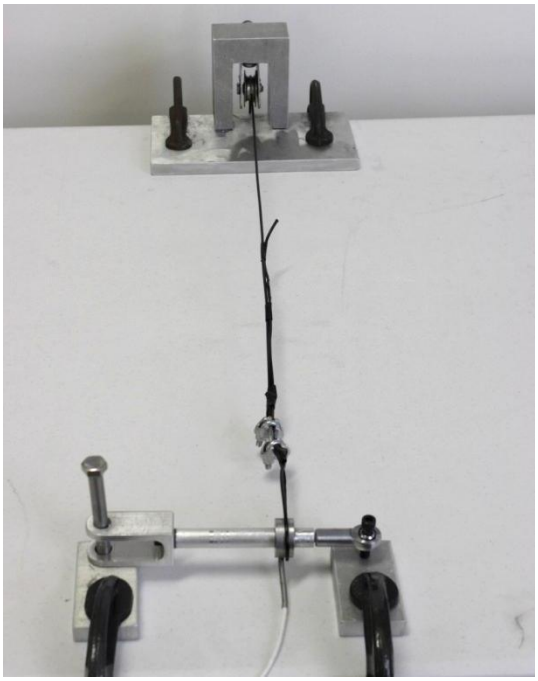

Figure 3-60: LC202-300 transverse shear correction calibration.

This test was structured in a similar manner to the chordwise centrifugal load test. The supports were securely clamped to the benchtop which provided a pinned boundary condition for each end of the linkage. A cable was wrapped around the load cell with the other end going through a pulley and attaching to a hanging pan. The transverse load was applied in increments of 0.5 lbs using weights. The calibration curve shown in Figure 3-61 displays the amount of false tensile force measured by the load cell for a given transverse shear load.

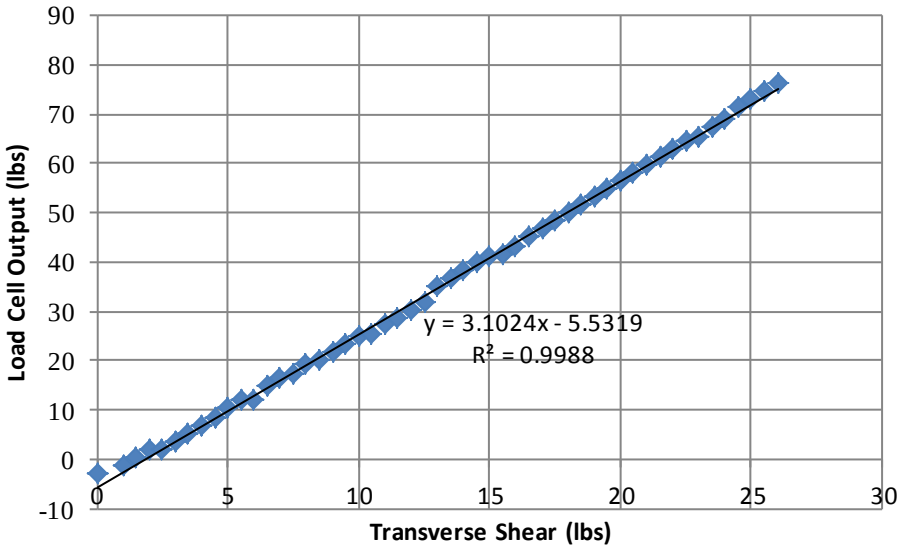

Figure 3-61: Transverse shear effect on LC202-300 load cell.

Using a linear regression, this calibration was then implemented into the numerical analysis to provide a first order approximation of the transverse shear effects. Obviously this test does not include axial force as well as transverse shear which may result in a nonlinear relationship not captured here. The analytical load cell output including shear is shown in Figure 3-62.

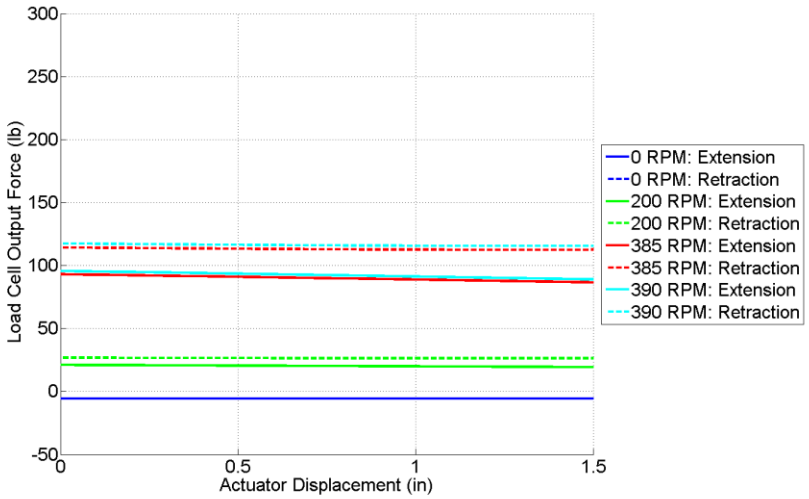

Figure 3-62: Numerical solution of load cell output with shear correction.

Although the transverse shear on the load cell certainly increases the load measurement, it may only account for up to 20 lbs given this calibration. Transverse shear alone is not enough to sufficiently explain the discrepancy between the experiment and analysis. Ultimately, it is most likely a combination the centrifugal field effects, including transverse shear, and the assumptions made in the rigid body modeling of the system.

Chapter 4

Centrifugal Test Prototype: Pneumatic Actuator

following sections will introduce the design of the pneumatic prototype and present the results of the spin test conducted in the AERTS facility. Finally, a comparison of these results with the numerical analysis will be provided.

4.1 Design Requirements

Pneumatic actuators have been considered for the extendable chord system due to their relative simplicity, as compared to geared electromechanical motors, as well as their high force output for a given size. Previous work demonstrating the effectiveness of pneumatic actuators in morphing rotor blades has been conducted Woods et al (Ref. 25). As mentioned, this test will be conducted in the same manner as the EMA prototype in the AERTS facility. Rather than using the electrical slip ring to power the actuator, this prototype will make use of an air compressor and pneumatic rotary union. The rotary union installed in the AERTS facility is manufactured by Rotary Systems, model 012-N-21212, and has a maximum air pressure rating of 250 psi (Ref. 26). However, as the rotational speed is increased, the likelihood of burning up the interior seals increases and the maximum pressure is therefore reduced. For this reason, the maximum pressure the AERTS facility could provide for this test was 105 psi. Furthermore, much of the test

structure remains identical to the EMA design. Any changes made will be detailed in the following section.

4.2 Pneumatically Actuated System Design

4.2.1 Modifications from EMA Prototype

Due to the fact that this prototype was fabricated after the EMA design, a few additional changes have been implemented to improve the system based on the results of the previous work. First of all, upon examining the railing along the spar which supports the sliding pin joint connected to the linkage, it was discovered that the chordwise force had caused the bolt threads to carve out groves along the inside of the railing. This was significantly increasing friction and thus increasing the required actuation force. Therefore, it was determined that incorporating a motion linear slide designed to support the chordwise restraining force would significantly reduce the friction.

Secondly, it was observed during the test of the electromechanical prototype that the chordwise force on the plate and the spanwise force on the actuation transmitter and rod were both contributing to the extension of the system. Furthermore, the actuator was required to provide a restraining force during extension and retraction. By switching the direction of the actuator, the spanwise force on the actuation transmitter and EMA rod would cause the system to retract. On the other hand, the chordwise force on the plate assembly would be working to extend the system. By carefully balancing the masses of these components it may be possible to reduce the actuation force while maintaining the one-way direction of the actuator force. However,

while it may theoretically possible to significantly reduce actuation force, the existing prototype design and available slider components did not allow for the system to be optimized.

4.2.2 CAD Model

As shown in Figure 4-1, the pneumatic actuator prototype incorporates many of the same components used in the EMA design.

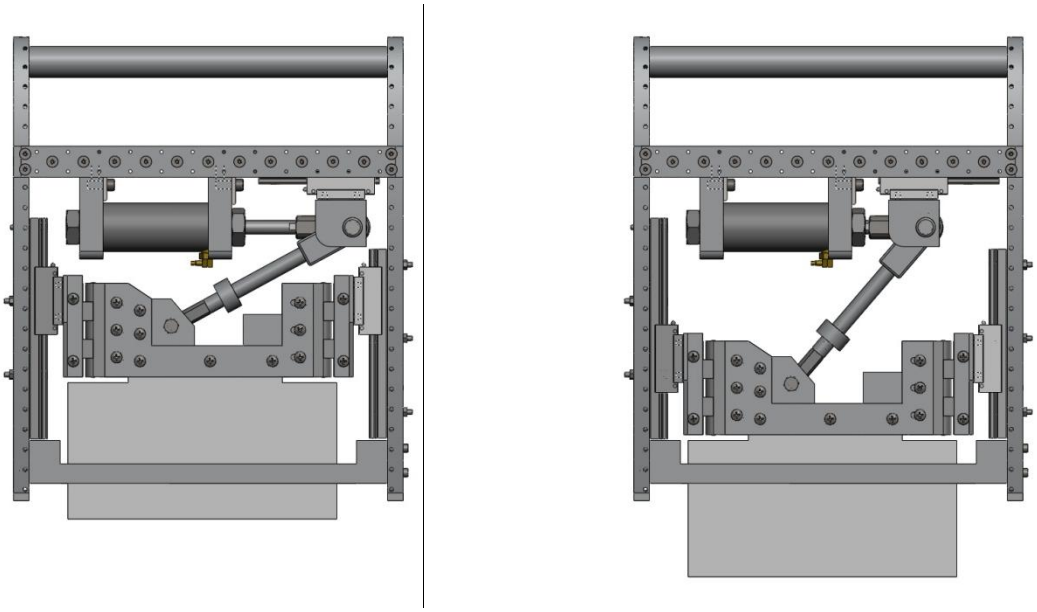

(a) (b)

Figure 4-1: CAD model of pneumatically actuated, extendable chord system in the (a) retracted and (b) extended configurations.

For example, the plate assembly uses the same parts and has simply been flipped to account for the new position of the actuator. The linear slides remain nearly identical except for a slight shortening of the outer slide to allow the actuator to fully extend. One of the new components in this design is the linear slide along the spar which is identical to the linear slides

on the ribs. In addition, the length of the linkage had been adjusted to maximize the plate extension.

The pneumatic actuator shown in this figure is based on a Stainless Steel Pneumatic Cylinder developed by Clippard Instrument Laboratory, Inc (Ref. 27). Due to the geometry of the test section, the largest bore diameter was limited to 1.5 in. Several properties were taken into consideration when selecting the exact pneumatic actuator, including overall length, mount type, force direction, and piston type. This will be described further along with an estimate of the required forces and moments using the analysis in the next section.

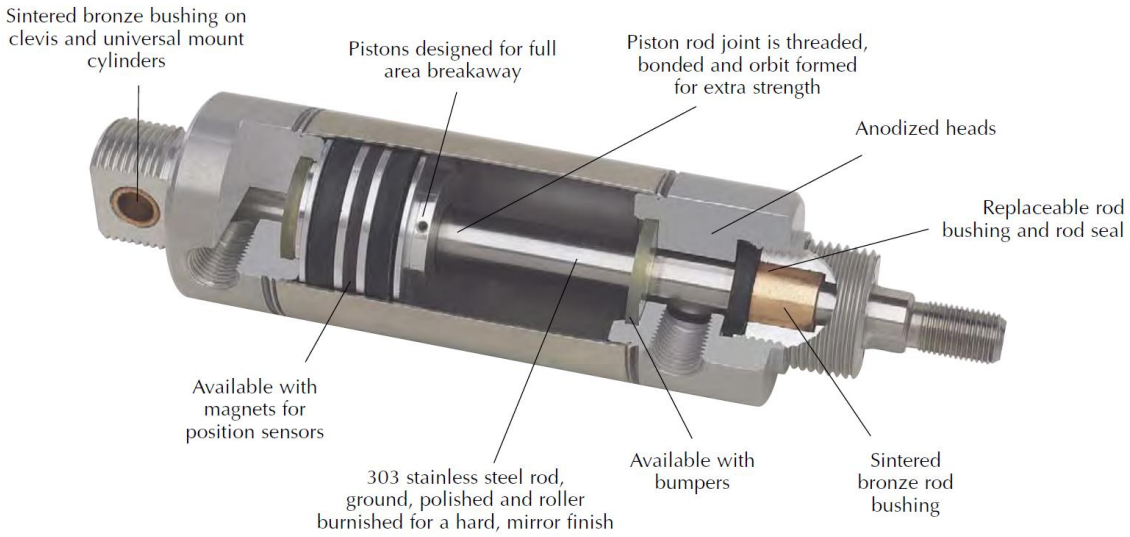

Figure 4-2: Clippard Stainless Steel Pneumatic Cylinder (Ref. 27).

4.3 Force and Moment Analysis

The diagram shown in Figure 4-3 was used to determine the kinematics and loads in the pneumatic prototype. The system was split into three components: plate assembly, linkage, and actuator mass. The actuator mass consists of the steel pneumatic piston, ball slide, aluminum pin mount connected to the slide, and steel pin. It is this mass that should ultimately be optimized to

balance the forces and reduce the actuation requirements. Of particular interest in this analysis are the chord extension, required actuator force, rib linear slide force, and spar linear slide force.

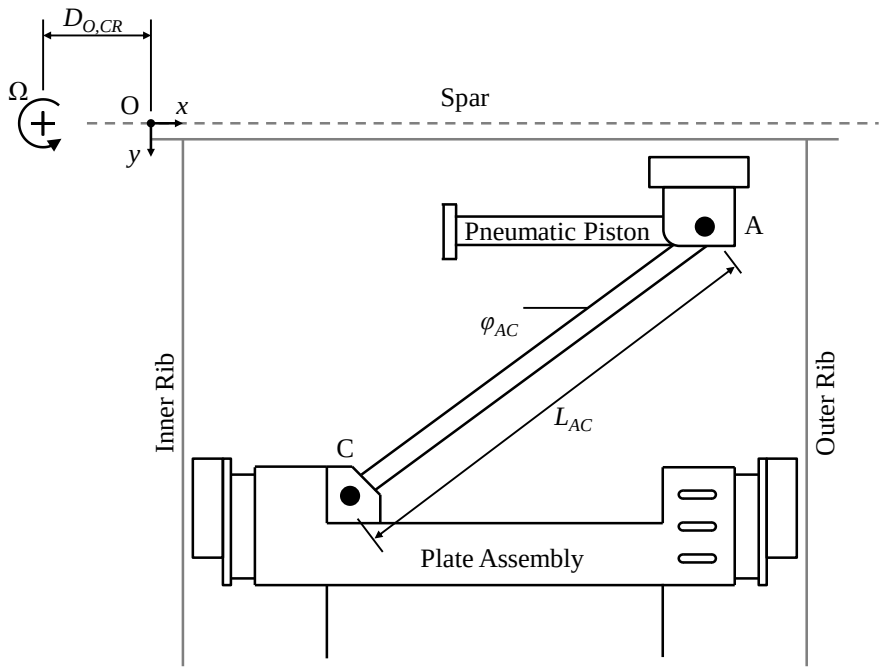

Figure 4-3: Pneumatically actuated, extendable chord system kinematics.

Applying the two dimensional force and moment equations to this system at a rotational speed of 500 RPM provided the results shown in Figure 4-4 through Figure 4-7. With this geometry, the maximum plate extension is around 1.85 in. Due to the configuration of the system, the magnitude of the force required in extension is larger than retraction. Thus, only the extension requirements have been shown here.

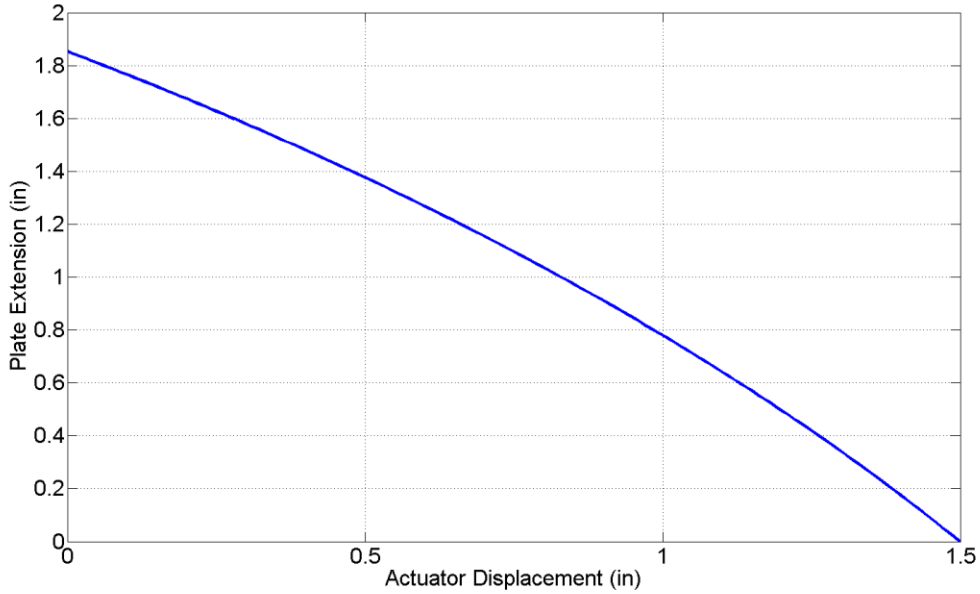

Figure 4-4: Plate extension for pneumatic system.

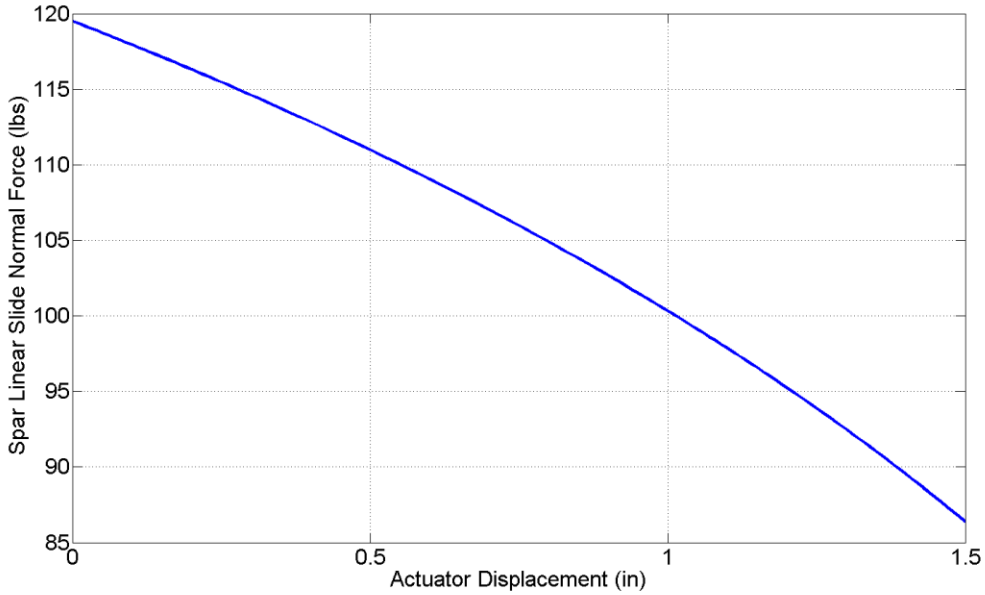

Figure 4-5: Spar linear slide normal force for pneumatic system during plate extension at 500 RPM.

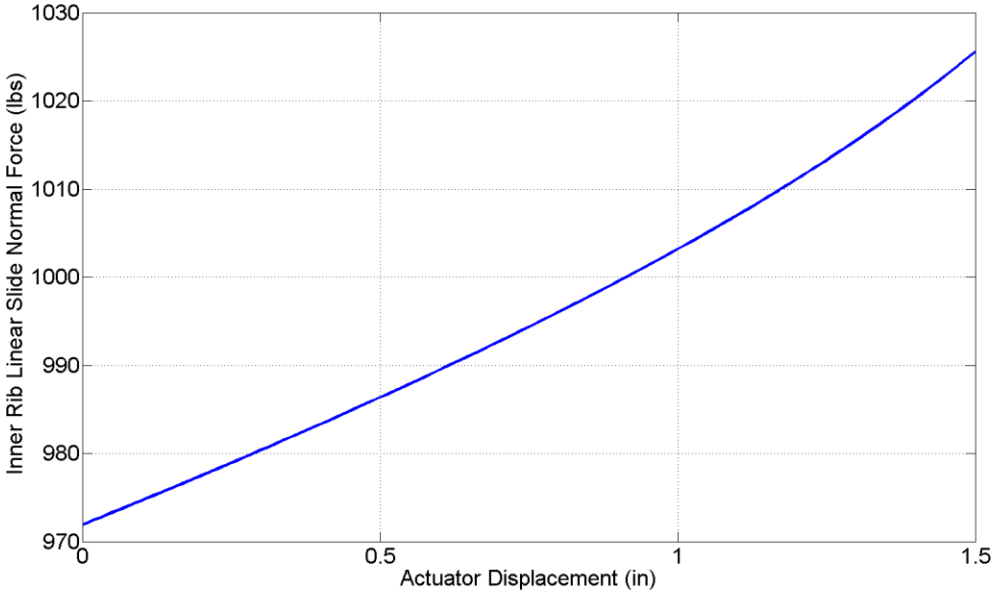

Figure 4-6: Inner rib linear slide normal force for pneumatic system during plate extension at 500 RPM.

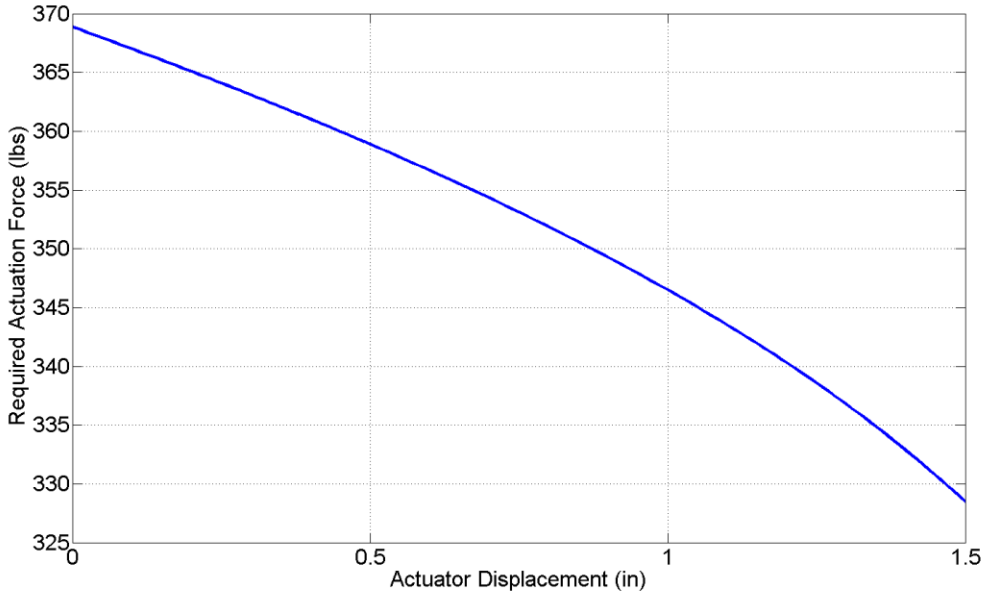

Figure 4-7: Actuation force required for pneumatic system extension at 500 RPM.

As shown, the maximum normal force on the spar linear slide is 120 lbs. Obviously the normal force on the inner rib slide is much larger, with a maximum of 1,026 lbs. These values

are well below the dynamic load capacity of the NSK LH15AN carriage (2,428 lbs). Figure 4-7 shows that the largest actuation force required occurs when the plate is fully retracted and is on the order of 369 lbs. Moreover, it can be seen that the force required extending and retracting the plate acts only in one direction. This high actuation forces clearly demonstrated the need for the largest actuator possible for this given space constraints. As previously mentioned, this corresponds to a cylinder with a bore diameter of 1.5 in. The force factor supplied by the manufacturer for this actuator is 1.55. This property is essentially the cross-sectional bore area which converts force to pressure. Strictly speaking, the area for this actuator is 1.77 in^2 and the reduction to the 1.55 force factor accounts for minor losses in the system. The estimated pressure required to extend the flat plate is shown in Figure 4-8.

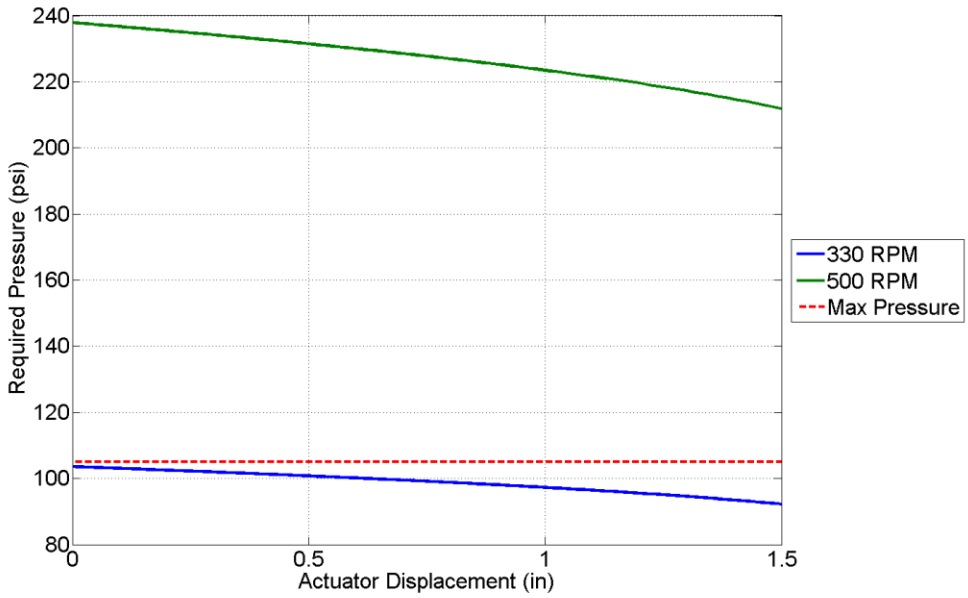

Figure 4-8: Pressure required for pneumatic system extension at various rotational speeds.

Unfortunately, due to the limitations of the facility and the retrofit nature of this design, the maximum rotational speed at which the flat plate would reach full extension was anticipated to be 330 RPM. It was also proven that by decreasing the mass of the moving actuator

components, i.e. the piston, ball slide, and pin mount, the required pressure could be significantly reduced. For instance, the current weight of these components is 1.13 lbs. However, if the mass was reduced by one-half, to 0.565 lbs, the pressure required is much lower (Figure 4-9). In fact, the system would even be able to actuate at the 500 RPM maximum for this facility. While the actuator mass has not been reduced for this prototype due to the available time and cost constraints, this is important to keep in mind when evaluating the success of this system and for any future work on this subject.

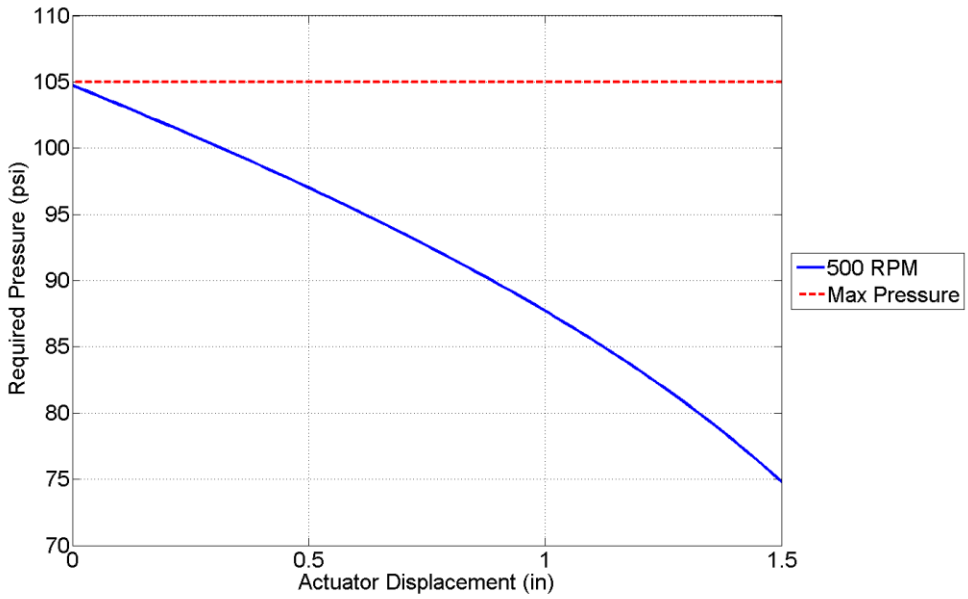

Figure 4-9: Pressure required for pneumatic system extension with reduced actuator component weight.

It should be noted that the finite element analysis conducted for the electromechanical actuator was not repeated for the pneumatic prototype due to the similarities in the designs, especially with regard to the moving plate assembly.

4.4 Pneumatic Actuator Prototype

The final pneumatic actuator prototype for the extendable chord system is shown in Figure 4-10. Overall, the internal extendable chord structure has a weight of 7.58 lbs.

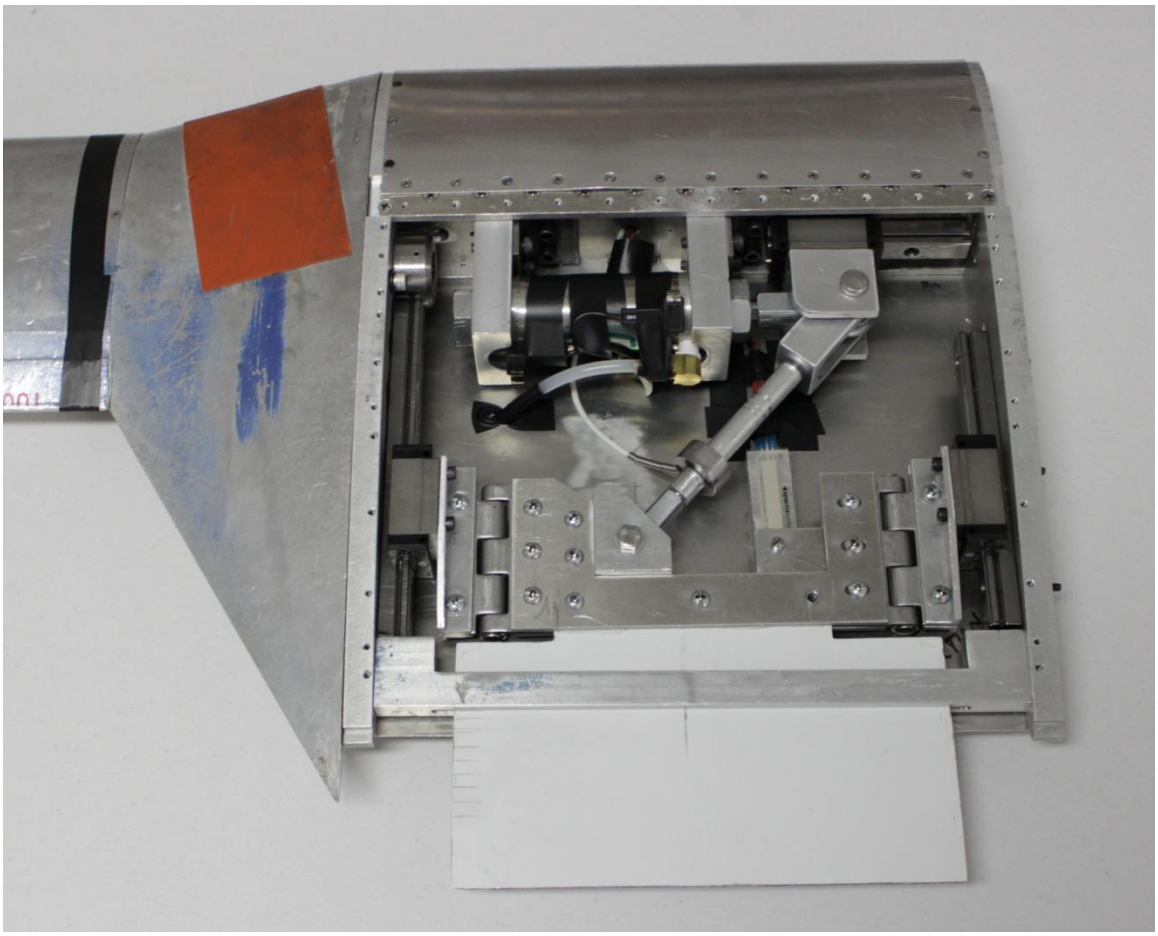

Figure 4-10: Pneumatically actuated extendable chord system.

The specific actuator chosen for this prototype was the Clippard Pneumatic Cylinder model EDR-24-1 ½-MB. As previously mentioned, this model has a 1.5 in bore diameter which provided the largest possible force output for the given space constraints. Although the actuation force is only required in one direction, this model features two ports for dual actuation which in fact shortened the overall length. Relevant data for this actuator has been compiled in Table 4-1.

Table 4-1: Clippard Pneumatic Cylinder properties (Ref. 27).

Property	**Unit**	**Value**
Part Number		EDR-24-1 ½-MB
Stroke	in	1.5
Max Pressure	psi	250
Bore Diameter	in	1.5
Force Factor		1.55
Length	in	7.375
Weight	lb	1.0

Unlike the electromechanical actuator, this actuator did not include a built in potentiometer to measure the actuator stroke. Rather, two Reed switches have been placed at the extrema of the piston to indicate when the actuator has reached full extension or retraction. Essentially these switches trigger a flag (0 or 1) to indicate that the piston is located at the given position. Also of note is that the SoftPot has been moved to coincide with the new position of the wiper. The SoftPot mount and wiper have been adjusted to correct for the error that occurred in the electromechanical test.

The pneumatic tubing exits the test section through a hole in the bottom skin due to the limited diameter of the conduit through the inner blade structure which is already carrying the sensor wires. This tubing is taped along the outside of the inner blade structure and is connected to the pneumatic rotary union via a quick connect fitting (Figure 4-11).

The remainder of this chapter discusses the results of the centrifugal test of the extendable chord system actuated with a pneumatic cylinder. The results will be presented in a manner similar to the electromechanical actuator and will also include a comparison to the analytical solution.

Figure 4-11: Pneumatically actuated extendable chord system installed in AERTS facility.

4.5 Pneumatic System

The extendable chord system was controlled inside the control room of the AERTS facility using three different methods. The first tests were conducted using a small compressor connected directly to the input port inside the control room. This pressure was not manually regulated and therefore it was only capable of providing a constant 66 psi.

The second control method involved the use of a large compressor shown in Figure 4-12. This compressor was capable of providing very high pressures but was limited to 105 psi due to the capabilities of the AERTS facility, specifically the rotary union.

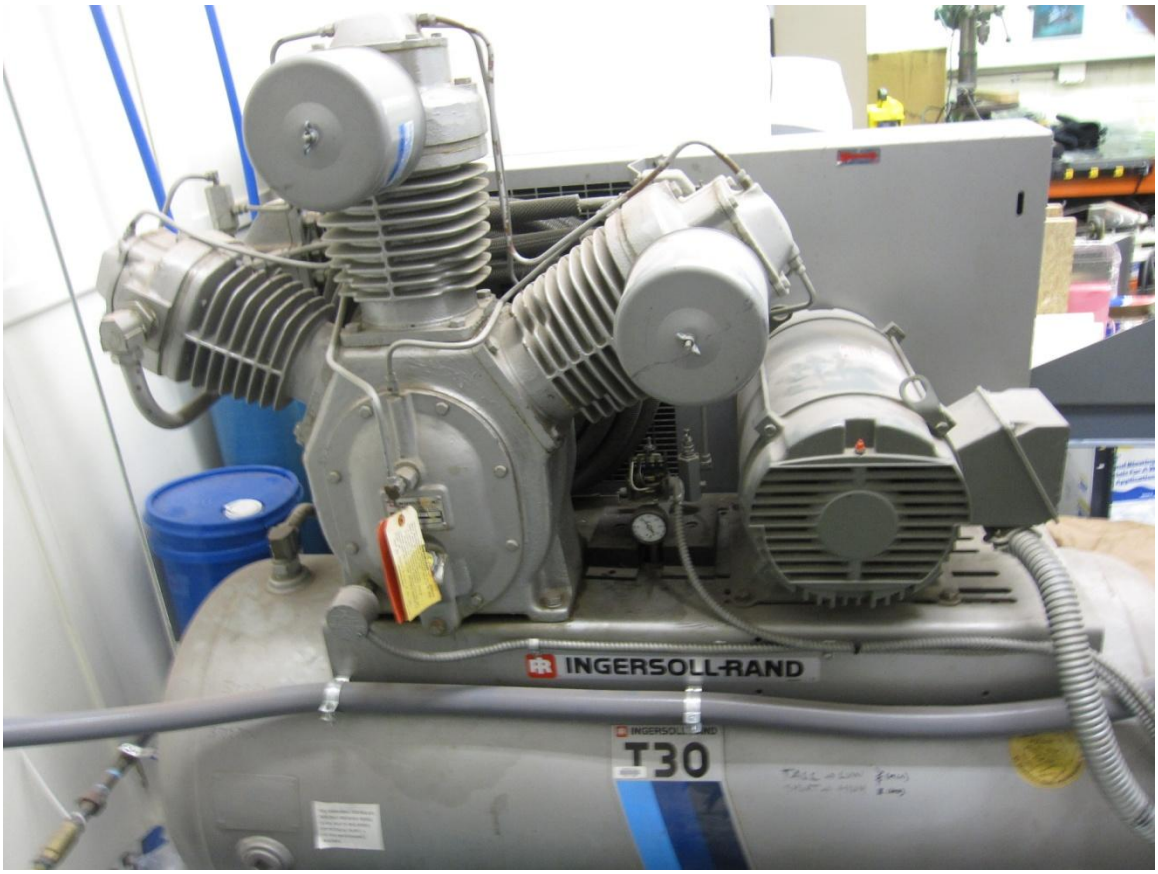

Figure 4-12: Large air compressor in AERTS facility.

A manual pressure regulator with a dial gauge was then used to dynamically adjust the pressure during the tests (Figure 4-13). However, the inclusion of the regulator reduced the maximum pressure 90 psi.

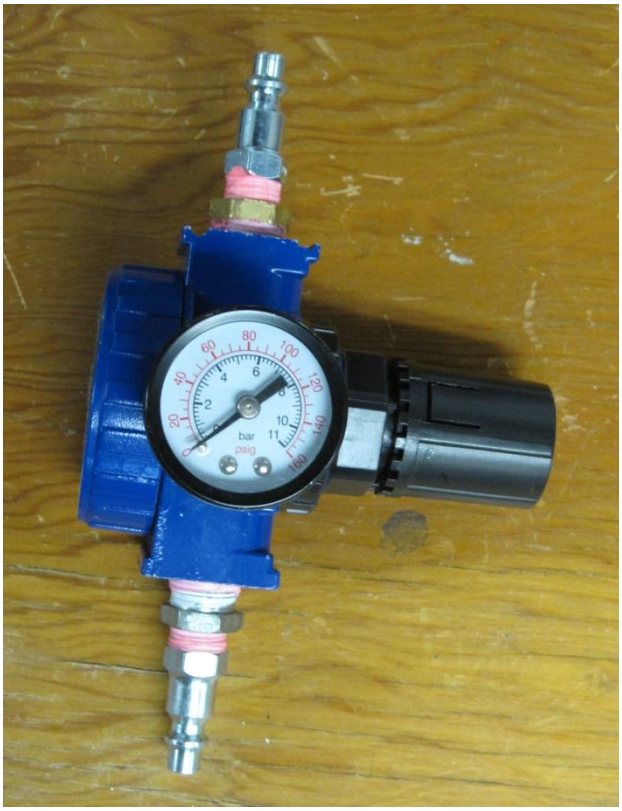

Figure 4-13: Manual pressure regulator.

Therefore, the third method of pressure control involved removing the regulator which increased the pressure to 105 psi, which was the maximum allowable in this facility. The direct connection was used to instantaneously actuate at higher speeds and the regulator was used to get a measurement of extension as a function of pressure for lower rotational speeds. Alternatively, the regulator could be used at the highest rotational speeds while sacrificing full extension capability.

4.6 Results and Comparison

While this is well below the maximum pressure, Figure 4-14 shows how the rotational speed affects the flat plate extension for a given pressure.

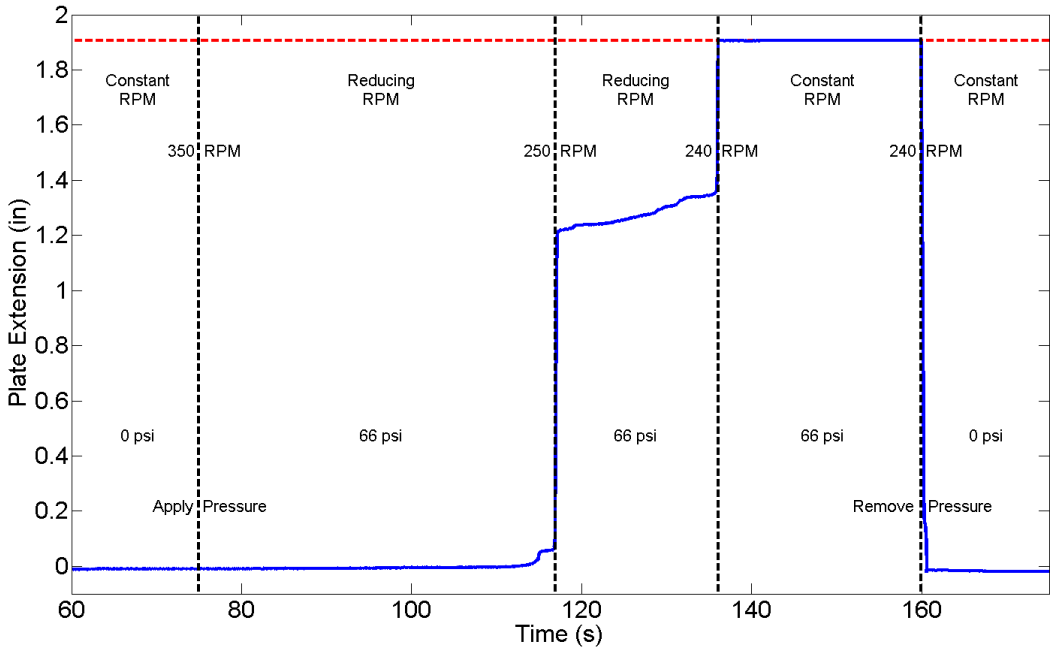

Figure 4-14: Plate extension under a varying rotational speed with the small compressor.

As expected, with a high starting rotational speed, the low pressure was not able to actuate the system. However, when the rotor speed was reduced from 350 to approximately 250 RPM, the system began to deploy. As the RPM was reduced further, the amount of plate extension gradually increased until instantaneous, full deployment at around 240 RPM. The pressure was held constant until approximately 160 seconds when it was removed entirely, causing an instantaneous retraction of the plate. As shown the maximum extension for the device was 1.906 in, which closely matches the 1.85 in estimate in the analytical solution.

The large compressor was then used in order to maximize the rotational speed, and centrifugal acceleration, at which the extendable chord system would deploy. Figure 4-15 shows the plate extension as a function of time at higher rotational speeds.

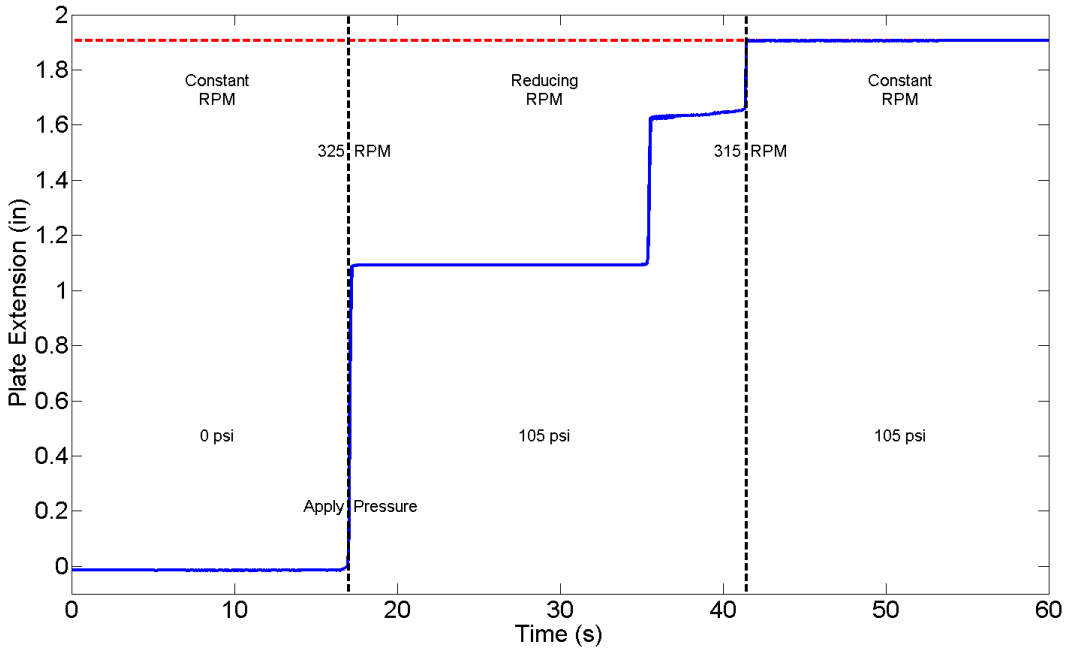

Figure 4-15: Plate extension under a varying rotational speed with the large compressor.

Given the results of the numerical solution in which the maximum rotational speed was anticipated to be 330 RPM, the next test was conducted with an initial rotor speed of 325 RPM. At approximately 17 s, the full 105 psi pressure is supplied to the system. The plate deploys approximately 1.09 in before abruptly stopping. As will be demonstrated, this was a common stopping point for the extendable chord system. This was most likely due to an increase in friction at this point, perhaps in one of the linear slides. The plate then fully deployed upon decreasing the rotational speed to 315 RPM. The brief pause at 1.64 in was also a common sticking point. A decent correlation between these results and the analytical results can be seen in Figure 4-16.

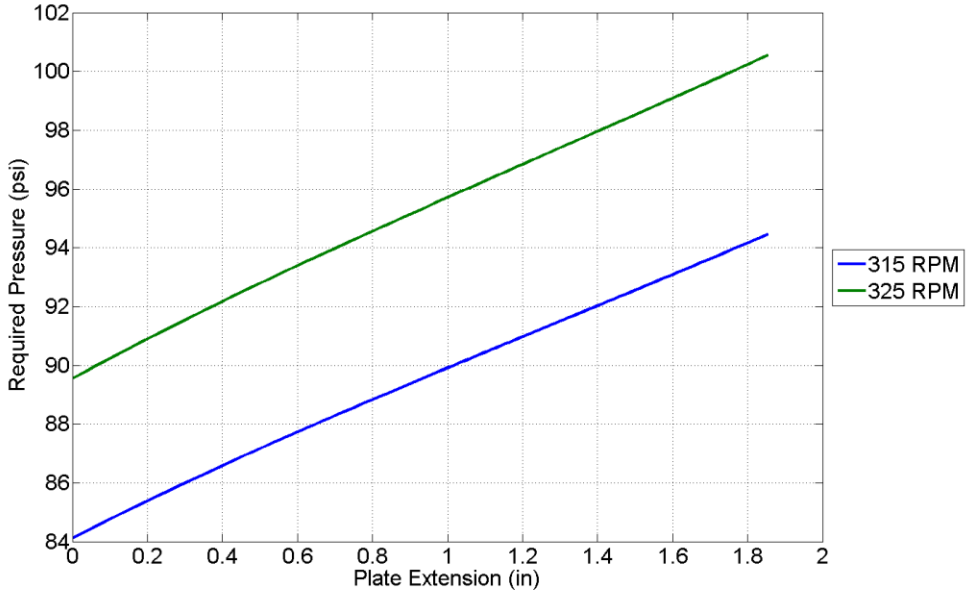

Figure 4-16: Pressure required to deploy the plate for a given position.

According to the analysis, the system should have fully deployed at 325 RPM given a pressure of 101 psi but it was not until 315 RPM that the supplied 105 psi was enough to extend the plate. For 315 RPM, comparing the anticipated 94 psi required to reach full extension with the 105 psi shown in the test yields a difference of 11 psi, or 10.5% error.

Using 315 RPM as the maximum rotational speed at which the system would deploy, a series of tests were conducted to gain a better understanding of how the system acts in this centrifugal field. Figure 4-17 shows the instantaneous deployment of the extendable chord system given an applied pressure of 105 psi.

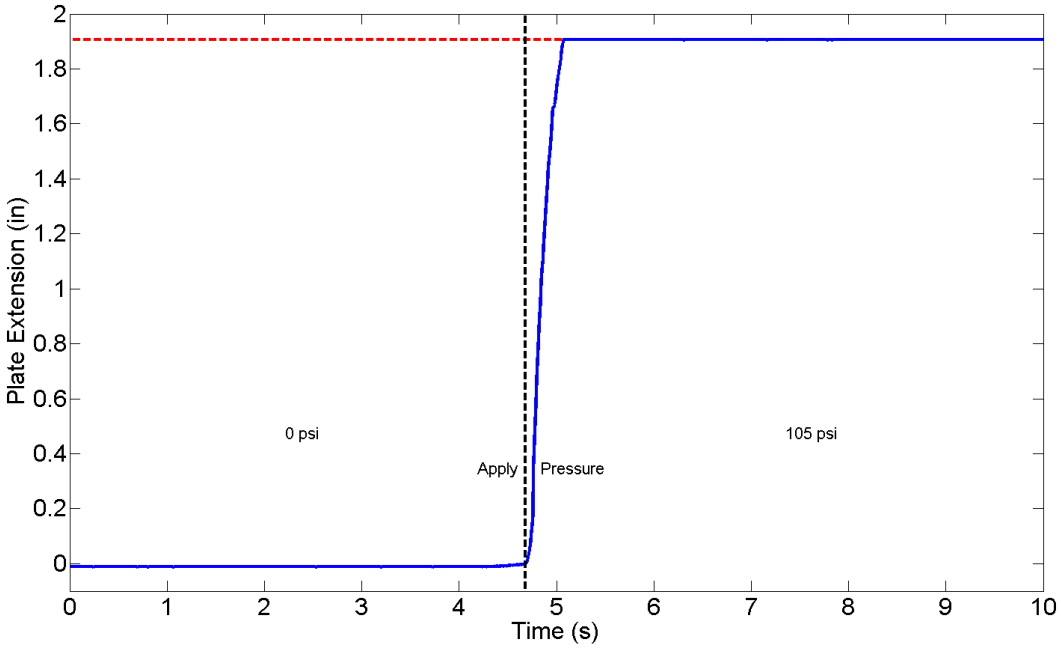

Figure 4-17: Pneumatically actuated extendable chord system deployment at 315 RPM.

The pressure regulator was then installed in order to gain more precise control for this test condition. Considering the decrease in maximum pressure, Figure 4-18 gives the variation of chord extension as pressure is increased for a constant rotational speed of 315 RPM.

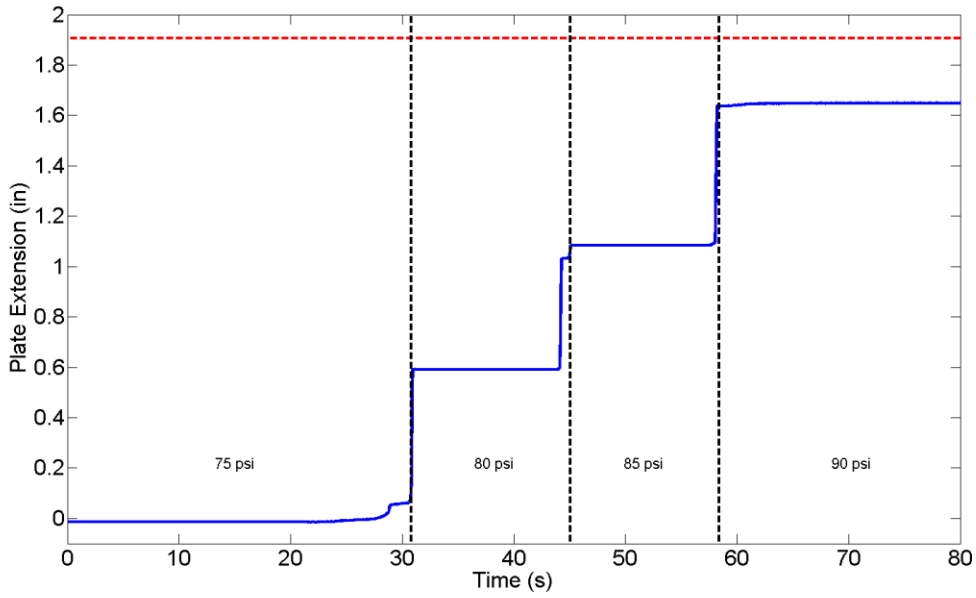

Figure 4-18: Plate extension using a pressure regulator.

Initially the applied pressure is 75 psi which was not sufficient to induce any movement. Manually increasing the pressure to 80 psi resulted in the first step to 0.59 in. The second step occurred at 1.08 in at 85 psi and terminated at 1.65 in at the maximum 90 psi. Note that the second and final deployment values are very similar to those found previously which supports the hypothesis that these points have a higher amount of local friction.

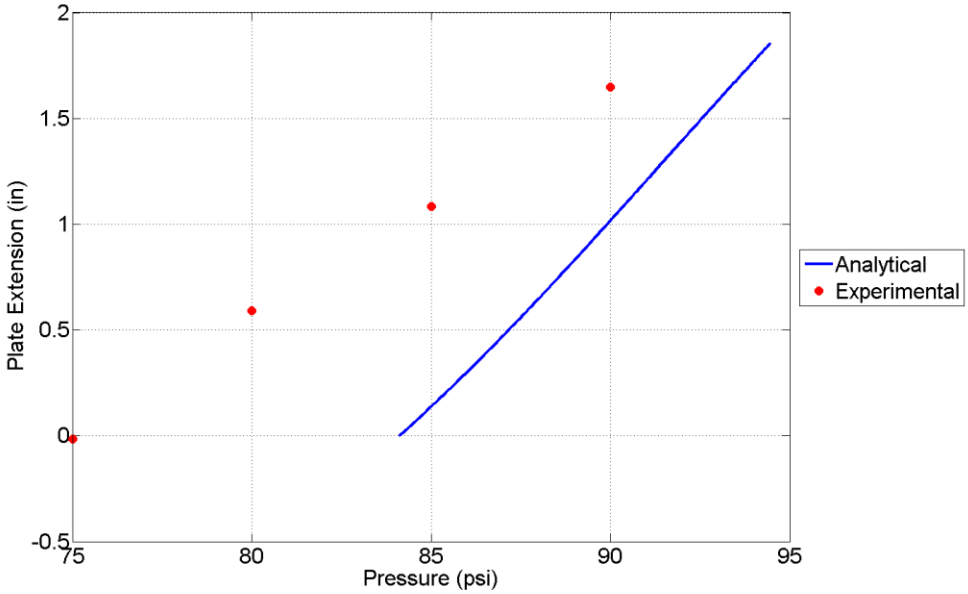

Figure 4-19: Comparison between experimental and analytical results of flat plate extension as a function of pressure for 315 RPM.

Comparing the plate displacement as a function of pressure during extension shows a fairly good agreement between the analytical and experimental results (Figure 4-19). As shown the analysis predicts zero extension for an input pressure below 84.1 psi. While the test shows no extension for 75 psi, at 80 psi the plate is extended 0.59 in which should not be achieved until an input pressure of 87.7 psi according to the analysis. Overall, the analysis underpredicted the amount of plate extension for a supplied pressure. The numerical solution was capable of predicting the pressure required to reach a given plate extension within 10%

On the other hand, the load cell output predicted by the analysis was again significantly different from the experiment (Figure 4-19).

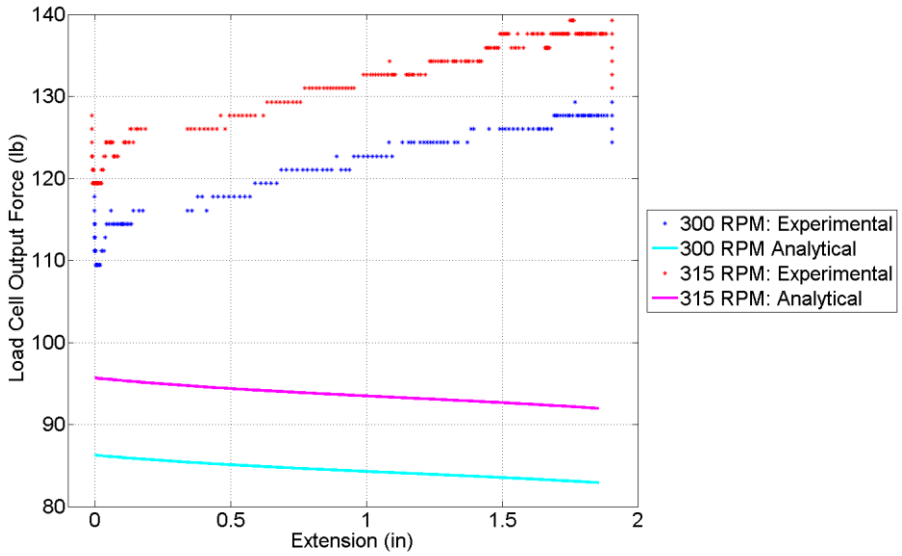

Figure 4-20: Load cell output comparison between experimental and analytical results with transverse shear correction.

While the analysis was capable of predicting the relative increase in force from 300 RPM to 315 RPM, the output from the tests was 20 to 45 lbs less than the analytical solution. It should be noted that these results already contain the increased output from the LC202-300 due to transverse shear. Clearly, it was not suitable to use a load cell on the linkage to gain an understanding of the forces within the system.

Chapter 5

Conclusions

This chapter presents a summary of the work conducted in this thesis. Additionally, the conclusions derived from the extendable chord prototype designs and experiments will be defined along with several recommendations for future work on this topic.

5.1 Summary

Improving helicopter performance is of great interest to the rotorcraft industry. Previous works have shown that various blade morphing technologies provide opportunities to significantly reduce main rotor power and consequently improve overall performance. Specifically, it has been shown that the rotor profile power can be reduced using a quasi-statically actuated, extendable chord system at the outer boundaries of the flight envelope where retreating blade stall is present. Thus, this thesis presented a concept for extending the chord over a section of the rotor blade in order to alleviate retreating blade stall and improve helicopter performance. The concept presented was built upon several previous studies which suggested that deploying a flat plate from the trailing edge of the airfoil has the ability to effectively extend the blade chord. As with any rotor blade morphing technology, the device must be able to withstand large centrifugal accelerations. Therefore, this work aimed to actuate the extendable chord prototype under the centrifugal accelerations representative of a full-scale helicopter. Furthermore, two

different actuation methods were considered: electromechanical and pneumatic actuators. The centrifugal testing was conducted in the Pennsylvania State University's Adverse Environment Rotor Test Stand.

5.2 Electromechanically Actuated Prototype

Considering the design space defined by the AERTS facility blade test section, an extendable chord system was developed using a commercially available electromechanical actuator. The device was constrained to be fully contained aft of the spar. In this manner, the impact on existing blade structural properties was minimized. The concept introduced in this work utilized a spanwise actuation displacement along the spar which was transformed into chordwise plate extension via a single linkage, truss structure. Although not present in the prototype, the system incorporated the design elements required to accommodate blade twist. This included rotational elements on the linkage and plate assembly in the form of rod ends and hinges, as well as an extension element at the plate assembly.

However, initial tests on the rotor stand indicated a design flaw which arose as a result of the moment created at the sliding element along the spar. The moment caused the system to bind even at very low centrifugal accelerations. A solution was presented in which the linkage was pinned directly to the electromechanical actuator, thus eliminating the moment arm. Unfortunately, this solution also removed the three-axis rotational element required at the end of the linkage for twist accommodation. A more suitable solution would be to incorporate an attachment on the actuator which would then be pinned to the rod end. However, this was not possible for the current design due to spanwise space constraints.

The final design of the extendable chord prototype with electromechanical actuation had a system weight of 7.6 lbs. This could certainly be reduced in successive redesigns. Overall the system achieved a flat plate extension of 1.3 in, or 8.1% for the 16 in chord. While this was below the goals of the study, the maximum extension was severely limited by the geometry of the test section. The minimum retraction was limited by the space required for the actuator and the length of the linkage was determined by the spanwise dimension. Thus, moving the actuator and increasing the span has the potential to increase the extension significantly.

Spin testing in the AERTS facility demonstrated the successful operation of the system up to a rotational speed of 385 RPM. Given the radius of the midspan of the prototype, this corresponds to a centrifugal acceleration of 209.5 g's or approximately 47.2% of the full scale acceleration. At this rotational speed, the electromechanically actuated prototype demonstrated the ability to be extended and retracted in 19.3 s and 37.3 s, respectively. Ultimately, even though the experiment did not reach full scale centrifugal acceleration equivalent to a UH-60 helicopter at 73% radius, the actuation of an extendable chord structure in a high-g environment was proven.

Furthermore, the maximum rotational speed was limited by the electromechanical actuator capabilities and not a binding of the extendable chord truss structure. As was shown in one of the preliminary tests, the electromechanical actuator malfunctioned at 150 RPM, or 31.8 g's. After modifications to the gear head the current rotational speed was achieved. Even still, there was a noticeable decrease in efficiency of the actuator in the rotating environment. The current through the electromechanical actuator during plate retraction at 385 RPM was seen to be 1.65 A which is much higher than the maximum rated current of 0.79 A. Under these conditions, the system required 40 W to actuate. It was shown that careful consideration must be given to the selection (or design) of such an actuator in any morphing rotor blade technology.

As with any first generation design, several areas of improvement were identified that could potentially increase the operational limits of the extendable chord system. First, an electromechanical actuator designed specifically for high-g operation has the possibility of greatly improving the performance of this device. Secondly, careful redesign of the plate assembly could reduce the weight of the structure which would be beneficial not only from an actuation standpoint but in terms of blade stability as well. Finally, switching the direction of the actuator and balancing the chordwise and spanwise forces could significantly reduce the actuation force. This idea was partially demonstrated in the pneumatically actuated system; the results of which are presented in the following section.

5.3 Pneumatically Actuated Prototype

One of the goals of this thesis was to investigate the use of several different actuation methods for the extendable chord device. Previous studies have demonstrated the promise of pneumatics in morphing rotor blade technology. Therefore, a pneumatic cylinder was used in the extendable chord system and tested in a manner similar to the electromechanical actuator. The pneumatic system was subjected to the same design criteria and experimental process. Likewise, this system was meant to maintain as much of the electromechanical design as possible. Thus, the structural shell and plate assembly were identical to the previous design. However, several modifications were made to the system to improve its performance based upon the results of the electromechanically actuated system. Chiefly, the direction of the actuator has switched such that the displacement points radially outwards. A design in which the centrifugal force on the actuator tip mass retracts the system and the force on the plate assembly extends the system results in an

overall reduction in the force required to actuate the system. Furthermore, the sliding pin along the spar was replaced by a linear slide in an attempt to reduce friction.

The weight of the pneumatic cylinder is significantly less than the electromechanical actuator due to the simplicity of the device. The cylinder has a weight of 1.0 lb as compared to the 2.1 lb electromechanical actuator. However, due to the inclusion of the linear slide, the weight of the entire structure coincidentally remains at 7.6 lbs. Again, this could be reduced with a successful redesign. The pneumatic prototype was able to achieve an 11.9% chord extension, or 1.91 in. Similar to the EMA design, this could be significantly increased by increasing overall spanwise dimension of the system. Therefore, this amount is within the acceptable limits for this study.

During centrifugal testing in the AERTS facility, this prototype demonstrated successful operation up to 315 RPM. This rotational speed corresponds to a centrifugal acceleration of 140.2 g's, or 31.6% of the full-scale UH-60 loads. Furthermore, the centrifugal testing of the pneumatic prototype also exhibited the ability of this system to deploy nearly instantaneously under these conditions. However, the limiting factor on the rotational speed was the amount of pressure that the facility could supply. Unlike electrical slip rings which can operate at rotational speeds much faster than conventional helicopters, the range of safe operation of a pneumatic rotary union can be significantly limited. For instance, it was recommended by the manufacturer, that the rotational speed during this test should not exceed 300 RPM at the maximum 250 psi using lubricated air. Considering the nominal rotation speed of a UH-60 is 258 RPM, this clearly demonstrates the increased risk in using a pneumatic rotary union as opposed to an electrical slip ring for morphing rotor blade technology. For the current study, the maximum pressure available in the AERTS facility was limited to 105 psi. Results for this experiment showed a good correlation with the numerical estimation of the required pressure. Consequently, using the

numerical analysis, it was possible to validate the hypothesis that the force required to actuate the system could be significantly be reduced by balancing the spanwise and chordwise forces.

Ultimately, the spin testing demonstrated the operability of the pneumatically actuated, extendable chord system within a high-g centrifugal field. Moreover, it was shown that with a proper redesign, the system has the potential of reaching the full-scale centrifugal acceleration goals set forth at the genesis of this project.

5.4 Comparing Electromechanical and Pneumatic Actuation

Although the electromechanical and pneumatic prototypes were similar in terms of their construction and even their performance, several key differences were noticed that should be considered in subsequent designs:

1. The speed of deployment for the pneumatically actuated system was much greater than that of the electromechanical system. It appears that given a pressure sufficient to overcome the static friction in the system, the device will deploy nearly instantaneously. Likewise, when the pressure is removed, the plate snaps back into the retracted position. In contrast, the electromechanical system can take up to 20 s to deploy and 45 s to retract. Considering also the fact that the retraction time increases significantly as the centrifugal acceleration increases, at full-scale loading the EMA may not be have the ability to actuate the extendable chord system within the acceptable limits. Obviously this should be improved with a more suitable actuator; however, the extent of which remains to be seen.
2. While the rate of actuation is much larger for the pneumatic prototype, the electromechanical actuator provides a greater control of the position of the system. The

EMA can directly control the displacement of the actuator rather than relying on the balancing of forces to maintain a position, as is the case for the pneumatic cylinder.

3. The pneumatic cylinder is a much simpler internal design and is therefore less likely to fail in a rotating environment. As was seen in the experiments, the centrifugal field can have a significant impact on the internal gearing of the electromechanical actuator which not only affects the efficiency of the device, but also has the ability to result in a mechanical failure of the actuator. This could be rectified by using an EMA designed specifically for use in this environment; however, the cost of such an actuator would be much greater than that of a pneumatic cylinder with similar force capabilities.
4. The simplicity of the pneumatic cylinder also results in a significant weight reduction when compared to the electromechanical actuator. Minimizing the weight of the system could be of great importance when considering blade stability.
5. A pneumatic actuator requires a large air compressor. This could add significant weight as well as taking up valuable real estate within the helicopter. Alternatively, the compressor could be eliminated if the system were to use bleed air from the engines as a pressure source.
6. Perhaps the most important difference between the two actuation systems involves their behavior in the event of system failure. Uneven deployment across each of the blades could result in high vibration levels which could prove to be dangerous. Alternatively, when the helicopter is operating within the expanded envelope flight regime, an unexpected retraction of the system could result in substantial complications. Fortunately, the electromechanically actuated extendable chord system is self-locking due to the non-backdrivable nature of the geared DC motor. Therefore, if the power supply to one or all of the sections were to fail, the system would remain in the current position. Uniformity across the rotor disk would be maintained, eliminating the possibility of

uneven deployment. Even if the device would fail in the fully extended state, the helicopter would still be safe as it approached landing, albeit with a slight main rotor power increase. On the other hand, the pneumatic actuator does not have the ability to independently maintain position. At the outer boundaries of the envelope, a system failure could result in a retraction of one (or all) extendable chord systems which could result in severe consequences. While a locking mechanism could be used to fix the system at a predefined position (e.g. extended or retracted), this would not protect the system during actuation. Therefore, given a failure of the pressure supply line, it would be possible to obtain uneven deployment across the rotor. Overall, the electromechanical actuator performs better in the event of a failure.

5.5 Recommendations for Future Work

The present work has demonstrated the operability of an extendable chord system in a centrifugal field using electromechanical and pneumatic actuators. In addition, several areas of research have been identified as possible directions for future work on this concept. The recommendations below apply to both the electromechanical and pneumatic systems unless otherwise specified.

1. Although the structure presented in this thesis was designed to work in a twisted blade, modifications had to be made which removed one of these required elements. Therefore, future iterations of the extendable chord system should be constructed on a twisted blade section.
2. The extension of the prototypes manufactured in this study was severely limited due to the spanwise dimension of the test section. An increase in the plate extension (more than

20% chord) must be validated using an extendable chord section with a larger span. A larger span would also allow the load cell to be placed at the end of the actuator which could then be used to more accurately measure the actuation requirements and validate the numerical analysis.

3. Overall, the next design iteration of this system should be implemented on a full-scale blade section which includes the aforementioned twist and span. Furthermore, the system should be placed within a full-scale helicopter airfoil. This should account for the proper chord and thickness as well as camber.
4. Previous numerical analyses have shown an increased aerodynamic benefit of this device when the plate is deployed at an angle relative to the trailing edge camber line. Thus, a method of extending the plate with and angle of incidence should be developed.
5. The design should be optimized in to achieve the largest chordwise extension with the lowest actuation force. As previously mentioned, this would involve balancing the spanwise force on the moving actuator components with the chordwise plate forces in order to expand the range of rotational speeds over which the device can operate. Ultimately, actuation in a full scale centrifugal environment must be achieved in future work.
6. An extendable chord system using an electromechanical motor designed specifically to operate in a rotating environment should also be tested.
7. Future work should also involve the testing of a pneumatically actuated system with a more robust pneumatic rotary union which allows for greater pressures at higher rotational speeds.
8. The numerical force and moment analysis and finite element modeling showed the large forces and stresses that must be supported by the external blade structure. A detailed investigation into blade integration must be conducted to ensure the safety of the blade

under these loads. This includes reinforcement of the ribs and spar where the mechanism is installed. Furthermore, the unsupported skin over the span of the mechanism will likely need to be stiffened to prevent the aerodynamic suction forces from deforming the skin and reducing the effectiveness of the device.

9. Higher fidelity modeling of the system should also be investigated that are capable of capturing elastic deformations within the mechanism. This will provide a greater understanding of how the system performs in the rotating environment and should lead to a more accurate numerical analysis.
10. Past works have demonstrated performance increases with an extendable chord system using comprehensive rotor codes. However, effectiveness of the flat plate extended chord should be validated using scaled aerodynamic rotor testing.

References

1. Leishman, J.G. *Principles of Helicopter Aerodynamics*. 2nd ed. New York: Cambridge University Press, 2006.
2. Léon, O. *Reducing Helicopter Main Rotor Power Requirements Using Multiple Trailing Edge Flaps and Extendable Chord Sections*. MS thesis. The Pennsylvania State University, University Park, 2009.
3. Johnson, W. *Helicopter Theory*. New York: Dover Publications, Inc., 1980.
4. Bousman, W.G., "Aerodynamic Characteristics of SC1095 and SC1094 R8 Airfoils," NASA/TP-2003-212265, 2003, pp. 26-37.
5. Yeo, H. "Assessment of Active Controls for Rotor Performance Enhancement." *Journal of the American Helicopter Society*. 53.2 (2008): 152-163.
6. Liu, T., J. Montefort, W. Liou, and R. Pantula. "Lift Enhancement by Static Extended Trailing Edge." *Journal of Aircraft*. 44.6 (2007): 1939-1947.
7. Léon, O., E. Hayden, and F. Gandhi. "Rotorcraft Operating Envelope Expansion Using Extendable Chord Sections." *American Helicopter Society 65th Annual Forum and Technology Display*. 27-29 May 2009.
8. Khoshlahjeh, M., F. Gandhi, and S. Webster. "Extendable Chord Rotors for Helicopter Envelope Expansion and Performance Improvement." *American Helicopter Society 67th Annual Forum and Technology Display*. 3-5 May 2011.
9. Noboru, K., N. Kondo, S. Saito, T. Akasaka, and Y. Tanabe. "An Experimental Study of On-blade Active Tab." *30th European Rotorcraft Forum*. 14-16 September 2004.

10. Saito, S., K. Noboru, and Y. Tanabe. “Application of an active device for helicopter noise reduction in JAXA.” *Fluid Dynamics Research*. 42. (2010).
11. Matalanis, C., A. Kuczek, R. Lin, E. Manes, B. Wake, and J. Yeh. “Development of an Active Trim Tab System for Onboard Rotor Tracking.” *American Helicopter Society 66th Annual Forum and Technology Display*. 12-13 May 2010.
12. Matalanis, C., A. Kuczek, B. Wake, N. Soldner, U. Jonsson, and V. Lakamraju. “Blade Integration of a Modular Active Trim Tab System for Onboard Rotor Tracking.” *American Helicopter Society 67th Annual Forum and Technology Display*. 3-5 May 2011.
13. Johnson, T. *Bistable Devices for Morphing Rotor Blades*. PhD dissertation. The Pennsylvania State University, University Park. 2010.
14. Barbarino, S., F. Gandhi, and S. Webster. “Design of Extendable Chord Sections for Morphing Helicopter Rotor Blades.” *ASME 2010 Conference on Smart Materials, Adaptive Structures, and Intelligent Systems*. 28 September - 1 October 2010.
15. Rufino, R., T. Miller, and F. Gandhi. “Morphing Hull Concepts for Unmanned Underwater Vehicles.” *Oceans, Poles and Climate: Technological Challenges*. 15-18 September 2008.
16. “General Purpose Small Geared DC Motors.” *Mclennan Servo Supplies*. Web. 12 Jun 2012. <http://www.mclennan.co.uk/product/generalpurposesmallgearedmotorassy.html>.
17. Palacios, J., Y. Han, E. Brouwers, and E. Smith. “Icing Environment Rotor Test Stand Liquid Water Content Measurement Procedures and Ice Shape Correlation.” *Journal of the American Helicopter Society*. 57.2 (2012): 29-40.
18. “The Bug - Precision Linear Actuator from Ultra Motion.” *Ultra Motion Linear Actuators*. Web. 15 Jun 2012. <http://www.ultramotion.com/products/bug.php>.

19. "NSK Linear Bearings." *NSK Americas*. Web. 2 Jul 2012. <http://www.nskamericas.com/cps/rde/xchg/na_en/hs.xsl/linear-guides.html>.
20. "LC202." *Omega Engineering*. Web. 15 Jun 2012. <http://www.omega.com/Pressure/pdf/LC202.pdf>.
21. "SoftPot Potentiometer." *Spectra Symbol*. Web. 15 Jun 2012. <http://www.spectrasymbol.com/potentiometer/softpot>.
22. "V-Link® –mXRS™ Wireless Voltage Node." *MicroStrain*. Web. 12 Dec 2011. <http://www.microstrain.com/wireless/v-link>.
23. *ANSYS®, Release 13.0, Help System, Element Reference, Part 1 Element Library, Ansys Inc.*
24. Oberg, E., F. Jones, H. Horton, and H. Ryffel. *Machinery's Handbook (27th Edition) & Guide to Machinery's Handbook*. Industrial Press, 2004. 1473-1848. Web. <http://www.knovel.com/web/portal/browse/display?_EXT_KNOVEL_DISPLAY_bookid=1074&VerticalID=0>.
25. Woods, B., C. Kothera, and N. Wereley. "Whirl Testing of a Pneumatic Artificial Muscle Actuation System for a Full-Scale Active Rotor." *American Helicopter Society 66th Annual Forum and Technology Display.* 11-13 May 2010.
26. "Series 012 2 Pass Threaded Shaft Unions." *Rotary Systems.* Web. 17 Jul 2012. <http://www.rotarysystems.com/series-012>.
27. "Cylinders." *Clippard Instrument Laboratory.* Web. 2 Jul 2012. <http://www.clippard.com/cylinders/>.

Appendix A

Calibrations

The following sections detail the process of calibrating each of the components used in the spin test. Each of the sensors was calibrated independently using the V-Link wireless transmitter to acquire the data.

A.1 Spectra Symbol SoftPot Membrane Potentiometer

A.1.1 Modified Electromechanical Actuator Prototype

Table A-1: SoftPot calibration data points for electromechanically actuated prototype.

Data Point	Transmitter Value (bits)	Extension (in)
1 – Retracted	3698	0.000
2	3270	0.460
3 – Midpoint	3047	0.732
4	2829	0.975
5 – Extended	2381	1.294

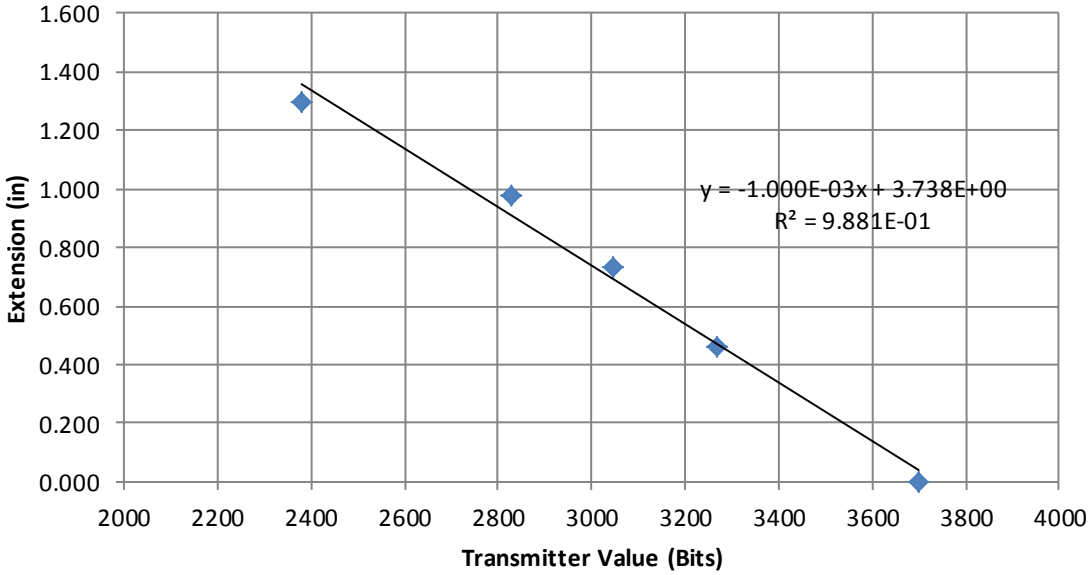

Figure A-1: SoftPot calibration curve for electromechanically actuated prototype.

A.1.2 Pneumatic Actuator Prototype

Table A-2: SoftPot calibration data points for pneumatically actuated prototype.

Data Point	Transmitter Value (Bits)	Extension (in)
1 – Retracted	3928	0.000
2*	3622	0.236
3	2875	0.517
4	2386	0.744
5	1885	0.981
6	1379	1.229
7	846	1.491
8	306	1.763
9 – Extended	43	1.890

* Outlier not included in calibration curve

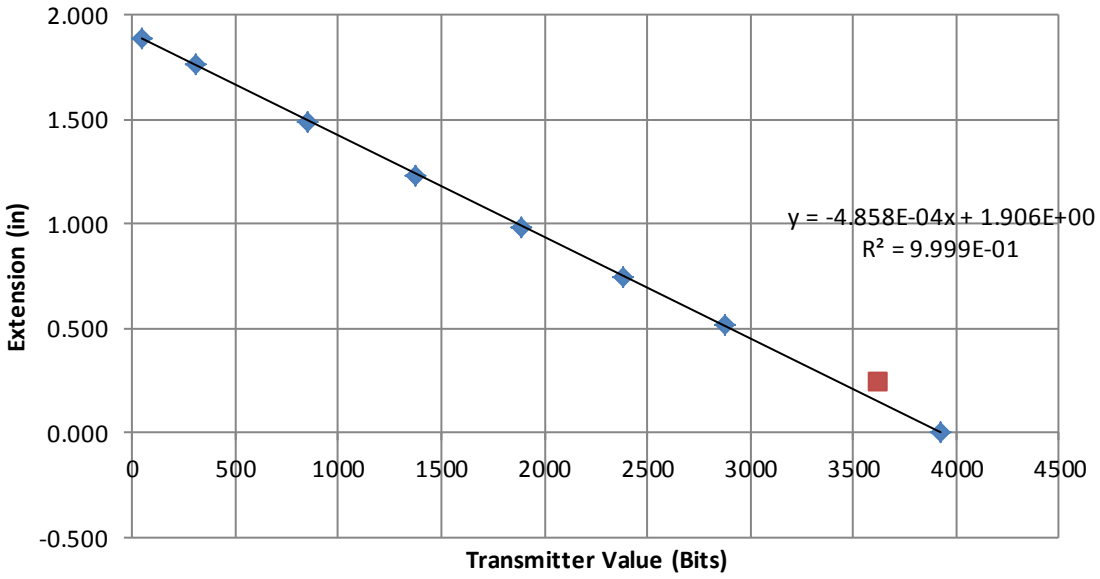

Figure A-2: SoftPot calibration curve for electromechanically actuated prototype.

A.2 Ultra Motion Bug Actuator Potentiometer

Table A-3: Electromechanical actuator potentiometer calibration data points.

Data Point	Transmitter Value (Bits)	Extension (in)
1 – Deployed	1244	1.449
2 – Middle	2882	0.509
3 – Retracted	3784	0.000

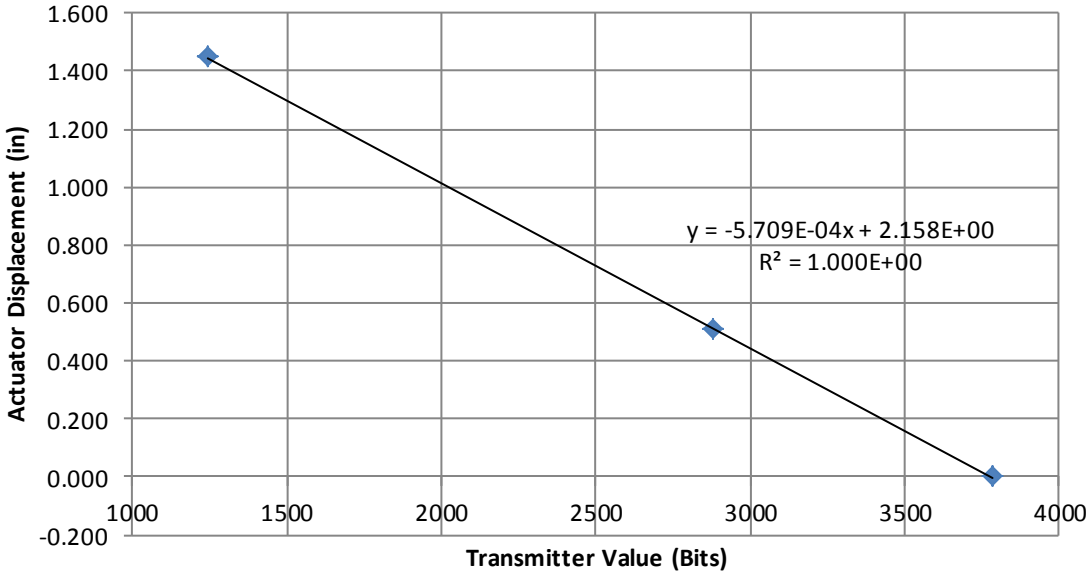

Figure A-3: Electromechanical actuator potentiometer calibration data points.

A.3 Omega Engineering LC202-300 Load Cell

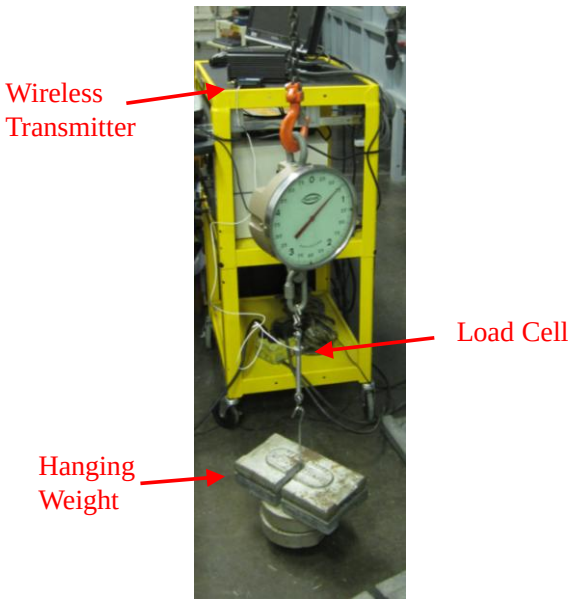

Figure A-4: Axial calibration of the LC202-300 load cell.

Table A-4: Load cell axial calibration data points.

Tensile Force (x 100 lbs)	Transmitter Value (Bits)
0.00	3064
0.10	3057
0.20	3051
0.30	3045
0.40	3039
0.50	3033
0.60	3027
0.70	3020
0.80	3014
0.90	3008
1.00	3002
1.10	2996
1.20	2990
1.30	2984
1.40	2978
1.50	2972
1.60	2966
1.70	2960
1.80	2954
1.90	2948
2.00	2942

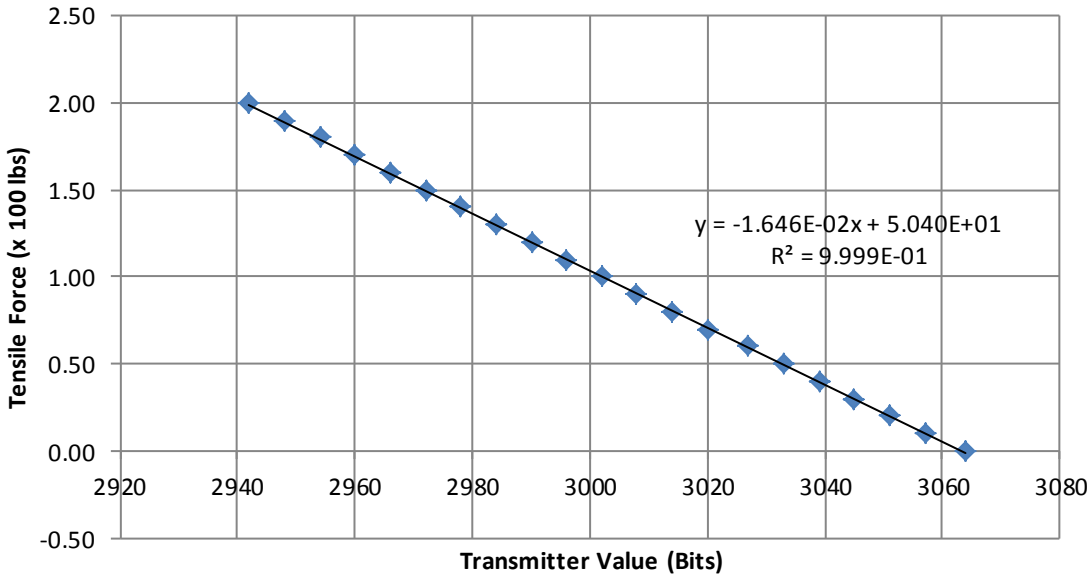

Figure A-5: Load cell axial calibration curve.

A.4 Ultra Motion Bug Performance

Considering the modifications made to the gearing, the efficiency of the electromechanical motor may have been altered. Figure A-7 shows the calibration of the current required by the modified electromechanical actuator as a function of the tensile output force. It is assumed that the actuator performance depends only upon the direction of the force relative to the direction of motion and not whether the actuator is in tension or compression. That is, the same curve can be used for retracting the actuator in tension as extending the actuator in compression.

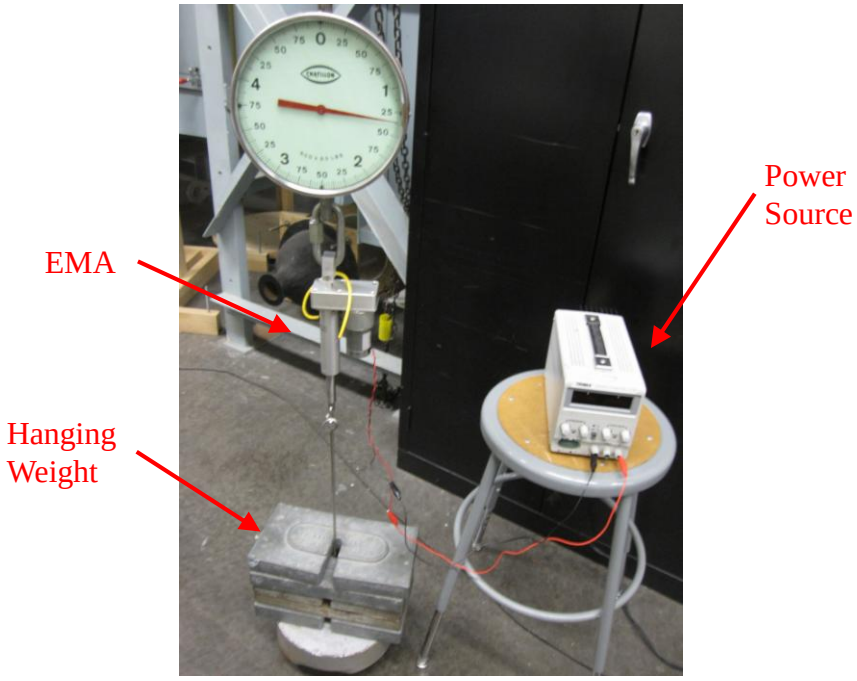

Figure A-6: Modified EMA performance calibration setup.

Table A-5: Modified EMA performance calibration data points.

Tensile Force (lbs)	Current (A)	
	Retraction	Extension
1	0.13	0.11
21	0.16	0.115
41	0.19	0.105
51	0.205	0.099
61	0.215	0.098
71	0.23	0.095
81	0.243	0.091
91	0.257	0.086
101	0.267	0.083
111	0.282	0.079
131	0.307	0.075
151	0.333	0.068

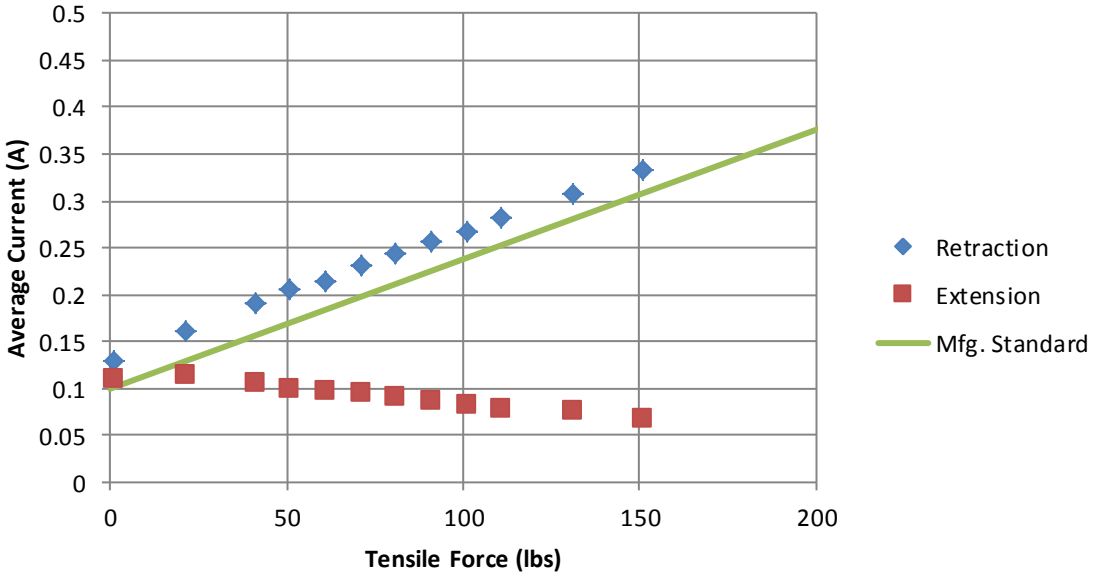

Figure A-7: Modified EMA performance calibration curve.

Appendix B

Pneumatic Force and Moment Analysis

This section presents the rigid body force and moment analysis used in the pneumatically actuated, extendable chord system. Eqn. 17 combined with the diagram in Figure 4-3 can be used to determine the kinematics of the system.

$$x_A - x_C\ ^2 + \ y_C - y_A\ ^2 = {L_{AC}}^2 \tag{17}$$

The loads can be determined in a similar manner to the EMA design. It should be noted that the inclusion of the coincident actuation transmitter, and subsequent removal of point B, has reduced the system to 6 degrees of freedom. The force and moment equations have been collected into the linear system shown in Eqn. 18.

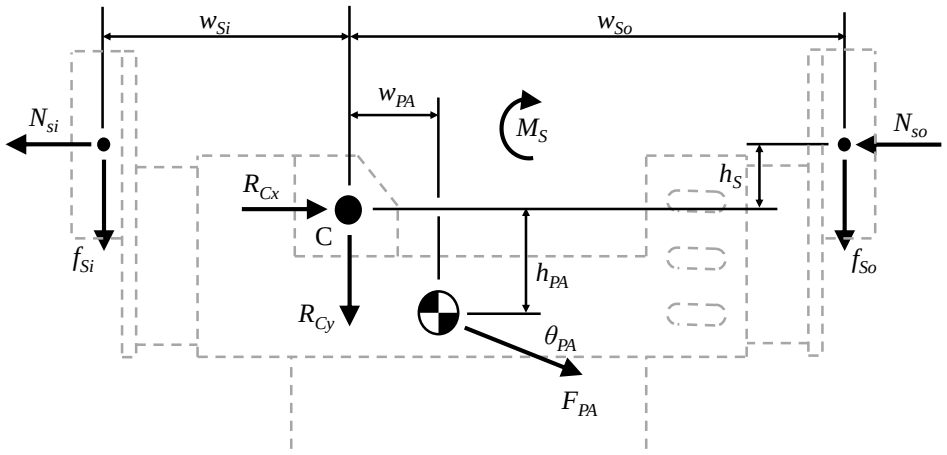

Figure B-1: Force and moment diagram of plate assembly in pneumatic system.

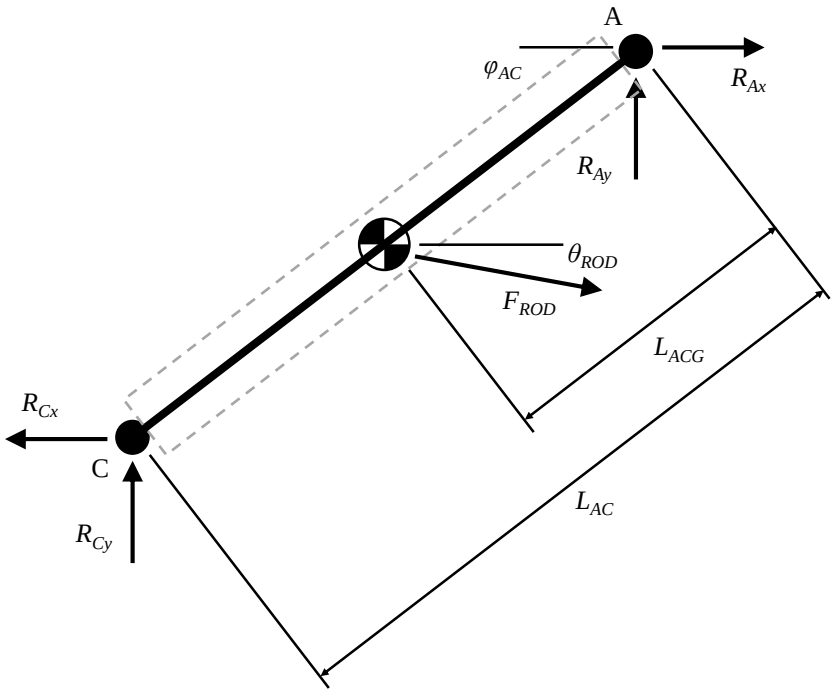

Figure B-2: Force and moment diagram of linkage in pneumatic system.

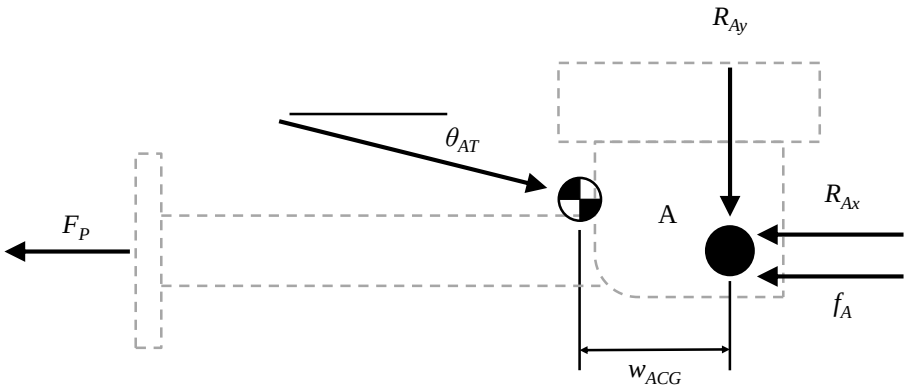

Figure B-3: Force and moment diagram of actuator components in pneumatic system.

$$A\ x = b \tag{18}$$

where

$$A = \begin{matrix} 0 & 0 & 1 & 0 & -1 & 0 \\ 0 & 0 & 0 & 1 & \mu_S & 0 \\ 0 & 0 & 0 & 0 & -h_S + \mu_S\ \frac{w_{So}}{2} - \frac{w_{Si}}{2} & 1 \\ 1 & 0 & -1 & 0 & 0 & 0 \\ 0 & -1 & 0 & -1 & 0 & 0 \\ 0 & 0 & y_C - y_A & x_A - x_C & 0 & 0 \end{matrix},$$

$$x = \begin{matrix} R_{Ax} \\ R_{Ay} \\ R_{Cx} \\ R_{Cy} \\ N_S \\ M_S \end{matrix}, and\ b = \Omega^2 \begin{matrix} -M_{PA}R_{PA}\cos\theta_{PA} \\ -M_{PA}R_{PA}\sin\theta_{PA} \\ M_{PA}R_{PA}\ -w_{PA}\sin\theta_{PA} + h_{PA}\cos\theta_{PA} \\ -M_{ROD}R_{ROD}\cos\theta_{ROD} \\ -M_{ROD}R_{ROD}\sin\theta_{ROD} \\ M_{ROD}R_{ROD}L_{ACG}\ \sin\theta_{ROD}\cos\theta_{AC} + \cos\theta_{ROD}\sin\theta_{AC} \end{matrix}$$

Appendix C

Rotor Test Stand Circuit

The spin test set up, shown in Figure C-1, was used to control the electromechanically actuated system. The 24 V power source was used to control the direction of the actuator simply by reversing the polarity of the signal. It should be noted that while the V-Link wireless transmitter has an onboard battery, an external 9 V source was used to power the device. Each of the sensors was powered directly from the wireless transmitter. This setup was identical for the pneumatic system with a few exceptions. Obviously the electric power source was removed and replaced by the pneumatic compressor which was then connected to the rotary union. Also, this actuator did not include a built in potentiometer.

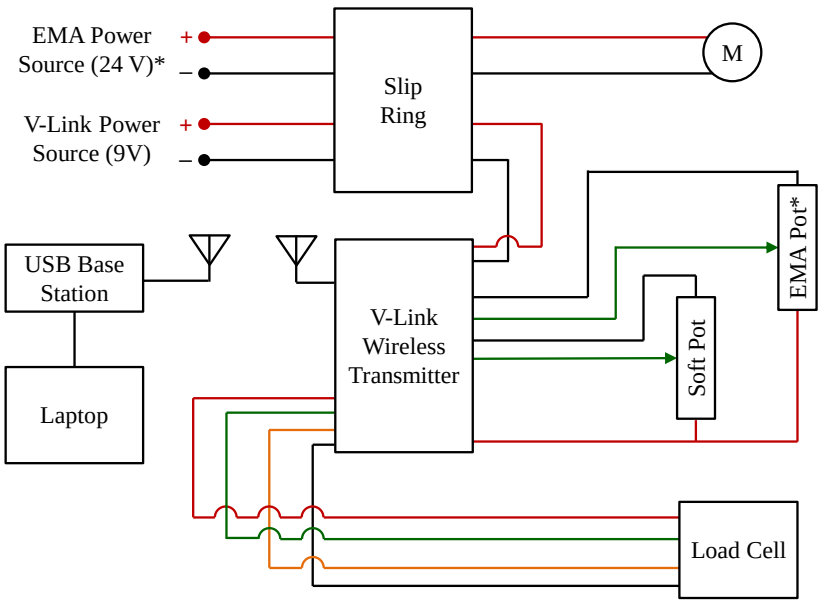

Figure C-1: Rotor test stand set up.